A comparison of trace element concentrations in chromite from komatiites, picrites and layered intrusions: Implications for the formation of massive chromite layers.

Sarah-Jane Barnes*[1], Eduardo T Mansur[1, 2] Wolfgang D Maier [3], Stephen A Prevec [4]

[1]Sciences de la Terre, Université du Québec à Chicoutimi, 555 boulevard de l'université, Québec G7H 2B1, Canada

[2]Geological Survey of Norway, P.O. Box 6315 Torgarden, NO-7491 Trondheim, Norway

[3] School of Earth and Environmental Sciences, Cardiff University, Cardiff, United Kingdom

[4] Department of Geology, Rhodes University, Makhanda, South Africa, 6140.

*Corresponding Author

Email for correspondence sjbarnes@uqac.ca

Keywords, Chromite, Trace elements, komatiite, picrite, Great Dyke, Stillwater, Bushveld,

Abstract :

By examining the minor and trace element contents of chromites from three intrusions; the Bushveld Complex (South Africa), the Stillwater Complex (USA) and the Great Dyke (Zimbabwe), and comparing these chromite compositions to those of magmas from which they could have formed (komatiites and picrites) we conclude that: a) the variations in Ti, V, Sc and Ga contents across stratigraphy and across individual layers do not support the model of magma mixing leading to chromite-only crystallization; b) the chromites from the lowest levels of the intrusions could have crystallized from komatiite liquids that were contaminated with continental crust; c) the Great Dyke chromites have the highest Cr# and lowest incompatible element contents and formed from a liquid closest to komatiite; d) all of the chromites, except those of the Dunite Succession of the Great Dyke have equilibrated with a liquid that had also crystallized pyroxene; e) the Great Dyke and Stillwater chromites show a narrower range in composition than the Bushveld chromites; f) Chromites from the western limb of the Bushveld Complex contain much higher V contents than all the other chromites. This requires either, that the fO_2 was lower in the western Bushveld or that the chromites equilibrated with a V-rich magma. We favor a model where chromite and silicate minerals crystallized in cotectic proportions (~2:98). The chromite, silicates and transporting liquid are emplaced into the magma chamber. During emplacement the chromite and silicate separated due to viscous particle flow to form a massive chromite layer overlain by silicates.

Introduction

The composition of chromite is of interest for both petrogenetic and economic reasons. On the petrogenetic side, chromite is one of first minerals to crystallize from primary magmas and one of the last to be consumed during partial melting of the mantle. Thus, variations in chromite compositions could potentially help inform us of the conditions during partial melting of the mantle and during crystallization of primary magmas. On the economic side, two important issues are worthy of consideration. First, the only economic source of Cr is chromite, either from massive chromite layers in ultramafic to mafic intrusions or as podiform chromites in ophiolites (Cawthorn et al. 2005; Mosier et al. 2012; Schulte et al. 2012). Most (> 70%) Cr is produced from mafic and ultramafic intrusions, principally the Bushveld Complex of South Africa, with minor production from the Great Dyke of Zimbabwe, the Kemi intrusion of Finland, and the Nuasahi and Sukinda intrusions of India (Fig. 1a). In terms of resources, however, the deposits are more evenly divided with the ophiolites (mainly Kempirsai, Kazakhstan) containing >40 % of the world's reserves (Fig. 1b). Another point of economic interest is that most of the chromite layers and podiform chromites are enriched in the platinum-group elements (PGE) Os, Ir, Ru, relative to the surrounding silicate rocks and some are also enriched in Rh, Pt and Pd (Barnes et al. 2016; Brough, et al. 2015; Mondal et al. 2019; Naldrett et al 2009; Scoon and Teigler 1994). Indeed, the world's largest PGE deposit is hosted in a massive chromite layer called the UG2 (Upper Group chromite layer 2) of the Bushveld Complex (McLaren and de Villiers 1982; Naldrett 2011). However, the PGE in massive chromites from layered intrusions are not found in the chromite (Pagé et al. 2012; Pagé et al. 2016)

The origin of the massive chromite layers in intrusions and podiform chromite in the ophiolites is not clear. A fundamental question is how a rock consisting of >50% chromite can be formed from a mafic magma, because during crystallization the cotectic proportion of chromite to silicate minerals is approximately 1 to 2 % (Roeder et al. 2006). This leads to two problems: a) how can 1 to 2% chromite be concentrated to form a massive chromite layer? And 2) assuming equilibrium processes, at least 1000 times more magma than chromite is required. Furthermore, following chromite crystallization this magma should be Cr depleted and yet at the Bushveld Complex mass balance calculations show that insufficient Cr-depleted material is present (Cawthorn and Walraven 1998; Eales 2000). Campbell and Murck (1993) point out the same problem at the Stillwater Complex, however there and at the Great Dyke, parts of the upper portions of the complexes have been eroded and therefore it is not possible to say that there is insufficient Cr-depleted material present in these cases.

A number of models have been proposed. We can consider these in terms of their ability to saturate the magma in chromite by changing the intensive variables of temperature, pressure, oxygen fugacity (fO_2), and composition of the magma or in terms of physical processes.

1) Initially it was thought that as temperature dropped, olivine crystallized, resulting in the composition of the magma becoming more oxidized and iron-rich. The magma then would crystallize both olivine or pyroxene and chromite in cotectic proportions. The chromite then settled through the liquid and accumulated on the cumulate pile (Wagner 1923). This model is currently out of favor, because the chromite grains are generally quite small (0.05 to 0.2 mm) and therefore it is thought would not settle in spite of the large density contrast between silicate magma and oxide. However, Manoochehri and Schmidt (2014) demonstrated using centrifuge experiments that chromite does settle. Furthermore, recently a variation of the chromite settling model has been suggested in which chromite grains might form clusters by syneusis. Such clusters would then be large enough to settle (Vukmanovic, pers. com.).

2) Liu and Presnall (1990) showed that in the Mg-Ca-Al system spinel is less soluble at high pressure. This has led to models whereby a large increase in the amount of chromite crystallizing is brought about by a sudden increase in pressure in the magma chamber (Cawthorn 2005; Lipin 1993). However, Roeder and Reynolds (1991) found that chromite is, in fact, slightly more soluble at high pressure. Latypov et al. (2017, 2022) proposed that a rapid transfer of a superheated magma from depth would lower pressure in the magma and could bring chromite only onto the liquidus which they modelled using the MELTS program.
3) An increase in fO_2 would ensure that most of the Cr is converted to Cr^{3+} (the form of Cr in chromite) leading to chromite saturation (Ulmer 1969; Murck and Campbell 1986; Roeder and Reynolds 1991).
4) The dominant model for the past 40 years has been a sudden compositional change brought about by magma mixing – a model (based on Fe-free experiments; Irvine, 1977) whereby primitive magma mixed with fractionated resident magma temporarily leads to chromite-only crystallization. However, recent experimental work which included Fe shows that magma mixing will not bring about chromite-only saturation (Keltie 2018).
5) Based on silicate inclusions in chromite some authors have suggested that addition of SiO_2 from a partial melt of SiO_2 rich country rocks (in particular in the roof of intrusions) could lead to chromite-only saturation (Irvine 1975; Alapieti et al. 1989; Kinnaird et al. 2002; Spandler et al. 2005). However, this process requires so much SiO_2 to be added to the magma that olivine would not be on the liquidus, which is inconsistent with the presence of olivine in the chromite layers from the Stillwater Complex and the Great Dyke (Irvine, 1977) and in some of the Bushveld chromite layers (Gain 1985).

6) Veksler and Hou (2020) found that by adding 2 to 4% H_2O to a magma of a composition similar to the proposed composition of the Bushveld B1 magma (Barnes et al. 2010) would lead to a 250 ^{o}C interval of chromite-only crystallization. However, the addition of H_2O suppresses plagioclase crystallization, which is inconsistent with the presence of large amounts of plagioclase in the chromite layers of the Upper Critical Zone of the Bushveld. Furthermore, the chromite compositions found in the experiments are too rich in Fe compared with those of observed Bushveld chromite.
7) Lesher et al. (2019) proposed that partial melting of banded iron formation and release of magnetite to a komatiite magma could result in the magnetite being converted to chromite that then formed the chromite layers. Experimental work by Keltie (2018) found that magnetite dissolves in komatiite magma, thus raising the Fe content of the magma which leads to chromite saturation at lower Cr contents. If sufficient Fe is added, then chromite-only crystallization does occur.

Some models, particularly those looking at the formation of chromite in ophiolites, propose a compositional change brought about by reaction between preexisting silicate minerals and a new melt.

1) For podiform chromites it is proposed that orthopyroxene in harzburgites reacted with Si-under saturated melt derived from deeper in the mantle to form olivine plus chromite (Arai 1997; González-Jiménez 2014).
2) Variations on this model have been proposed for chromite in layered intrusions, whereby picritic melts percolated down into the cumulate pile and reacted with the cumulate minerals to form thin chromite layers (O'Driscoll et al. 2009). Alternatively, fluids rising through the

cumulate pile could react with norite to dissolve orthopyroxene, releasing Cr and leaving an anorthositic residuum (Marsh et al. 2021). The Cr-rich liquid precipitated chromite at a level in the intrusions where conditions changed such that the Cr-rich liquid became saturated in only chromite (Nicholson and Mathez 1991; Marsh et al. 2021).

Some models suggest the chromite is collected by physical processes.

1) Density currents could transport chromite from the upper parts of the chamber to the top of the cumulate pile (Irvine 1979, 1980), but this still leaves the mass balance problem unresolved.
2) To circumvent the mass balance problem, so called “offstage” models have been proposed, whereby chromite and silicate minerals crystallized in cotectic proportions to form a slurry of chromite, silicates and liquid. This slurry was then injected into the magma chamber (Eales 2000; Jenkins and Mungall 2018; Mondal and Mathez 2007; Voordouw et al. 2013) or slumped from the walls into the magma chamber (Forien et al. 2015; Maier et al. 2013; Naldrett et al. 2012; Wilson and Prendergast 1989) and during transport the chromite and silicates were separated from each other by winnowing. The Cr-depleted liquid is thought to have slumped into the center of the intrusion (Forien et al. 2015; Maier et al. 2013) or have been forced up along the sides of the intrusion (Naldrett et al. 2012).

Previous studies of the major and minor element composition of chromite (Barnes and Roeder 2001; Kamenetsky; et al. 2001) were constrained by two factors. First, the concentrations of only a few elements (Ti, Al, Cr, Fe and Mg) could be reliably determined due to the limitations of microprobe analysis. Secondly, chromite is generally an accessory mineral present at <2 modal %, and is consequently susceptible to post-crystallization re-equilibration with the other phases present. This is particularly true for the 2+ ions (Barnes 1998; Roeder and Campbell 1985), such that the original composition of the chromite can be difficult to estimate.

The advent of laser-ablation inductively-coupled plasma mass spectrometry (LA-ICP-MS) provides the opportunity to quantify a wider range of elements down to the ppm and even ppb level for many minerals, including chromite. Consequently, there are now numerous studies of the compositions of chromite found in rocks representative of the mantle, conducted with the goal of understanding processes in the mantle (Gonzalez-Jimenez et al. 2014; Pagé and Barnes 2009; Zhou et al. 2014). Other uses include the application of V content of chromite from komatiites, to document the oxygen fugacity of the early Earth (Canil 2002; Nicklas et al. 2016). The PGE contents of chromites from volcanic rocks have been determined to investigate the use of PGE concentrations in chromite in exploration for Ni and PGE deposits (Arguin et al. 2016; Locemellis et al. 2011; Pagé et al. 2012; Pagé and Barnes 2016; Park et al. 2012, 2017). However, the trace element content of chromite from layered intrusions has not received much attention.

There are three large layered intrusions that contain PGE deposits; the Rustenburg Layered Suite of the Bushveld Complex (South Africa), the Stillwater Complex (Montana, USA) and the Great Dyke (Zimbabwe). All contain numerous massive chromite layers. This work will present results for the chromite compositions from these intrusions and compare the results with compositions of chromite from the Alexo komatiite (Ontario, Canada) and picrites from the Emeishan large igneous province (China), with the aims of determining: a) the type of magma from which the chromite crystallized and b) the process(es) whereby they formed.

Materials and Methods.

Terminology.

In many publications the term chromitite is used to refer to rocks with a high percentage of chromite. However, the use of the term is inconsistent, varying from rocks with >90% chromite to rocks with 30% chromite. In order to avoid confusion the term will not be used here. The terms massive chromite will be applied to rocks containing >66% chromite (the volume at which chromite grains in a rock should be in contact), semi-massive chromite for rocks containing 33% to 66% chromite (some chromite grains will be contact and but some silicate grains will be in contact), disseminated chromite for rocks containing 2 to 33%.

Materials

Stillwater Complex

The Stillwater Complex, Montana, U.S.A. (Fig. 2a) is a layered intrusion that was emplaced into the Archean Wyoming Craton over a three million year period, 2709 to 2012 Ma. (Wall et al. 2018). The host rocks consist of a meta-sedimentary sequence, which was intruded by a granitoid suite between 2730 and 2790 Ma (Wooden 1991). The complex has been divided into 5 series; the Basal, the Ultramafic, the Lower Banded, Middle Banded and Upper Banded (McCallum et al. 1980).

The lower part of the Ultramafic series, known as the Peridotite zone, consists of a series of cyclic units of harzburgites overlain by olivine orthopyroxenites and orthopyroxenites (Cooper 1997; Jackson 1961). Within the peridotites, zones consisting of layers of semi-massive to massive chromite are present. The chromite zones are labelled A to K from the base upwards (Fig. 2b). In most cases, each chromite zone contains a number of chromite-rich layers separated by chromite-bearing peridotite or pyroxenite (Fig. 3a). In many cases, but not all, the silicate rocks associated with the chromite layers have a pegmatoidal texture. The zones vary in thickness from thin doublets of the E zone (5 to 10 cm, Fig. 3a) to the thick (4 m) G zone (Page 1971). The thickness of individual layers of chromite varies from 1 cm to 50 cm, with the basal layers of the G and H chromite zones (Fig. 3b) being the thickest (~30 to 50 cm, Page 1971) and the layers of the C, E, I and J chromite zones being amongst the thinnest (1-3cm). The upper part of the Ultramafic series consists of orthopyroxenite, which contains ~0.5 modal % chromite (Barnes et al. 2016), and is called the Bronzitite zone. McCallum (2002) reports that the zone is uniform except for a few thin layers of olivine +/- chromite. All of the zones, A to K were sampled along two traverses across the Mountain View and Benbow areas (Fig. 2a). In addition a rare example of massive chromite from the olivine-bearing zone 1 (OB1), just below the level of the PGE deposit (the JM reef) was provided by Dr. Zientek.

Most of the layers are massive in these two areas. Exceptions to this are layers C and E which are semi-massive (30 to 50 modal % chromite). In the semi-massive layers, where most of the chromite grains do not quite touch, the grains are euhedral and small (0.2-0.5 mm). In contrast, in the massive layers many of the chromite grains are larger (1-2 mm), anhedral, and have 120^{o} triple junctions, suggesting that they grew post-cumulus (Fig. 3c). The interstitial minerals in most of the chromite layers are subhedral olivine and oikocrysts of orthopyroxene (Fig. 3d). Exceptions to this are the E and J chromite layers where the interstitial mineral is predominantly subhedral orthopyroxene (Fig. 3e). The igneous assemblage has been preserved in most of our samples, but some samples contain serpentine, chlorite, actinolite and epidote as a result of greenschist facies metamorphism at 1700 Ma (Page 1977).

The Bushveld Complex

The Rustenburg Layered Suite (RLS) of the Bushveld Complex (South Africa) (Fig 4) was emplaced into the Archean Kaapvaal Craton over a 5 million year period, 2055-2060 Ma, (Scoates et al. 2021). It is the world's largest known layered intrusion (400 km by 300 km in area, and approximately 8 to 9 km thick; Eales and Cawthorn, 1996). The RLS is divided into five zones (Hall, 1932): the basal Marginal Zone (0-800 m of norites), overlain by the Lower Zone (800-1300 m of cyclic units of harzburgites and pyroxenites), the Critical Zone (1000 to 1800 m of cyclic units of chromite, pyroxenites, and norites), the Main Zone (3000 to 3400 m of norites, gabbronorites and anorthosites), and the Upper Zone (2000 to 2800 m of magnetitites, ferrogabbronorites anorthosites, and diorites) (Fig. 4).

Twelve to 14 chromite layers are found in the Critical Zone. (As in the case of the Stillwater Complex these layers are more correctly referred to as zones because in many cases each "layer" consists of more than one massive chromite layer, but to be consistent with published literature the term layers will be used, with the understanding that more than one massive chromite layer can be present. In most areas the Lower Critical Zone consists of a series of cyclic units of chromite layers and pyroxenites with minor harzburgites (Cameron 1980; Engelbrecht 1985; Scoon and Teigler 1994, Naldrett et al. 2012, Kaufmann 2018). The massive chromite layers in the Lower Critical Zone are referred to as Lower Group (LG) 1 to 7, overlain by the Middle Group (MG) 0 to 2. The base of the Upper Critical Zone is marked by the appearance of plagioclase as a cumulus phase in an anorthosite layer just above the MG2 chromite. In most areas, the Upper Critical Zone contains four to five layers of chromite, namely Middle Group (MG3 to 4) and Upper Group (UG) 1 to 3. These layers occur within units consisting of chromite, pyroxenite and norite. Some cyclic units contain anorthosites at the top of unit. Some 30 to 300 meters above the UG2 Reef (depending on location) is the Merensky Reef (and cyclic unit). The base of the Merensky unit is typically marked by a narrow 1-5 cm chromite layer. Normal Reef generally has two chromite layers, although as many as four and as few as one (or none) occur in some sections. The common rock type between the layers is coarse-grained melanorite usually described as "pegmatoidal feldspathic pyroxenite".

In the northern limb (or lobe) the stratigraphy is more complicated (Grobler et al. 2019; Maier et al. 2021). The Lower Zone and Lower Critical Zone are largely absent. Rocks considered equivalent to the Upper Critical Zone, containing numerous xenoliths, are found at the lower contact. The first chromite layer in this zone is believed to be equivalent to the UG2.Tthe Lower Zone is expressed as intrusions within the country rocks and, in contrast, to the western and eastern limbs chromite layers occur in the Lower Zone (Hulbert and von Gruenewaldt 1985).

For the current study, samples from the Marginal Zone sills as well as the LG6, MG1 and MG3, UG1 and UG2 chromites were analyzed by LA-ICP-MS. The MG1 and MG3 samples are from the Waterval Mine in the western Bushveld (Arunachellan 2022). The UG1 and UG2 samples are from the Impala Mine, (western Bushveld) previously studied for variations in whole rock compositions (Maier and Barnes 2008). In addition, Langa et al. (2021) analyzed chromite from two cross sections of UG2, one from the northern limb and one from the western limb from the Waterval Mine. The samples from the western limb will be referred to as UG2-W and those from the north as UG2-N in the following text. Samples from the other layers were not available at the time of this study and so the data set is supplemented for the layers LG1 to 5, MG2 and MG4 by the microprobe data of Naldrett et al. (2012).

As in the case of the Stillwater chromite, crystals from the semi-massive chromites are fine grained (0.1 to 0.5 mm) and euhedral, whereas in the massive chromite the chromite grains are coarser (0.5 to 1 mm) and show triple junctions. The chromites from the massive chromites contain small (4 X 40 μm) ilmenite exsolutions. In the Lower Critical Zone the most common interstitial mineral is orthopyroxene. Small amounts of interstitial plagioclase and clinopyroxene are also present. The orthopyroxene can take the form of oikocrysts enclosing the chromite grains or occurs as euhedral laths. In our sample set of the Upper Group chromites the dominant mineral is interstitial plagioclase with minor orthopyroxene. Both minerals commonly take the form of oikocrysts (Figs. 5a and b).

The Great Dyke

The Great Dyke of Zimbabwe is a 550 km-long layered intrusion (Fig. 6) of early Proterozoic age (2575.4 ± 0.7 Ma, Oberthür 2002; Oberthür 2011) emplaced into the granite-greenstone terrain of the Zimbabwean Craton (Worst, 1960). The stratigraphy as defined by Wilson and Prendergast (1989) consists of a lower 2 km of the intrusion made up of ultramafic rocks (the Ultramafic Sequence), and an upper 1.5 km of mafic rocks (the Mafic Sequence) (Fig. 6). In the thickest part of the intrusion, the Ultramafic Sequence is divided into 14 cyclic units. The lower part of the Ultramafic Sequence (the Dunite Succession) comprises a series of cyclic units consisting of massive chromite layers overlain by dunite. The upper part of the Ultramafic Sequence (the Pyroxenite or Bronzitite Succession) consists of cyclic units of massive chromite layers overlain by harzburgites, which in turn is overlain by orthopyroxenite. Not all units contain a chromite layer. The chromite layers are labeled from the top of the Ultramafic Sequence downwards from C1 to C12, where the numeral refers to the number of the cyclic unit in which the chromite is present. Towards the top of the very last orthopyroxenites of the Ultramafic Sequence is a 1 to 2 m-thick zone of PGE enrichment, known as the Main Sulfide Zone. Chromite layers 12 to 5 are thin (<20 cm) and contain very little (<5%) interstitial material (Wilson 1982). Chromite layers 4 to 1 are thicker (1 to 2 m), but contain more (20%) interstitial material (Wilson 1982). Chromite grains in the chromite layers are 0.5 to 3 mm in size and polyhedral, with triple junctions. The interstitial material in the Dunite Succession is olivine or serpentine after olivine, whereas in the Bronzitite Succession the interstitial silicates are orthopyroxene and olivine. Only samples from layers C8, C6 and C1d were available for the current LA-ICP-MS study. These data are supplemented with major and minor element compositions from Wilson (1982) and Mason Apps (1998). Disseminated chromite is present in the MSZ, and major and minor element data are available from Chaumba and Musa (2020), but were not included in the current study.

Chromite from komatiites and picrites.

In order to assess the composition of chromite crystallized from magma types that could be important in forming the layered intrusions, the composition of chromite grains from the Alexo komatiites of the Abitibi Greenstone Belt, Canada (Barnes et al. 1983; Houlé, et al. 2012; Meric 2018) and picrites of the Emeishan large igneous province, China (Arguin et al. 2016; Barnes et al. 2022) are considered.

The samples from the Alexo komatiites are from a thin olivine spinifex-textured flow and from a thick clinopyroxene spinifex-textured flow (Barnes et al. 1983). These correspond to categories 1 and 4, of Barnes (1998), representing a thin differentiated flow and layered lava-lake, respectively. The distinction may be important because the chromite from a thin flow would have less time to re-equilibrate with trapped liquid. Fine (<0.2 mm) euhedral disseminated (<1% modal) chromite grains are present interstitially to the olivine and to the acicular pyroxene in devitrified glass. Also present in the spinifex-textured part of the flow are skeletal chromite. However, only the euhedral chromite was analyzed. The Alexo locality was chosen because the degree of metamorphism is low (prehnite-pumpellyite facies, Jolly 1982) and thus changes in composition due to metamorphism are, probably, limited (Barnes 1998).

Detailed descriptions and analyses of chromite from the Emeishan large igneous province have been presented previously (Arguin et al. 2016; Barnes et al. 2022). Most authors suggest that two distinct magma series are present, high-Ti and low-Ti (Xu et al. 2001). However, Kamenetsky et al. (2012) propose that rather than two distinct series, there is a continual gradation from low to high-Ti magmas, The picrite samples from the current study do form two distinct groups - one (high-Ti) enriched in Ti, Hf, Nb, Sn and LREE relative to one (low-Ti) depleted in these elements, but enriched in Al (Barnes et al. 2022). Therefore the terms high-Ti and low-Ti picrite will be used in this work. Picrites from both magma series contain disseminated chromite grains (0.1 to 0.2 mm in size). The grains occur in two habits, as inclusions in olivine (inclusion chromite) and as interstitial grains in a fine grained matrix of clinopyroxene, plagioclase and magnetite (matrix chromite). The inclusion chromites are euhedral and compositionally unzoned (Fig. 2 of Barnes et al. 2022). The matrix chromites have an overgrowth of titano-magnetite surrounding the chromite core (Fig. 3 of Barnes et al. 2022). Barnes et al. (2022) found that the chromite compositions reflect the composition of the magma series, with chromite from high-Ti picrites being enriched in Ti, V, Nb, Sn, Hf and Ta and depleted in Al relative to chromite from low-Ti picrites.

Methods

Polished thin sections of each sample were made and then examined with a petrographic microscope. Chromite grains were selected based on their appearance. Euhedral grains which lack fractures were favored. Five to 10 grains from each sample were analyzed. Major elements, Mg, Al, Fe, Cr and minor elements Si, Ti, Mn and Ni were determined on a CAMECA SX100 microprobe by wavelength dispersive spectrometry (beam size 5 μm, accelerating voltage 15 Kv, and current 20 nA) at the Université Laval, Québec City. The concentration of minor and trace elements were determined by LA-ICP-MS at LabMaTer Université du Quebec a Chicoutimi using an Excimer 193 nm resolution M-50 laser ablation system (Australian Scientific Instrument) equipped with a double volume cell S-155 (Laurin Technic) and coupled with an Agilent 7900 mass spectrometer. The LA-ICP-MS tuning parameters were a laser frequency of 15 Hz, a power of 3 mJ/pulse, a dwell time of 7.5 ms, and a fluence of 5 J/cm^2. The beam size was 55 or 44 μm depending on the size of the grain. For the komatiite-hosted chromite grains (because of their small size), spots in the center of the grains were used, but for the other chromites, line scans from time to rim across the surface of grains were made with a raster speed of 5 to 10 μm/s, depending on grain size. In order to avoid edge effects and possible alteration at the rims only the central part of the spectra was used for the line scans. The gas blank was measured for 30 s before switching on the laser for around 60 s. The ablated material was carried into the ICP-MS by an Ar–He gas mix at a rate of 0.8–1 L/min for Ar and 350 mL/min for He, and 2mL/min of nitrogen was also added to the mixture. Data reduction was carried out using the Iolite package for Igor Pro software (Paton et al. 2011). Maps of the element distribution were made of some chromite grains using the same parameters. The maps were generated using the Iolite package, based on the time-resolved composition of each element.

The isotopes ^{29}Si, ^{31}P, ^{34}S, ^{44}Ca, ^{75}As, ^{121}Sb, ^{125}Te, and ^{209}Bi were monitored in order to exclude inclusions of; silicate, apatite and platinum-group element minerals. Inclusions were rare and excluded from the analyses. The isotopes ^{24}Mg, ^{27}Al, ^{45} Sc, ^{49}Ti, ^{51}V, ^{52}Cr, ^{55}Mn, ^{57}Fe, ^{59}Co, ^{60}Ni, ^{63}Cu, ^{66}Zn, ^{71}Ga, ^{89}Y, ^{93}Nb, ^{95}Mo ^{101}Ru, ^{103}Rh, ^{108}Pd, ^{111}Cd, ^{115}In, ^{118}Sn, ^{178}Hf, ^{181}Ta, ^{185}Re,

^{189}Os, ^{193}Ir, ^{195}Pt, and ^{197}Au were used to determine the concentrations of these elements. possibility of interference of ^{53}Cr^{40}Ar on ^{93}Nb was investigated. However, there appears to be no correlation between Cr and Nb; for example Nb concentrations in the in-house reference chromite AX37 and MIA (which contain the highest observed Cr concentrations) are amongst the lowest Nb concentrations at 0.015 ppm, close to detection limit. Therefore, the Cr interference on Nb was considered negligible. The concentrations of Sn are too low for ^{115}Sn to produce a significant interference on ^{115}In and thus was not considered. Cadmium, Cu and Ni concentrations are too low to produce interferences on Pd, Rh and Ru and thus the potential interference from these elements was not considered.

External calibration was carried out using two reference materials. GSE-1g (supplied by USGS), with a composition close to a basaltic glass and doped with ~400 ppm of most trace elements, was used for minor and trace elements, except the PGE, Au and S. Laflamme Po727 (supplied by Memorial University), a pyrrhotite (FeS) doped with ~ 40 ppm of each PGE and Au, was used for the PGE and Au. ^{57}Fe was used for internal calibration. Natural chromite from in-house reference materials, AX 37 (a komatiite) and GProbe 6 (a basaltic glass), were used as monitors. The results obtained for the monitors agree within analytical error with the working values (Supplementary Material, Table S1). Representative chromite analyses are presented in Table 1. The full list of chromite analyses is provided in Supplementary Material, Table S2.

The results from the microprobe were used for Mg, Al, Si, Cr and Fe. The results from the LA-ICP-MS were used for all other elements. Comparison of Ti and Mn from the two methods are within 5 relative percent of each other.

Results

Platinum-Group Elements, Re and Au.

The concentrations of the Or, Ir, Ru and Rh for most of the analyzed chromites have been previously discussed in Arguin et al. (2016), Barnes et al. (2016), Meric (2018), Pagé et al. (2012) and Pagé and Barnes (2016). These authors found that Os, Ir, Ru and Rh, are present in chromite from volcanic rocks and in the marginal sills of the Bushveld at the 100 to 400 ppb level for Ru and at the 10 to 30 ppb level for Os, Ir and Rh. However, chromite from intrusions contain abundances below detection limits of Os, Ir, Ru and Rh (<10 to 20 ppb). Chromite from the intrusions contain small (1 to 20 μm) inclusions of laurites, which host the Os, Ir and Ru, and malanite, which hosts Rh (Barnes et al. 2016; Prichard et al. 2017). In the current study we also determined Pt, Pd, Au and Re concentrations and found that chromites from all settings contain less than detection levels of these elements (< 10 to 20 ppb). These observations are in agreement with other studies of PGE in chromite (Kamenetsky 2015; Locmelis et al. 2011, Park et al. 2012; 2017). The PGE, Au and Re will not be discussed any further in this work.

Major Elements

Chromium is the most abundant element in chromite and is rapidly depleted as the parent magma evolves, therefore for an overview the element concentrations are presented on plots of Cr_2O_3 versus the element or oxide. A more traditional approach would be to use Cr#, but this is affected by plagioclase crystallization and by oxidation state of the magma. Chromium concentrations vary from 35 to 60 weight % (Fig. 7). Chromites from komatiites and the Great Dyke show the highest Cr_2O_3 concentrations, from 52 to 59 weight %. In addition, the chromite from the LG1 to LG4 layers and from the sills of the Bushveld Complex fall in this range. Chromite from the Stillwater Complex, the Emeishan picrites and most of the remaining

Bushveld chromites show a lower range, from 40 to 50 weight % Cr_2O_3. An exception to this is chromite from the UG2-N of the Bushveld where Cr_2O_3 concentrations are lower, at 35 to 42 weight %.

Magnesium shows a positive correlation with Cr_2O_3 (Fig. 7a). Chromites from komatiites, the Great Dyke and the Bushveld Complex form a single broad trend from 15 weight % MgO for the Cr_2O_3-rich chromite to 4 weight % MgO for the UG2-N. The Stillwater Complex and Emeishan chromites appear to be more MgO-rich at a given Cr_2O_3 than the other chromites. All Fe is plotted as FeOT, although some Fe is present as Fe_2O_3. Because most of the Fe in chromite occupies the same site as Mg, FeOT shows an inverse behavior to MgO with the Great Dyke and komatiite samples having the lowest FeOT contents at 15 weight % and the UG2-N chromites having the highest FeOT content at up to 40 weight %. The Stillwater Complex chromites plot off the general trend, with lower FeOT at a given Cr_2O_3 content, consistent with their slightly higher MgO contents.

Aluminum oxide shows an inverse correlation with Cr_2O_3, which is to be expected as both elements occupy the same trivalent crystallographic site in chromite. Most chromites fall on a general trend from a low of 10 weight % Al_2O_3 in the komatiite and Great Dyke through to a high of 20 weight % Al_2O_3 in the Stillwater chromites. Exceptions to this trend are chromites from the UG2-N and the Emeishan high-Ti picrites which are depleted in Al_2O_3 relative to Cr_2O_3 (Fig. 7c).

Minor Elements

Titanium oxide shows an inverse correlation with Cr_2O_3, but more than one trend is evident (Fig. 8a). The chromites from the Great Dyke, komatiites, low-Ti picrites, the Bushveld sills, LG1 to LG4 and the Stillwater Complex define one trend (I), with fairly low TiO_2 contents at 0.2 to 0.5 weight % and relatively little change in TiO_2 with Cr_2O_3. The chromites from the Emeishan high-Ti picrites a second, steeper, trend (II) ranging from 1.5 to 2.5 weight % TiO_2. The chromites of the Bushveld Complex from LG5 to UG2-W and the chromites from the UG2-N show trends parallel to the Emeishan high-Ti picrite chromites, but contain lower Cr_2O_3 concentrations.

As is the case for TiO_2, V shows a negative correlation with Cr_2O_3, but more than one trend is evident (Fig. 8b). The chromites from the Great Dyke, komatiites, Bushveld sills, LG1 to LG4, Stillwater, the Emeishan high-Ti picrites and UG2-N form one trend, starting at 800 ppm and rising to 2000 ppm in the UG2-N. The chromites of the Bushveld above the LG4 are richer in V than the other chromites and form a second trend, starting at 1500 ppm and rising to 3600 ppm. The chromite from Emeishan low-TiO_2 picrites form a separate cluster with low V contents of <1000 ppm.

Manganese shows a negative correlation with Cr_2O_3, ranging from low values of ~1000 ppm in the komatiites to a high of 2500 ppm in the UG2-N (Fig. 8c). The Mn values from the Great Dyke cover a much wider range. Manganese concentrations of chromites from our study and that of Mason-Apps (1982) are low and similar to the komatiites. However, most of Wilson's (1982) MnO concentrations for chromite, shown inside the circle on figure 8c, are much higher.

Overall, Zn shows a negative correlation with Cr_2O_3, with a low of 300 ppm in the Great Dyke chromites through to a high of 1600 ppm in the UG2-N (Fig. 7d). A few samples plot at much higher values than indicated by the overall trend.

Cobalt concentrations range from 200 to 350 ppm for most of the chromites and fall on a single but very broad trend showing a negative correlation with Cr (Fig. 8e). Exceptions to this are the chromites from the Bushveld sills and the chromite from the C1 unit of the Great Dyke which all have higher Co concentrations, in the 350 to 500 ppm range

Nickel concentrations do not show a clear relationship with Cr_2O_3 (Fig. 8f). The concentration of Ni in chromite from massive chromites varies from 500 to 1500 ppm. The chromites from the Emeishan picrites are generally richer in Ni, at 1500 to 2000 ppm, whereas the Ni concentrations in chromites from the komatiites are similar to those of the chromites from the massive chromites.

Trace Elements

Gallium shows a negative correlation with Cr_2O_3 and has a single trend starting at a low of 24 ppm for the chromites from komatiite and the Bushveld sills through to a high for the UG-N chromites, at 60 to 70 ppm (Fig 9a). The chromite from the UG2-W and the UG1 do not fall on this trend. Gallium varies from 50 to 70 ppm in these chromites, but their Cr_2O_3 concentrations are almost constant at 42.5 to 44 weight %.

Scandium concentrations are generally low at <15 ppm and show no correlation with Cr_2O_3 (Fig. 9b). The chromites from Stillwater, the LG6, MG1, UG2-N and the sills of the Bushveld Complex, and Emeishan low-Ti picrites all contain very low Sc concentrations of <6 ppm. In contrast, chromites from the komatiites, the high-Ti picrites and from the MG3, UG1 and UG2-W of the Bushveld contain higher Sc, from 6 to 15 ppm.

For Sn, Hf, Nb and Ta, the data set is limited as the concentrations of these elements in chromite approach detection limits. Hafnium concentrations in the chromites from volcanic rocks show a broad negative correlation with Cr_2O_3, with concentrations ranging from 0.01 ppm in komatiites to 0.12 ppm in chromite from the Emeishan high-Ti picrites (Fig, 9c). The Hf concentrations in chromites from the intrusions do not show any clear relationship with Cr_2O_3. The chromites from the Stillwater Complex tend to have low Hf contents from less than detection limit to 0.04 ppm. In contrast, the LG6 and MG1 chromites are relatively rich in Hf at 0.1 to 0.12 ppm. The chromites from the Great Dyke and from the MG3, UG1 and UG2-W show a wide range of values, from 0.04 to 0.12 ppm.

As in the case of Hf, Sn values do not show a correlation with Cr_2O_3 (Fig. 9d). The chromites from the komatiites, the picrites, the Stillwater Complex and most Bushveld localities cover the range 0.1 to 0.6 ppm. The chromites from the Great Dyke are richer in Sn at 1 to 3 ppm. The time-resolved analysis signals were inspected to establish whether the Great Dyke values are due to inclusions, but the patterns were found to be homogeneous and thus it is assumed that the Great Dyke chromites contain elevated Sn levels.

Tantalum concentrations in chromites from the high-Ti picrites show a negative correlation with Cr_2O_3 and cover the range 0.005 ppm to 0.025 ppm (Fig. 9e). The Ta concentrations for most of the intrusion chromites are close to, or less than, the detection level (0.005 ppm). Exceptions to this are the Great Dyke and MG1 chromites. In both cases, Ta levels exceed 0.01 ppm. As in the case of Ta, Nb concentrations in chromites from the picrites appear to define a negative correlation with Cr_2O_3 (Fig. 9f), covering the range 0.05 to 0.25 ppm. The Nb contents of most intrusion chromites are close to, or less than, the detection level of <0.05 ppm.

Copper concentrations for most chromites are in the 1 to 10 ppm range. An exception to this are some of the chromites from the Emeishan picrites, which contain up to 300 ppm Cu.

Park et al. (2017) report similarly high Cu concentrations in chromites from Emeishan picrites and low Cu concentrations in chromites from komatiites. The Emeishan chromites show some zonation with respect to Cu concentrations (Barnes et al. 2022).

A number of other elements, namely Ge, Y, Zr, Cd, In and W were measured. Their concentrations are found either to be close to their detection limits or there are possible interferences that still need to be resolved. These elements will not be considered any further.

Discussion

Barnes (1998) studied the composition of chromites by considering: a) the influence of the composition of the magma from which chromite crystallized; b) the influence of post-crystallization re-equilibration with the trapped liquid fraction; c) the influence of sub solidus re-equilibration with the silicates during cooling; and d) the influence of metamorphism. More recently, workers have come to appreciate that cumulate systems are rarely closed and thus, after initial crystallization the chromite may have re-equilibrated with interstitial liquid that has replaced or mixed with the liquid from which the chromite crystallized. Thus process b) should more correctly be phrased as post-crystallization re-equilibration with liquid.

Partition Coefficients

In order to understand the influence of various processes on the composition of the chromite an estimation of the partition coefficients of the elements between chromite and liquids is helpful (Table 2). There are some results from experiments, and in addition, we have previously estimated partition coefficients based on the composition of the chromite from the Emeishan picrites and modelled Emeishan liquids (Barnes et al. 2022). For the current work, we have also calculated partition coefficients based on chromite from komatiite. To calculate the partition coefficients between komatiite and chromite one needs to estimate the composition of the komatiite liquid at the time of chromite crystallization. Both experimental and empirical evidence suggest that chromite only begins to crystallize when the MgO content of a komatiite liquid falls to ~ 20 to 25 weight % (Barnes 1998; Keltie 2018). Thus, chromite would not be on the liquidus in the initial komatiite liquid at Alexo, which contained 30 weight % MgO based on the composition of the hyaloclastite flow top (Barnes et al. 1983). To estimate the composition of the komatiite liquid at the time of chromite crystallization the composition of the spinifex textured sample (AX19) with the lowest MgO content (22 weight %) was used to estimate the liquid composition. The composition of AX19 can be modelled as the product of ~ 30 % crystal fractionation from the initial komatiite liquid (Barnes et al. 1983). The partition coefficients estimated for the komatiite chromite are similar to those of the Emeishan chromite (Table 2).

The empirical partition coefficients calculated for the 3+, 4+ and 5+ ions are similar to those from experimental work. The 2+ ions show more variable behavior. In our data set the empirical partition coefficients for Mg, Co, and Ni are lower than those deduced from experimental work. The partition coefficients of Mn, Fe and Zn are within the range of experimental partition coefficients. However, in the Emeishan picrites, concentrations of these elements were found to be significantly lower in chromites included in olivine than in chromites found in the matrix, which suggests that the latter have been modified from their primary compositions (Barnes et al. 2022). Furthermore, the composition of chromite in equilibrium with the modelled Emeishan liquid as calculated by SPINMELTS 2 (Nikolaev et al. 2018) is richer in MgO and poorer in FeOT than the observed chromite compositions, whereas the Cr_2O_3, TiO_2 and Al_2O_3 concentrations are similar to calculated values (Barnes et al. 2022). Therefore, in the following section we will assume that the 3+, 4+ and 5+ ions are the most representative of igneous compositions and that the 2+ ions may have been modified due to post-cumulate processes.

Metamorphism

In the current study none of the samples have experienced metamorphism above lower greenschist facies. Hence, as documented by Barnes (1998), metamorphic effects should be minimal, although he reports mobilization of Mn, Co and Zn during low grade alteration. Enrichment of Mn and Zn was identified along cracks in the chromites of the UG2 (Fig. 10) possibly reflecting this type of alteration. These zones have been excluded from analyses. The Mn concentrations of chromites from the Great Dyke reported by Wilson (1982) (those within the circle on Fig. 8c) are much higher than those reported from the Great Dyke by Mason-Apps (1998) and in our own samples. Samples from within 300 m of the current weathering surface of the Great Dyke have undergone serpentinization (Wilson and Prendergast 1987) and thus it is possible that the high Mn values are the result of this alteration. No clear evidence of Co mobility due to metamorphism or low temperature alteration was observed in our sample set.

Post crystallization re-equilibration with liquid and sub solidus re-equilibration

The composition of chromite from volcanic rocks is subject to two competing effects. On the one hand, the rocks cool quickly, therefore the opportunity for diffusion of ions and re-equilibration of chromite with melt is limited. On the other hand, the ratio of silicate material to chromite is high and therefore each chromite grain is in contact with silicate material with which it could re-equilibrate during cooling. The effects of re-equilibration on the chromite from Emeishan picrites have been considered by comparing chromite compositions from chromite included in olivine with those in the matrix (Barnes et al. 2022). Inclusion chromites are significantly richer in Mg and Co and poorer in Fe, Mn and Zn, whereas Al, Cr, Ti, Sc, V, Ga, Nb, Ta and Hf concentrations are similar in both types of chromite. These observations for the 2+ ions are in agreement with Barnes (1998), Roeder and Campbell (1985), and Scowen et al. (1991), who attribute the difference in concentrations to reaction between chromite and olivine. Barnes et al. (2022) showed that the 3+, 4+ and 5+ ions in chromite from Emeishan picrites do not appear to have re-equilibrated.

Barnes (1998) reported that in chromite from komatiites Mg#, and Ti, V, Mn, Co, Zn concentrations can be affected by reaction with trapped liquid. As outlined above, on the basis of a comparison of partition coefficients from experimental work and empirical partition coefficients calculated for the komatiite chromite from Alexo, the Mg, Fe, Co and Ni concentrations of chromite in the current study may be altered, but as in the case of the Emeishan study the 3+, 4+ and 5+ elements in the komatiite chromites do not appear to have been modified. The marginal sills of the Bushveld Complex contain <1 % chromite, and these chromites have similar compositions to the chromite from the Alexo komatiites in terms of 3+, 4+ and 5+ elements. The tendency of the 3+, 4+ and 5+ ions in the volcanic and sill rocks to maintain their initial concentrations may be because the chromite and liquid cooled relatively quickly and there was insufficient time for these elements to diffuse due to their slower diffusion rates (Coulthard et al. 2021)

The effects of re-equilibration on the chromite from within the intrusions require serious consideration. The chromite could have been in contact first with a fractionating liquid and subsequently with interstitial silicate minerals at high temperatures for a lengthy period. In addition, the exchange between chromite and interstitial silicate minerals may occur because the equilibrium constant has changed with temperature or because this mineral was not present at the time chromite initially crystallized.

The question of how much re-equilibration has occurred is often addressed by considering the amount of chromite in the rock. The logic behind this approach is that the more chromite is present, the less re-equilibration is possible. In the case of Stillwater, both the whole rock compositions of the chromite layers and the composition of the chromite are available. Therefore, the weight % chromite in each sample can be calculated and the possible influence of re-equilibration with silicate material evaluated.

Considering first the 2+ ions, there is an increase in Mn, Co and Zn concentrations in chromite from samples containing less than 40 weight % chromite (Figs. 11a to c). Nickel shows no clear trend (Fig. 11d). In contrast with the observations of Barnes (1998) for chromites from komatiites and Langa et al. (2020) for chromites from the UG2, where Mg# decreases as the portion of chromite present decreases, the Mg# of the Stillwater chromites does not show a clear trend (Fig. 11e). Chromite from samples with <40 modal % chromite from the C layers do have lower Mg# than chromite from the massive chromite layers. However, chromites from samples with <40 modal % chromite from the E, J, H and B layers have Mg# similar to the massive chromites (Fig. 11e).

The concentrations of Sc, V and Sn (all elements with a charge >2+) are similar in chromites from both massive and disseminated samples (Figs. 12a to c). For TiO_2 and Ga the results are variable. Concentrations of these elements are not enriched in disseminated chromites from zones E, H, B and J relative to chromites from massive chromites (Figs. 12d and e). However, TiO_2 and Ga concentrations in chromites from the C chromites are higher than the other chromites. The C chromite layers have a low concentration of chromite and also showed a low Mg#, thus enrichment could be due to sub solidus re-equilibration.

Niobium, Hf and Ta concentrations are uniform (not shown), but as they are close to detection levels no clear conclusion can be drawn. The Cr# is higher in the G layer than in the other layers, but there is no correlation with amount of chromite present (Fig. 12f). In summary, in rocks with >40 modal % chromite none of the elements appear to be disturbed. In rocks with <40 modal % chromite the 2+ ions Mn, Fe, Co and Zn are enriched in some of the chromite grains and MgO is depleted. The ions with >2+ charge do not appear to have re-equilibrated.

For most of the Bushveld chromite layers the exact amount of chromite in the samples has not been reported. However, Naldrett et al. (2012) describes their sample set as massive chromite, which implies that they contain at least 50 modal % chromite. Our MG1, MG3, UG1 and UG2 samples are all massive. In the case of our UG1 and UG2-W samples (where whole rock data is available) the weight % chromite present is calculated to be between 70 to 90 weight %, (depending on the sample) equivalent to 64 to 87 modal %. Langa et al. (2021) report that their UG2-W samples contain ~90 modal % chromite (except for 2 samples, which contain low concentrations). Langa et al. (2021) report that their UG2-N layer samples have a more variable chromite content (~2 to 90 modal %) and that the Mg# is constant and >0.4 in rocks containing >40 modal % chromite, but decreases in rocks with <40 modal % chromite.

In order to assess the potential for re-equilibration of the various elements, and because the amount of chromite present in each rock is not always reported, following Langa et al. (2021), we have used Mg# as proxy for re-equilibration. Plots of Mg# versus elements with a 2+ charge show that concentrations of Mn, Co and Zn are higher in chromite with Mg# < 0.4 (Fig. 13a to c). In contrast, Ni does not show clear trends (Fig. 13d).

The behaviors of elements with a charge >2+ (Ti, Sc, V, G) are more variable (Fig. 14). Concentrations of TiO_2, V, Ga and Sc in chromites from the UG2-N with Mg# < 0.4 are higher than those with Mg# > 0.4. The relative increase is greatest for TiO_2 from ~ 1 weight % to 1.6 weight % and least for Ga from ~ 50 ppm to 70 ppm. These increases suggest that TiO_2, V, Sc and Ga have, as suggested by Langa et al. (2021), re-equilibrated in the rocks with <40 modal% chromite (Figs. 14a to d).

In contrast, there is no correlation between Mg# and Ti, V, Sc and Ga in the UG2-W and the other massive chromite layers, which suggests that there has not been re-equilibration in of these elements in the massive chromite layer. There is a notable difference in V content between the UG2-N chromites and the LG5 to UG2-W chromites. The latter are all much richer in V than the UG2-N and LG1 to LG4 chromites (Fig. 14b). As in the case of V, there is a difference in Sc contents of chromite from different chromite layers. The UG2-W, UG1 and MG3 chromites all cluster with relatively high Sc contents of 6 to 8 ppm, whereas chromites from the UG2-N, the LG6 and the Bushveld sills contain relatively low Sc, at 2 to 6 ppm (Fig. 14c).

Niobium, Sn, Hf and Ta (not shown) show no correlation with Mg#, but many samples are close to detection limits. Therefore, no reliable conclusions can be made. In summary, the UG2-N data show that in rocks with <40% modal chromite TiO_2, V, Sc and Ga in chromite are enriched, possibly due to post-crystallization re-equilibration.

The Great Dyke samples from our study are massive chromites from layers C8 and C6, (>75 weight % chromite based on whole rock composition) plus a sample from layer C1 (30 weight % chromite) and disseminated (1 weight %) chromite from the C1 harzburgites. A plot of Mg# vs Cr# shows a limited range of Cr# for the chromites from layers C1 to C12 (0.70 to 0.80) whereas the Mg# varies more widely 0.44 to 0.68 (Fig. 15a). The greater variability of the Mg#

suggests some re-equilibration may have taken place. If we further consider the change in Cr# and Mg# for chromite from layers where massive and disseminated chromite data are available (C1 and C6) we can see a decrease in both Cr# and Mg# in the disseminated chromite. The TiO_2 concentrations in chromites from massive chromite layers are fairly constant and do not vary with Mg# (Fig. 15b). However, the disseminated chromite from the C1 unit appears to be enriched in TiO_2, possibly due to re-equilibration. Nickel concentrations show no clear trends (Fig.15c). Insufficient data are available to track changes in Zn and Co, except to observe that the disseminated chromites of the C1 layer are enriched in these elements.

In summary, in rocks from within the intrusions where chromite concentrations are <40 modal %, elements with a 2+ charge may have undergone re-equilibration and are therefore not a reliable guide to the melt composition at the time of chromite crystallization. In rocks with chromite concentrations <25 modal %, elements with a charge >2+ may have undergone re-equilibration.

Composition of the parent liquids to the chromites

Variations of TiO_2, V, Ga and Sc with stratigraphic height.

Apart from the major elements, Ti is the element for which most data are available. Given that TiO_2 is incompatible with most of the minerals present (olivine, orthopyroxene and plagioclase, Table 3), but only slightly incompatible with regard to chromite (Table 2), the TiO_2 content of the chromite should rise as the magma evolves. Also, the TiO_2 concentrations of the chromites should be sufficiently high to be reliably determined, thus making it an indicator of fractionation of the liquid.

In the case of the Stillwater chromites the TiO_2 contents of the A and B chromite layers (Fig. 16a) are higher (0.6 to 0.7 weight %) than the TiO_2 contents of chromite from layers E and above (0.4 to 0.56 weight %). The C chromite is also relatively enriched in TiO_2 at 0.8 to 1.4 weight %, but as mentioned above the chromite content of this layer is low and thus this result is ambiguous. The relatively high TiO_2 in chromites from the lowest two chromite layers may be the result of contamination of the magma with continental crustal rocks. Initial Os isotopes from the lower chromite layers indicated more crustal contamination than in the layers above (Horan et al. 2001). The variations in TiO_2 content with height are mirrored by V and Ga (Figs. 16b and c) which are highest in the A to C chromites, lowest in the G chromite. The concentrations of TiO_2, V and Ga are higher in the H, I, J and K chromites than in the G chromites and the OB1 chromite contain intermediate concentrations. Scandium shows an inverse relationship with stratigraphic height and follows Cr# (Figs. 16d and e), with the highest levels being found in the G chromites and falling to lower levels in the J and K chromites, before rising slightly in the OB1 chromite. The variations in $TiO_{2,}$ V and Ga contents of the chromite in layers E and above are relatively small (varying by a factor of 1.4) suggesting that the TiO_2, V and Ga contents of the magma did not vary greatly during the formation of this section of the intrusion.

Chromites from massive layers of the Great Dyke have lower TiO_2 contents than chromites and show a narrow range than those from either the Stillwater Complex or Bushveld Complex at 0.25 to 0.45 vs 0.4 to 0.7 and 0.4 to 1.2 weight % TiO_2 respectively (Figs. 16 to 18). Concentrations in chromites vary slightly in the C12 to C5 units at 0.25 to 0.35 weight % (Fig. 17a). Concentrations in chromite from the upper chromite layers C2 and C1 are slightly higher at around 0.45 weight %. An exception to this is the concentration of TiO_2 in the disseminated chromite from the C1 unit, which is higher at around 1 weight %, possibly due to re-equilibration. Vanadium, Ga and Sc concentrations are only available from chromites C1, C6 and C8. Due to the limited dataset the variations with stratigraphic height will not be discussed here. As in the case of the Stillwater chromites, the TiO_2 content shows an inverse relationship with Cr#, with the highest Cr# in the lower parts of the intrusion and lower Cr# in the C1 and C2 chromites. Also, as in the case of the Stillwater chromites, the limited range in TiO_2 contents of the massive chromite indicates that the TiO_2 content of the magma did not vary greatly during the crystallization of the Ultramafic Sequence although it was slightly higher in the upper parts.

Both the TiO_2 and V contents of chromite from the Bushveld Complex show much wider ranges in concentrations than the Stillwater or Great Dyke chromites. TiO_2 and V concentrations in chromite increase by a factor of approximately three from the marginal sills to the UG2 chromtite (Figs.18a and b). The Cr# also covers a wider range (0.6 to 0.8) than at Stillwater (0.58 to 0.68) and Great Dyke (0.7 to 0.8) (Fig. 18c). For Ga and Sc the data set is more limited, but the concentrations in chromites of the UG2 are also approximately three times those of the sills (Table 1). These wider ranges in chromite compositions indicate that the Bushveld chromites equilibrated with magmas with a wider range of compositions than the Great Dyke and Stillwater chromites and that the magmas were progressively more evolved upwards in the stratigraphic section.

Variations of the elements across individual layers

As discussed in the introduction, many models for the formation of massive chromite layers propose that there is a sudden change in an intensive variable (pressure, compositional of the magma, fO_2), such that chromite became the dominant or sole mineral to crystallize. Brenan et al. (2022) in their investigation of the massive chromite layers from the Esker Intrusive

Complex (McFalls Lake greenstone belt of northwest Ontario, Canada) tested this model by considering the behavior of V versus Ga. Their hypothesis is based on the observation that both V and Ga partition into chromite, and thus if chromite is the dominant or sole mineral to crystallize, then the concentrations of these two elements should decrease across a massive chromite layer. However, because both elements are incompatible with the mafic silicates if chromite crystallized in cotectic proportions (~2%) with olivine or orthopyroxene, then the bulk partition coefficients for these elements would be much less than 1 (Table 3) and thus the concentrations of V and Ga should increase across the massive chromite layer. In the case of the Esker Complex they found that these elements increased across the massive chromite layer, which they interpret to indicate that the layer could not have formed by chromite-only crystallization, but instead formed by a combination of processes, beginning with cotectic crystallization of chromite and olivine followed by separation of chromite and silicates to form the chromite layer.

This hypothesis can be extended to other elements compatible with chromite. Thus, in addition to V and Ga, concentrations of Mn, Co, Ni and Zn should decrease across massive chromite layers if they formed by chromite-only crystallization, whereas concentrations of TiO_2 and Sc should increase. Cross-sections from the UG2-W at Waterval and from the UG2-W and UG1 at Impala mine show variable trends. In the Waterval section, V, Ga, Mn, Co, Ni and Zn all increase by approximately 20 relative % up-section (Figs. 19a to f) inconsistent with chromite-only crystallization. In their study of the Waterval section, Naldrett et al. (2012) also observed that V increased up-section. They nevertheless favored chromite-only crystallization and suggested that the increase in V content in the upper parts of the section was due to an increase in the partition coefficient of V into chromite. Although, they did not state this explicitly, such an increase in partition coefficient would require a decrease in fO_2. A change in fO_2 would not, however, change the partition coefficient for Ga and other elements and since the concentrations of a number of elements compatible with chromite increase up-section at Waterval, we do not think that the increase in V is due to a change in partition coefficient. In the case of the Impala UG2-W and UG-1 cross-sections there is very little systematic variation in the concentrations of V, Ga, Mn, Co, Ni or Zn (Figs. 19a to f) across the sections, which once again does not support chromite-only crystallization.

Influence of crystal fractionation on TiO_2, V, Ga and Sc for all chromites

Below we consider the influence of crystal fractionation on TiO_2, V, Ga and Sc during crystal fractionation for the whole data set. On plots of these elements against each other, vectors for the composition of chromite after 30 % cotectic crystal fractionation of chromite with olivine, orthopyroxene, clinopyroxene and plagioclase and chromite-only crystallization are shown (Fig. 20). In each case, the composition of an initial chromite was calculated using the bulk partition coefficients in Table 3. The composition of the liquid after 30 % crystal fractionation was calculated assuming 2 weight % chromite plus 98 weight % olivine or orthopyroxene or clinopyroxene or plagioclase, or 100 weight % chromite crystallization. Then the composition of chromite in equilibrium with this liquid was calculated using the partition coefficients in Table 2. For chromites from the layered intrusions, only the chromites from the massive chromites are shown due to the difficulty in assessing the influence of re-equilibration due changes in the liquid composition or exchange with the silicate minerals during cooling.

On the plot of TiO_2 versus Ga all of the chromites, except for those from the high-Ti picrite, plot on a single trend defined by cotectic crystallization of chromite plus olivine or orthopyroxene or clinopyroxene (Fig. 20a). The chromite from the high Ti-picrites plot on a parallel trend to the other chromites, but are slightly richer in TiO_2, implying a more TiO_2-rich parent magma than in the case of the other rocks. It is noteworthy that, despite the presence of primocryst plagioclase in the Upper Critical Zone of the Bushveld Complex, the chromites from this portion of the Bushveld do not appear to follow the plagioclase plus chromite vector, implying that the chromite and plagioclase did not crystallize at the same time.

On a plot of TiO_2 versus V, most of the chromites plot along cotectic vectors for chromite plus olivine or pyroxene, with the komatiite and Great Dyke chromite having the lowest TiO_2 and V concentrations, Stillwater chromites plotting at intermediate levels of TiO_2 and V, and most Bushveld chromites having the highest TiO_2 and V contents (Fig. 20b). Finally, the chromites from the high-Ti picrite are richer in TiO_2 than the other chromites and plot along a shallower trend. It is notable that the V content of all chromites from the Bushveld above the LG4 layer are enriched in V relative to chromite from other intrusions and the volcanic chromite. This implies that either the V content of the magma was much higher (2 to 3 times) than the magma that formed the LG1 to 4 and the UG2-N (and the chromite from other settings) or the partition coefficient for V into chromite was higher.

The oxidation state of V in crustal magmas varies from 3+ to 5+ and hence is sensitive to fO_2. Vanadium 3+ has a much higher partition coefficient into chromite than V^{5+} (Canil et al. 2001, Brenan 2022). Assuming that the V content of the parent magma of the UG2-N and UG-2W are similar and at approximately 200 ppm (based on the composition of the marginal rocks, Barnes et al. 2010) and applying the equation of Canil (2002)

$$\Delta NNO = \{\log[(V_{liq}/V_{chr})*24.1-1]-0.82\}/0.28$$

The fO_2 can be estimated as approximately -2 ΔFMQ and -1 ΔFMQ for the UG2-W and N, respectively. Similar conclusions for the difference in oxidation state of the UG2-W and N have also been drawn by Dyan (2021). Our estimates are somewhat lower than suggested by the $Fe^{3+}/\Sigma Fe$ ratio found by Langa et al. (2021), which suggests a range in fO_2 of between -1 ΔFMQ and 0. The difference in the estimations could be due to a number of factors including re-equilibration of Fe, or underestimation of V in the liquid. Alternatively, the equation of Canil et al. (2002) may not be directly applicable to the UG2 magma composition as the equation is based on a komatiitic magma, whereas the magma that formed the UG-2 was more evolved. Nonetheless, the point remains that fO_2 for the UG2-W appears to have been lower than fO_2 for the UG-2N and most other chromites.

On a plot of Sc versus Ga, the chromites from the komatiites and picrites form trends that are parallel to the olivine plus chromite vector, with the picritic chromite containing slightly more Ga than the komatiitic chromite (Fig. 20c). The Bushveld and Stillwater chromites are richer in Ga than the chromites from the volcanic rocks. This could reflect a higher Ga concentration in the parent magmas of the intrusions relative to the komatiites and picrites, which is consistent with the premise that parent magmas of the intrusions were contaminated with continental crust (Eales and Costin 2012; Horan et al. 2001; Jenkins and Mungall 2018; Maier et al. 2016), because the continental crust is enriched in Ga relative to Sc. It is also notable that the UG2-N chromites are depleted in Sc relative to the UG2-W and other chromites from the Critical Zone. This relative Sc-depletion of the UG2-N chromites could be explained by the crystallization of primocryst clinopyroxene which is a common phase in the northern limb. In contrast to the remainder of the Bushveld where clinopyroxene typically forms an intercumulus phase. The early appearance of cumulus augite in the northern limb is consistent with the generally pervasive contamination of the northern limb magmas by assimilation of footwall shale and carbonate. The two chromite layers from the Dunite Succession of the Great Dyke plot with the komatiites and the chromite from the Stillwater intrusion. As in the case of the TiO_2 versus Ga plot it is noteworthy that the Upper Critical Zone chromites do not plot along a chromite plus plagioclase vector.

Turning to the plot proposed by Brenan et al (2022) of V versus Ga (Fig. 20d), most chromites fall on a single trend of increasing V and Ga. Chromites from komatiites, low-Ti picrites and the Bushveld marginal sills have the lowest concentrations of V and Ga, whereas chromite from the UG2, both in the northern and western limb, have the highest concentrations of Ga. As noted above, the Upper Critical Zone chromites are richer in V than other chromites and on this plot cluster together at a higher level than the general trend.

Overall, on the plots of Ti, Sc, V and Ga, the samples do not appear to fall along chromite-only crystallization vectors and thus do not support models that require only chromite on the liquidus to form massive chromite.

Multi-Element Plots

For the data set as a whole, only MgO shows a positive correlation with Cr (Figs. 7 to 9). The positive correlation between MgO and Cr_2O_3 in these massive chromites is in contrast to chromites inclusions in olivine from volcanic settings (Kamenetsky et al. 2001), but is in agreement with experimental work (Keltie 2018). We suggest that this difference arises because the ratio of chromite to silicate component in massive chromites is much lower than in chromite inclusions in olivine. Thus the massive chromites have undergone re-equilibration to a lesser degree than the inclusion chromites. The positive correlation between MgO and Cr and the negative correlation between the remaining elements and Cr indicates that the bulk partition coefficient for MgO during crystal fractionation was greater than 1 but for the other elements was less than one.

This observation can be used to design a multi-element plot to compare the composition of the chromites. On this plot the elements have been normalized to chromite in komatiite sample AX37. This is the LabMaTer in-house standard that has been analyzed over 200 times and thus we are confident of the values, listed in Table 1. The elements are plotted in order of their bulk partition coefficient, assuming 2 weight % chromite and 98 weight % olivine (Table 3). From Ni to Zn the elements are controlled by olivine or pyroxene. If only olivine and chromite crystallize then V and Ga are controlled by chromite and Sc, Hf, $TiO_{2,}$ and Sn should reflect the liquid compositions. If pyroxene has crystallized the concentrations of Sc and V could be lower. If plagioclase crystallized, Ga will be depleted. Contamination of komatiite magma with average continental crustal increases the Sn, Hf, and Ga concentrations.

Chromites from komatiite have approximately flat patterns ranging from 0.5 to 2 times the AX 37 standard (Fig. 21a). The chromites from the low-Ti picrites show similar patterns, but tend to have slightly higher Hf and Ti values (Fig. 21b). The chromites from the high-Ti picrite show similar trace element patterns to komatiites from Ga to Ni, at 1 to 2 times the komatiite. However, they are strongly enriched in Hf and Ti, at 3 to 10 times komatiite and slightly enriched in Sn at 2 to 3 times komatiite (Fig. 21c). As discussed by Barnes et al. (2022), the high-Ti picrite liquids are enriched in Ti, Hf and Sn, and the chromites reflect this.

The shape of the chromite patterns from all of the intrusions show an enrichment in Hf and, in some cases Sn, relative to the other elements, and all chromites except those from the Dunite Succession of the Great Dyke show strong negative Sc anomalies (Figs. 22 and 23). The concentrations of most elements from the massive chromite layers C8 and 6 from the Dunite

Succession of the Great Dyke are low, similar to komatiites, and the overall patterns are flat, apart from enrichment in Hf and Sn (Fig 22a). Elements such as Zn and, in some cases Ni, have even lower concentrations, down to 0.4 times komatiite. This pattern is consistent with the Great Dyke chromites having formed from a komatiitic liquid that has experienced some contamination with continental crust, which would have enriched the magma in Hf and Sn. The two chromites from the C1 unit of the Bronzitite Succession are semi-massive and disseminated (Fig. 22a). They have similar patterns to the chromites from the C8 and C6 chromite layers except that the C1 chromites have negative Sc anomalies and are richer in most elements (except Ni). The negative Sc anomalies could be the result of crystallization of pyroxene. The depletion in Ni could be due to olivine crystallization. The higher levels of the other elements that have bulk partition coefficients of less than 1 (Sn, Hf, Ti, Ga and V) may be the result of enrichment in the magma by crystal fractionation. However, Zn, Mn and Co have bulk partition coefficients close to 1 and would thus not be expected to be enriched. As discussed above these elements are susceptible to enrichment by reaction with the silicates and the enrichment of these elements could thus be due to sub solidus re-equilibration as these rocks contain only 30 weight % chromite.

The chromites from the massive chromites of the Stillwater Complex, including the massive chromite from the OB1 unit at the level of the JM Reef, exhibit essentially similar patterns (Fig. 22b). From Zn to Ni they overlap with the komatiite patterns. There is a slight enrichment from V through to Ti at 2 to 3 times komatiite, but with a large negative Sc anomaly. Hafnium concentrations are variable from 1 to 4 times komatiite. In some chromites, Sn is strongly enriched at up to 5 times komatiite levels. The negative Sc anomaly suggests that the chromite has equilibrated with a liquid that crystallized pyroxene. Although it is commonly thought that the interstitial mineral to the chromite at Stillwater is olivine, both olivine and orthopyroxene are present. The ratio of olivine to orthopyroxene in the chromite layers can be estimated using a plot of MgO versus Sc for the whole rock compositions (Fig. 24). This indicates that most of the chromite layers contain olivine and orthopyroxene in a ratio of ~1:1, consistent with the premise that pyroxene crystallization has controlled the Sc content the chromite. The chromite from the semi-massive C layer shows slightly higher concentrations of Ti, Ga, Mn, Co and Ni than the other layers. As discussed above, this enrichment could have occurred due to sub-solidus re-equilibration or could be due to equilibration with a more fractionated liquid.

The patterns of chromite from the marginal sills of the Bushveld Complex show Zn to Ni being present at approximately the level of komatiite chromite, a negative Sc anomaly and a strong enrichment in Sn, Hf and to a lesser extent Ti (Fig. 23a). The cumulate minerals in the marginal sills are olivine and orthopyroxene. The pyroxene probably controlled the Sc. Overall, the enrichment in Sn and Hf relative to the other elements suggests a strong crustal component in the liquid.

The Bushveld chromites from the LG1 to MG2 layers show similar shaped patterns to the chromites from the marginal sills, but are slightly enriched in Hf to V and depleted in Zn to Ni (Fig. 23a). The chromites from the MG3, MG4 and UG1 also show similar shaped patterns, except that they are more enriched in Ti to V (Fig. 23b). The overall enrichment in elements from Ti to V and depletion in elements from Zn to Ni relative to the chromites from the marginal sills and komatiite is consistent with equilibration with a more evolved magma.

If we consider only the massive chromites from the UG2-W and the UG2-N, the patterns are similar in shape and level to the UG1 chromites (Fig. 23c). However, the UG2-N chromites contain slightly less Sc, V, Co and Ni and more Zn and Ti.

Summary of the assessment of the composition of the liquids

Of the analyzed samples, the chromites of the Great Dyke from the Dunite Succession are the richest in Cr and have compositions closest to komatiite, apart from the enrichment in Sn and Hf. This supports the idea that the chromites have equilibrated with magma of komatiitic composition. The compositions of the chromites from the Bronze Succession are slightly poorer in Cr and richer in Ga, V and Ti, and have negative Sc anomalies. These characteristics suggest that the chromites equilibrated with a liquid that was enriched in elements incompatible with olivine, and that the liquid was sufficiently evolved to crystallize pyroxene. Overall, the compositions of the chromites are consistent with a komatiitic liquid that was slightly contaminated with continental crust.

Of all the chromites examined, the Stillwater chromites have the highest Al_2O_3 contents, except for a few of the chromites from the Bushveld UG1 layer. The multi-element patterns of the Stillwater chromites are similar to those from the Bronzitite Succession of the Great Dyke, suggesting that the magma was more evolved than the initial magma of the Great Dyke. The chromites could have equilibrated with a komatiite magma contaminated with continental crust (as suggested for the Stillwater silicate rocks; Jenkins and Mungall 2018) but the negative Sc anomalies suggest that chromite composition has been influenced by the presence of orthopyroxene. Interpreting the relative timing of crystallization of the olivine, orthopyroxene and chromite depends on one’s interpretation of how the orthopyroxene oikocrysts formed.

Jackson (1961) argued that they are the product of a peritectic reaction of fractionated liquid with olivine. On the other hand, orthopyroxene crystallization could have been delayed relative to olivine crystallization due to the differences in energy of nucleation. In this case, crystallization of orthopyroxene would have been rapid and would have engulfed the pre-existing olivine and chromite grains once the energy barrier was overcome. This topic is beyond the scope of the current work. However, the influence of orthopyroxene on the chromite composition seems reasonable as in most samples chromite is not included in olivine, but is either included in orthopyroxene or interstitial to both orthopyroxene and olivine (Fig. 3e).

Bushveld chromites cover a wider range of compositions than either the Great Dyke or Stillwater chromite. The chromites from the floor sills and the LG1 to LG4 chromite layers are similar in composition to chromite from komatiite magmas, but have negative Sc anomalies and enrichment in Sn and Hf. The initial magma at the Bushveld is thought to be a komatiite contaminated with a large amount of upper crust (Barnes et al. 2010, Eales and Costin 2012, Maier et al. 2016; Wilson 2012) and would be a suitable liquid to crystallize these chromites. At the level of the UG2 layer, the concentration of elements incompatible with olivine and orthopyroxene (Hf, Ti, Ga, Sc and V) has increased by factors two to three. If this change were simply brought about by crystal fractionation then 50 to 66 % crystal fractionation would be required and the liquid composition would not be appropriate to crystallize chromite. Therefore, other process(es) are needed to enrich these chromites in the incompatible elements. One possible model is outlined below.

Formation of a massive chromite layer

The various models that require chromite-only crystallization are not consistent with variations in Ga, V, Ti and Sc throughout the dataset and across individual massive chromite layers, namely the UG2 and UG1. This suggests that models invoking changes in intensive variables, such as pressure, composition and/or fO_2 to form massive chromite layers are not viable. The variations in these elements are consistent with crystallization of chromite and mafic minerals in cotectic proportions. This requires a mechanism to separate the chromite and most of the silicate minerals after crystallization.

We suggest a more elaborate model involving semi-consolidated cumulates containing cotectic proportions of chromite slumped towards the center of the intrusions. (This model does not preclude settling of chromite clusters at a particular stage.) The slumping model is consistent with the variation in thickness of the layers. For example, Wilson and Prendergast (1989) pointed out that in the Great Dyke the chromite layers are thin and disseminated at the margins of the intrusion but thicken and become more massive towards the center. Similar types of structures can be observed on the thin section scale at Stillwater (Fig. 3f). The slumping model is also consistent with complex structures observed in some layers observed both at Stillwater and the Bushveld. For example the UG1 layer at Dwars River of the Bushveld is famous for the complex structures associated with it. There is ample evidence for disruption of the layers, such as anorthosites clasts within the chromite layers (Fig. 5c) and chaotic layering beneath the layer (Fig. 5d) and the bifurcation of the chromite layers. These complex structures are not confined to Dwars River. Nex (2004) documents these features from six localities around the western and eastern limbs of the Bushveld and attributes them to liquefaction of the underlying unconsolidated anorthosites caused by major magma influx and associated seismicity. We suggest that the magma(s) in question is actually a chromite slurry which either slumped from the side walls of the chamber or formed in a feeder chamber at depth and was then emplaced into the chamber.

The reason for slumping could be the collapse of the floor of the chamber due to melting and/or mobilization of the country rock at the base of the intrusion. Alternatively, it could be the result of a fresh injection of magma accompanied by earthquakes. It should be noted that the slumping was not necessarily a single event. There could have been repeated events, and as shown by Forien et al.'s (2016) experimental work, this could result in younger surges injecting into older cumulates, thereby thickening layers. Slumping could also explain the lack of variation in chromite composition across the 1 m thick UG1 and 2 layers at Impala and the anomaly of plagioclase oikocrysts enclosing chromites. Fractional crystallization of the B1 magma could produce chromite of the observed Cr# and Mg# but plagioclase would not have been on the liquidus at the point at which chromite crystallizes. In this model the layers formed by injection of a chromite-orthopyroxene slurry into a semi-consolidated anorthosite. During transport the chromite collected at the base of the slurry. There would be little compositional change across the section because any variations due to crystal fractionation have been obscured by the mixing of the grains during transport. A second process that should be considered is that in order for the slurry to move it would needed to have contained at least 30% liquid. Furthermore, if the underlying anorthosite still contained a liquid this interstitial anorthosite liquid would have been more fractionated than the slurry liquid and not in equilibrium with the chromite. During compaction the slurry liquid and anorthosites liquid could mix and pass through the chromite slurry causing re-equilibration of the chromite to a broadly similar composition across the beds and enriching the chromite in incompatible elements. This mixed liquid could also have crystallized the plagioclase oikocrysts.

Conclusions

The concentrations of elements with a charge >2+ (Al, Sc, Ti, Cr, V, Ga, Nb, Sn, Hf and Ta) in disseminated chromites from volcanic rocks (Alexo komatiite and Emeishan picrites) and the marginal sills of the Bushveld Complex reflect the composition of the melts they crystallized from. The elements with a 2+ charge appear to have been disturbed after initial crystallization. This could occur during equilibrium crystallization, whereby the chromite consistently re-equilibrated with the fractionating magma. Alternatively, it could occur after solidification, due to changes in the partition coefficients between the silicate minerals and chromite as the temperature fell. Both processes are aided by the high silicate to oxide ratio in the volcanic rocks and the fast diffusion coefficients for these elements.

The variations in the concentrations of elements with >2+ charge in chromite from komatiite and picrite plot along olivine plus chromite crystallization trends and the multi-element patterns are similar, except that the high-Ti picrites are enriched in Sn, Hf and Ti, reflecting the composition of the magmas.

Disseminated chromites from the intrusions show enrichment in Mn, Fe, Co, Zn and, to a lesser extent, Ti, V and Ga. As in the case of the volcanic rocks this can be attributed to re-equilibration of the initial chromite with a more fractionated liquid or due to post-solidification re-equilibration with the surrounding silicate minerals. The concentrations of these elements in chromite from massive chromites layers from the same settings are fairly constant suggesting that they have not re-equilibrated.

With the exception of the chromite from the Dunite Succession of the Great Dyke the intrusion chromites all have negative Sc anomalies on multi-element plots, interpreted to be due to pyroxene crystallization. On the multi-element plots all of the intrusion chromites are enriched in Hf and, in some cases, Sn relative to the other elements. This is attributed to contamination of a komatiitic parent magma with continental crust.

On plots of V, Ti, Ga and Sc the chromites from the intrusions follow vectors defined by chromite plus olivine or pyroxene in cotectic proportions. This is inconsistent with models of chromite-only crystallization. Furthermore, variations in the changes in concentrations of these elements across the individual layers of massive chromite (UG2 and UG1 layers) do not support the hypothesis of chromite-only crystallization. We favor the formation of the chromite layers by slumping of a slurry of chromite, pyroxene and/or olivine onto and into semi-consolidated cumulates during which the chromite is concentrated at the base of the slurries. After coming to rest the residual liquids from the slurry and the underlying cumulate may mix resulting in some re-equilibration of the chromite as the mixed liquid rises through the chromite layer.

Acknowledgements

SJB would like to thank Canadian Journal of Earth Science for the invitation to submit a review manuscript on a subject of her choice. Two reviewers (Dr. Chris Jenkins and Dr. Vadim Kamenetsky) are thanked for their reviews and the editor for handling the manuscript. This work was supported by a Natural Science and Engineering Discovery grant (*1884-2013*) and the Canada Research Chair grant (*(215503)* to SJB. In addition, support for the komatiite chromite project was provided by the Geological Survey of Canada with a Targeted Geoscience Initiative 4 (TGI-4) grant. Northam Platinum is thanked for access to the MG1 and MG3 samples. The Stillwater samples were collected under the guidance of Dr. Mike Zientek of the United States Geological Survey and with the help of Dr. Philippe Pagé of IOS Services Géoscientifiques, Chicoutimi, both are warmly thanked. Mr. Dany Savard, Ms. Audrey Lavoie and Dr. Christopher Beckett-Brown are thanked for their support of laboratory work.

Competing interests: The authors declare there are no competing interests.

Roles of the authors

Sarah-Jane Barnes, -principal author, sample collection komatiites, Great Dyke, Bushveld LG6, marginal sills

Eduardo Mansur LA-ICP-MS data collection except komatiites, editing and figure drafting

Wolfgang Maier Sample collection Bushveld UG1, UG2, geological setting information, editing

Steve Prevec Sample collection MG1 and MG3, geological setting information, editing and figure 4.

References.

Arai, S. 1997. Origin of podiform chromitites. Journal of Asian Earth Sciences **15**(2-3): 303-310.

Arguin, J.-P., Pagé, P., Barnes, S.-J., Yu, S.-Y., and Song, X.-Y. 2016. The effect of chromite crystallization on the distribution of osmium, iridium, ruthenium and rhodium in picritic magmas: an example from the Emeishan Large Igneous Province, Southwestern China. Journal of Petrology **57**(5): 1019-1048.

Alapieti, T.T., Kujanpaa, J., Lahtinen, J.J., and Papunen, H. 1989. The Kemi stratiform chromitite deposit, northern Finland. Economic Geology **84**(5): 1057-1077.

Arunachellan, Y. (2022) Constraints on Cr-PGE Mineralisation: Geochemistry and Petrology of the Middle Group 1 and 3 Chromitites, Western Limb, Bushveld Complex, South Africa. Unpublished Masters thesis, Rhodes University, Makhanda, South Africa. 123 p.

Barnes, S.-J., Gorton, M.P., and Naldrett, A.J. 1983. A comparative study of olivine and clinopyroxene spinifex flows from Alexo, Abitibi greenstone belt, Ontario, Canada. Contributions to Mineralogy and Petrology **83**(3-4): 293-308.

Barnes, S.-J., Maier, W.D., and Curl, E.A. 2010. Composition of the Marginal Rocks of the Rustenburg Layered Series, Bushveld Complex, South Africa: Implications for the Formation of the Platinum-Group Element Deposits. Economic Geology **105**(8): 1491-1511

Barnes, S.-J., Pagé, P., Prichard, H.M., Zientek, M.L., and Fisher, P.C. 2016. Chalcophile and platinum-group element distribution in the ULtramafic series of the Stillwater Complex, MT, USA—implications for processes enriching chromite layers in Os, Ir, Ru, and Rh. Mineralium Deposita **51**(1): 25-47

Barnes, S.-J., Mansur, E.T., and Pagé, P. 2022. Differences in composition of chromites from low-Ti and high-Ti picrites of the Emeishan Large Igneous Province and comparison with chromites of the UG-2 platinum-deposit of the Bushveld complex. Lithos **412**: 106613.

Barnes, S.J. 1998. Chromite in komatiites, 1. Magmatic Controls on Crystallization and Composition. Journal of Petrology **39**(10): 1689-1720.

Barnes, S.J. 2000. Chromite in komatiites, II. Modification during greenschist to mid-amphibolite facies metamorphism. Journal of Petrology **41**(3): 387-409.

Barnes, S.J., and Roeder, P.L. 2001. The range of spinel compositions in terrestrial mafic and ultramafic rocks. Journal of Petrology **42**(12): 2279-2302.

Bédard, J.H. 2005. Partitioning coefficients between olivine and silicate melts. Lithos **83**(3-4): 394-419.

Bédard, J.H. 2006. Trace element partitioning in plagioclase feldspar. Geochimica Cosmochimica Acta **70**(14): 3717-3742. doi: 10.1016/j.g

Bédard, J.H. 2007. Trace element partitioning coefficients between silicate melts and orthopyroxene: Parameterizations of D variations. Chemical Geology **244**(1-2): 263-303.

Bédard, J.H. 2014. Parameterizations of calcic clinopyroxene—Melt trace element partition coefficients. Geochemistry, Geophysics, Geosystems **15**(2): 303-336.

Brenan, J.M., Finnigan, C.F., McDonough, W.F., and Homolova, V. 2012. Experimental constraints on the partitioning of Ru, Rh, Ir, Pt and Pd between chromite and silicate melt: the importance of ferric iron. Chemical Geology **302**: 16-32.

Brenan, J.M., Woods, K., Mungall, J.E., and Weston, R. 2022 Origin of chromitites in the Esker Intrusion Complex, Ring of Fire Intrusive Suite, as revealed by chromite trace element chemistry and simple crystallization models. Geological Survey of Canada Open File 8755 p. 1-19.

Brough, C., Prichard, H.M., Neary, C., Fisher, P.C., and McDonald, I. 2015. Geochemical variations within podiform chromitite deposits in the Shetland Ophiolite: Implications for petrogenesis and PGE concentration. Economic Geology **110**(1): 187-208.

Campbell, I.H., and Murck, B.W. 1993. Petrology of the G and H chromitite zones in the Mountain View area of the Stillwater Complex, Montana. Journal of Petology **34**: 291-316.

Cameron, E. 1980. Evolution of the Lower Critical Zone, central sector, eastern Bushveld Complex, and its chromite deposits. Economic Geology **75**(6): 845-871.

Canil, D. 2002. Vanadium in peridotites, mantle redox and tectonic environments: Archean to present. Earth and Planetary Science Letters **195**(1): 75-90.

Cawthorn, R.G., 2005. Pressure fluctuations and the formation of the PGE-rich Merensky and chromitite reefs, Bushveld Complex. Mineralium Deposita **40**(2): 231-235.

Cawthorn, R.G., and Walraven, F. 1998. Emplacement and crystallization time for the Bushveld Complex. Journal of Petrology **39**(9): 1669-1687.

Cawthorn, R.G., Barnes, S.J., Ballhaus, C., and Malitch, K. 2005. Platinum Group Element, Chromium, and Vanadium Deposits in Mafic and Ultramafic Rocks. *In* Economic Geology 100th Anniversary Volume. *Editors* J.W. Hedenquist, J.F.H. Thompson, R.J. Goldfarb and J.P. Richards. Society Economic Geologist. p. 215-249.

Chaumba, J.B., and Musa, C.T. 2020. Geochemistry of the chromitite stringer at the contact of the mafic sequence and the ultramafic sequence in the Unki Mine area, Shurugwi Subchamber of the Great Dyke, Zimbabwe. The Canadian Mineralogist **58**(3): 313-333.

Cooper, R.W. 1997. Magmatic unconformities and stratigraphic relations in the Peridotite zone, Stillwater Complex, Montana. Canadian Journal of Earth Sciences **34**(4): 407-425.

Coulthard, D.A., Zellmer, G.F., Tomiya, A., Jégo, S., and Brahm, R. 2021. Petrogenetic implications of chromite-seeded boninite crystallization experiments: Providing a basis for chromite-melt diffusion chronometry in an oxybarometric context. Geochimica Cosmochimica Acta **297**: 179-202.

Dyan, S. 2021 Constraining the role of carbonate assimilation on spinel stability in oxide ores of the Flatreef, Bushveld Complex, South Africa, Unpub Masters thesis Rhodes University, Makhanda, South Africa, 183 pp.

Eales, H.V. 2000. Implications of the chromium budget of the Western Limb of the Bushveld Complex. South African Journal of Geology **103**(2): 141-150.

Eales, H.V., and Cawthorn, R.G. 1996. The Bushveld Complex. *In* Layered Intrusions. *Editor* R.G. Cawthorn. Elsevier, Amsterdam. pp. 181-229.

Eales, H.V., and Costin, G. 2012. Crustally contaminated komatiite: primary source of the chromitites and Marginal, Lower, and Critical Zone magmas in a staging chamber beneath the Bushveld Complex. Economic Geology **107**(4): 645-665.

Engelbrecht, J.P. 1985. The chromites of the Bushveld Complex in the Nietverdiend area. Economic Geology **80**(4): 896-910.

Forien, M., Tremblay, J., Barnes, S.-J., Burgisser, A., and Page, P. 2015. The role of viscous particle segregation in forming chromite layers from slumped crystal slurries: insights from analogue experiments. Journal of Petrology **56**(12): 2425-2444.

Gain, S.B. 1985. The geologic setting of the platiniferous UG2 chromitite layer on Maandagshoek, Eastern Bushveld Complex. Economic Geology **80**: 925-943.

González-Jiménez, J.M., Griffin, W.L., Proenza, J.A., Gervilla, F., O'Reilly, S.Y., Akbulut, M., Pearson, N.J., and Arai, S. 2014. Chromitites in ophiolites: How, where, when, why? Part II. The crystallization of chromitites. Lithos **189**: 140-158.

Grobler, D. F., Brits, J., Maier, W.D., and Crossingham, A. 2019. Litho-and chemostratigraphy of the Flatreef PGE deposit, northern Bushveld Complex. Mineralium Deposita **54**(1): 3-28.

Hall, A.L. 1932. The Bushveld Igneous Complex in the central Transvaal. Geological Society, South Africa. p. 544.

Horan, M.F., Morgan, J.W., Walker, R.J., and Cooper, R.W. 2001. Re–Os isotopic constraints on magma mixing in the Peridotite zone of the Stillwater complex, Montana, USA. Contributions to Mineralogy and Petrology **141**(4): 446-457.

Horn, I.H., and Jenner, G. A. 1994. Compositional dependencies of the partition coefficients for Zr, Nb, Ta, Hf and selected transition elements between spinel and melt. Geochim. Cosmochim. Acta **51**: 1071-1081.

Houlé, M.G., Lesher, C.M., and Davis, P.C. 2012. Thermomechanical erosion at the Alexo Mine, Abitibi greenstone belt, Ontario: implications for the genesis of komatiite-associated Ni–Cu–(PGE) mineralization. Mineralium Deposita **47**(1): 105-128.

Hulbert, L., and von Gruenewaldt, G. 1985. Textural and compositional features of chromite in the lower and critical zones of the Bushveld Complex south of Potgietersrus. Economic Geology **80**(4): 872-895.

Irvine, T.N. 1975. Crystallization sequences in the Muskox Intrusion and other layered complexes-origin of chromitite layers and similar deposits of other magmatic ores. Geochimica Cosmochimica Acta **39**: 991-1020.

Irvine, T.N. 1977. Origin of chromitite layers in the Muskox intrusion and other stratiform intrusions II.: a new interpretation. Geology **5**: 273-277.

Irvine, T.N. 1979. Rocks whose composition is determined by crystal accumulation and sorting. *In* The Evolution of the Igneous rocks: Fiftieth Anniversary perspectives. *Editor* H.S. Yoder. Princeton University Press, Princeton. pp. 245-306.

Irvine, T.N 1980. Magmatic density currents and cumulus processes. American Journal of Science **280**: 1-58.

Jackson, E.D. 1961. Primary Textures and Mineral Associations in the Ultramafic Zone of the Stillwater Complex, Montana: US Geol. Survey Prof. Paper 358, 106 p.

Jenkins, M.C., and Mungall, J.E. 2018. Genesis of the Peridotite zone, Stillwater Complex, Montana, USA. Journal of Petrology **59**(11): 2157-2189.

Jolly, W.T. 1982. Progressive metamorphism of komatiites and related Archean lavas of the Abitibi area, Canada. *In* Komatiites. *Editors* Arndt, N. T., and Nisbet, E.G., Geoge Allen and Unwin, London, U.K. p. 247-266.

Junge, M., Oberthür, T., and Melcher, F. 2014. Cryptic variation of chromite chemistry, platinum group element and platinum group mineral distribution in the UG-2 chromitite_ An example from the Karee mine, western Bushveld Complex, South Africa. Economic Geology **109**: 795-810.

Kamenetsky, V.S., Crawford, A.J., and Meffre, S. 2001. Factors controlling chemistry of magmatic spinel: an empirical study of associated olivine, Cr-spinel and melt inclusions from primitive rocks. Journal of Petrology **42**: 655-671.

Kamenetsky, V.S., Park, J.-W., Mungall, J.E., Pushkarev, E.V., Ivanov, A.V., Kamenetsky, M.B., and Yaxley, G.M. 2015. Crystallization of platinum-group minerals from silicate melts: Evidence from Cr-spinel–hosted inclusions in volcanic rocks. Geology **43**: 903-906.

Kaufmann, F.E., Vukmanovic, Z., Holness, M.B., and Hecht, L. 2018. Orthopyroxene oikocrysts in the MG1 chromitite layer of the Bushveld Complex: implications for cumulate formation and recrystallisation. Contributions to Mineralogy and Petrology **173**: 1-20.

Keltie, E., E. 2018. An experimental study of the role of contamination in the formation of chromitites in the Ring of Fire intrusive suite. Unpublished masters thesis., Dalhousie University, Halifax 133 p

Kinnaird, J.A., Kruger, F.J., Nex, P.A.M., and Cawthorn, R.G. 2002. Chromitite formation—a key to understanding processes of platinum enrichment. Applied Earth Science **11**1: 23-35.

Langa, M.M., Jugo, P.J., Leybourne, M.I., Grobler, D.F., Adetunji, J., and Skogby, H. 2021. Chromite chemistry of a massive chromitite seam in the northern limb of the Bushveld Igneous Complex, South Africa: correlation with the UG-2 in the eastern and western limbs and evidence of variable assimilation of footwall rocks. Mineralium Deposita **56**(1): 31-44.

Latypov, R., Chistyakova, S., and Mukherjee, R. 2017. A novel hypothesis for origin of massive chromitites in the Bushveld Igneous Complex. Journal of Petrology **58**(10): 1899-1940.

Latypov, R., Chistyakova, S., Barnes, S.J., Godel, B., Delaney, G.W., Cleary, P.W., Radermacher, V.J., Campbell, I., and Jakata, K. 2022. Chromitite layers indicate the existence of large, long-lived, and entirely molten magma chambers. Scientific Reports **12**(1): 1-15.

Lesher, C.M., Carson, H., and Houlé, M. 2019. Genesis of chromite deposits by dynamic upgrading of Fe±Ti oxide xenocrysts. Geology **47**(3): 207-210.

Lipin, B.R. 1993. Pressure increases, the formation of chromite seams, and the development of the ULtramafic series in the Stillwater Complex, Montana. Journal of Petology **34**: 955-976.

Liu, T.-C., and Presnall, D.C. 1990. Liquidus phase relationships on the join anorthite-forsterite-quartz at 20 kbar with applications to basalt petrogenesis and igneous sapphirine. Contributions to Mineralogy and Petrology **104**(6): 735-742.

Locmelis, M., Pearson, N.J., Barnes, S.J., and Fiorentini, M.L. 2011. Ruthenium in komatiitic chromite. Geochimica Cosmochimica Acta **75**(13): 3645-3661.

McCallum, I.S. 2002. The Stillwater Complex: A review of the geology. *In* 9th International Platinum Symposium Geology and Guide Stillwater Complex, Montana, USA, Billings. pp.A1-A25.

McCallum, I.S., Raedeke, L.D., and Mathez, E.A. 1980. Investigations of the Stillwater Complex: Part I. Stratigraphy and structure of the Banded zone. American Journal Science **280**: 59-87.

McLaren, C.H., and De Villiers, J.P. 1982. The platinum-group chemistry and mineralogy of the UG-2 chromitite layer of the Bushveld Complex. Economic Geology **77**(6): 1348-1366.

Maier, W.D, and Barnes, S.-J. 2008. Platinum-group elements in the UG1 and UG2 chromitites, and the Bastard reef, at Impala platinum mine, western Bushveld Complex, South Africa: Evidence for late magmatic cumulate instability and reef constitution. South African Journal of Geology **111**(2-3): 159-176.

Maier, W.D., Barnes, S.-J., and Groves, D. 2013. The Bushveld Complex, South Africa: formation of platinum–palladium, chrome-and vanadium-rich layers via hydrodynamic sorting of a mobilized cumulate slurry in a large, relatively slowly cooling, subsiding magma chamber. Mineralium Deposita **48**(1): 1-56.

Maier, W.D., Barnes, S.-J., and Karykowski, B. 2016. A chilled margin of komatiite and Mg-rich basaltic andesite in the western Bushveld Complex, South Africa. Contributions to Mineralogy and Petrology **171**(6): 1-22.

Maier, W.D., Yudovskaya, M., and Jugo, P. 2021. Introduction to the special issue on the Flatreef PGE-Ni-Cu deposit, northern limb of the Bushveld Igneous Complex. Mineralium Deposita **56**(1): 1-10.

Manoochehri, S., and Schmidt, M.W. 2014. Settling and compaction of chromite cumulates employing a centrifuging piston cylinder and application to layered mafic intrusions. Contributions to Mineralogy and Petrology **168**(6): #1091.

Marsh, J.S., Pasecznyk, M.J., and Boudreau, A.E. 2021. Formation of chromitite seams and associated anorthosites in layered intrusion by reactive volatile-rich fluid infiltration. Journal of Petrology **62**(2):1-23.

Mason-Apps, A.D. 1998. The petrology and geochemistry of the lower pyroxenite succession of the Great Dyke in the Mutorashanga area, Unpublished masters thesis Rhodes University 199p.

Meric, J. 2018. Le ruthénium (Ru), iridium (Ir), osmium (Os) et rhodium (Rh) et les éléments traces dans des chromites de komatiites issues de la zone Alexo et de la zone Hart,(Abitibi, Ontario): un outil diagnostique pour l'exploration de systèmes fertiles. Unpublished masters thesis Université du Québec à Chicoutimi. 202 p.

Mondal, S.K., and Mathez, E.A. 2007. Origin of the UG2 chromitite layer, Bushveld Complex. Journal of Petrology **48**(3): 495-510.

Mondal, S.K., Khatun, S., Prichard, H.M., Satyanarayanan, M., and Kumar, G.R. 2019. Platinum-group element geochemistry of boninite-derived Mesoarchean chromitites and ultramafic-mafic cumulate rocks from the Sukinda Massif (Orissa, India). Ore Geology Reviews **104**: 722-744.

Mosier, D.L., Singer, D.A., Moring, B.C., and Galloway, J.P., 2012, Podiform chromite deposits—database and grade and tonnage models: U.S. Geological Survey Scientific Investigations Report 2012-5157, 45 p.

Murck, B.W., and Campbell, I.H. 1986. The effects of temperature, oxygen fugacity and melt composition on the behaviour of chromium in basic and ultrabasic melts. Geochimica Cosmochimica acta **50**(9): 1871-1887.

Naldrett, A.J., Kinnaird, J., Wilson, A., Yudovskaya, M., McQuade, S., Chunnett, G., and Stanley, C. 2009. Chromite composition and PGE content of Bushveld chromitites: Part 1–the Lower and Middle Groups. Applied Earth Science: Transactions of the Institutions of Mining and Metallurgy: Section B **118**(3-4): 131-161.

Naldrett, A.J. 2011. Fundamentals of magmatic sulfide deposit. *In* Magmatic Ni-Cu and PGE deposits: Geology, Geochemistry, and Genesis. *Editors* C. Li and E.M. Ripley. Society of Economic Geologists Lillteton. pp. 1-50.

Naldrett, A.J., Wilson, A., Kinnaird, J., Yudovskaya, M., and Chunnett, G. 2012. The origin of chromitites and related PGE mineralization in the Bushveld Complex: new mineralogical and petrological constraints. Mineralium Deposita **47**(3): 209-232.

Nex, P.A.M. 2004. Formation of bifurcating chromitite layers of the UG1 in the Bushveld Igneous Complex, an analogy with sand volcanoes. Journal of the Geological Society **161**(6): 903-909.

Nicholson, D.M., and Mathez, E.A. 1991. Petrogenesis of the Merensky Reef in the Rustenburg section of the Bushveld Complex. Contributions to Mineralogy and Petrology **107**: 293-309.

Nicklas, R.W., Puchtel, I.S., and Ash, R.D. 2016. High-precision determination of the oxidation state of komatiite lavas using vanadium liquid-mineral partitioning. Chemical Geology **433**: 36-45. doi: https://doi.org/10.1016/j.chemgeo.2016.04.011.

Nikolaev, G.S., Ariskin, A.A., and Barmina, G.S. 2018. SPINMELT-2.0: Simulation of spinel–melt equilibrium in basaltic systems under pressures up to 15 kbar: II. Description of the program package, the topology of the Cr-spinel–melt model system, and petrological implications. Geochemistry International **56**(2): 125-135.

Oberthür, T. 2002. Platinum-group element mineralization of the Great Dyke, Zimbabwe. . *Dans* The Geology, Geochemistry, Mineralogy and Mineral Beneficiation of Platinum-Group Elements. *Editor* L.J. Cabri. Canadian Institute of Mining, Metallurgy and Petroleum, Special Vol 54. pp. 483-506.

Oberthür, T. 2011. Platinum-group element mineralization of the main sulfide zone, Great Dyke, Zimbabwe. Reviews in Economic Geology **17**(12): 329-349.

O'Driscoll, B., Donaldson, C.H., Daly, J.S., and Emeleus, C.H. 2009. The roles of melt infiltration and cumulate assimilation in the formation of anorthosite and a Cr-spinel seam in the Rum Eastern Layered Intrusion, NW Scotland. Lithos **111**(1-2): 6-20.

Page, N.J. 1977. Stillwater Complex, Montana; rock succession, metamorphism and structure of the complex and adjacent rocks. US Geological Survey Professional Paper 999: 79 p.

Pagé, P., and Barnes, S.-J. 2009. Using trace elements in chromites to constrain the origin of podiform chromitites in the Thetford Mines ophiolite, Québec, Canada. Economic Geology **104**(7): 997-1018.

Pagé, P., and Barnes, S.-J. 2016. The influence of chromite on osmium, iridium, ruthenium and rhodium distribution during early magmatic processes. Chemical Geology **420**: 51-68.

Pagé, P., Barnes, S.-J., Bédard, J.H., and Zientek, M.L. 2012. In situ determination of Os, Ir, and Ru in chromites formed from komatiite, tholeiite and boninite magmas: implications for chromite control of Os, Ir and Ru during partial melting and crystal fractionation. Chemical Geology **302-303**: 3-15.

Park J-W, Campbell I.H., and Eggins S.M. 2012. Enrichment of Rh, Ru, Ir and Os in Cr spinels from oxidized magmas: evidence from the Ambae volcano, Vanuatu. . Geochimica Cosmochimica Acta **78**: 28-50.

Park, J.-W., Kamenetsky, V., Campbell, I., Park, G., Hanski, E., and Pushkarev, E. 2017. Empirical constraints on partitioning of platinum group elements between Cr-spinel and primitive terrestrial magmas. Geochimica Cosmochimica Acta **216**: 393-416.

Paton, C., Hellstrom, J., Paul, B., Woodhead, J., and Hergt, J. 2011. Iolite: Freeware for the visualisation and processing of mass spectrometric data. Journal of Analytical Atomic Spectrometry **26**(12): 2508-2518.

Prevec, S.A. 2019. The Bushveld Complex, South Africa: New Insights and Paradigms. Geoscience Canada. **45**: 117-135.

Prevec, S.A., Largatzis, S.A., Brownscombe, W., and Salge, T. 2021. PGE distribution in Merensky wide-reef facies of the Bushveld Complex, South Africa: Evidence for localized hydromagmatic control. The Canadian Mineralogist **59**(6): 1305-1338.

Prichard, H.M., Barnes, S.-J., Fisher, P.C., Pagé, P. and Zientek, M.L. 2017. Laurite and associated PGM in the Stillwater chromitites: implications for processes of formation, and comparisons with laurite in the Bushveld and ophiolitic chromitites. The Canadian Mineralogist **55**(1): 121-144.

Righter, K., Campbell, A.J., Humayun, M., and Hervig, R.L. 2004. Partitioning of Ru, Rh, Pd, e, Ir and Au between Cr-bearing spinel, olivine, pyroxene and silicate melts. Geochimica and Cosmochimica Acta **68**: 867-880.

Roeder, P.L., and Campbell, I.H. 1985. The effect of postcumulus reactions on composition of chrome-spinels from the Jimberlana intrusion. Journal of Petrology **26**(3): 763-786.

Roeder, P.L. and Reynolds, I. 1991 Crystallization of chromite and chromium solubility in basaltic melts. Journal of Petrology **32**(5): 909-934.

Roeder, P.L., Gofton, E., and Thornber, C. 2006. Cotectic proportions of olivine and spinel in olivine-tholeiitic basalt and evaluation of pre-eruptive processes. Journal of Petrology **47**(5): 883-900.

Scoates, J.S., Wall, C.J., Friedman, R.M., Weis, D., Mathez, E.A., and Van Tongeren, J.A. 2021. Dating the Bushveld Complex: Timing of Crystallization, Duration of Magmatism, and Cooling of the World's Largest Layered Intrusion and Related Rocks. Journal of Petrology **62**(2): https://doi.org/10.1093/petrology/egaa107

Scoon, R.N., and Teigler, B. 1994. Platinum-group element mineralization in the critical zone of the western Bushveld Complex; I, Sulfide poor-chromitites below the UG-2. Economic Geology **89**(5): 1094-1121.

Scowen, P.A.H., Roeder, P.L., and Helz, R.T. 1991. Reequilibration of chromite within Kilauea Iki lava lake, Hawaii. Contributions to Mineralogy and Petrology **107**(1): 8-20.

Schulte, R.F., Taylor, R.D., Piatak, N.M., and Seal, R.R., II, 2012, Stratiform chromite deposit model, chap. E *of* Mineraldeposit models for resource assessment: U.S. Geological Survey Scientific Investigations Report 2010–5070–E, 131 p.

Spandler, C., Mavrogenes, J., and Arculus, R. 2005. Origin of chromitites in layered intrusions: Evidence from chromite-hosted melt inclusions from the Stillwater Complex. Geology **33**(11): 893-896.

Todd, S.G., Keith, D.W., Le Roy, L.W., Schissel, D.J., Mann, E.L., and Irvine, T.N. 1982. The JM platinum-palladium reef of the Stillwater Complex, Montana; I, Stratigraphy and petrology. Economic Geology **77**(6): 1454-1480.

Ulmer, G.C. 1969. Experimental Investigations of Chromite Spinels. *In* Magmatic Ore Deposits. *Editor* H.D.B. Wilson. Society of Economic Geologists, Monograph 4, pp 114–131

U.S. Geological Survey, 2021, Mineral commodity summaries 2021: U.S. Geological Survey, 200 p., https://doi.org/10.3133/mcs2021

Veksler, I.V., and Hou, T. 2020. Experimental study on the effects of H2O upon crystallization in the Lower and Critical Zones of the Bushveld Complex with an emphasis on chromitite formation. Contributions to Mineralogy and Petrology **175**(9): 1-17.

Voordouw, R.J., Gutzmer, J., and Beukes, N.J. 2010. Zoning of platinum group mineral assemblages in the UG2 chromitite determined through in situ SEM-EDS-based image analysis. Mineralium Deposita **45**(2): 147-159.

Wagner, P.A. 1923. The chromite of the Bushveld igneous complex. South African Journal of Science **20**(1): 223.

Wall, C.J., Scoates, J.S., Weis, D., Friedman, R.M., Amini, M., and Meurer, W.P. 2018. The Stillwater Complex: integrating zircon geochronological and geochemical constraints on the age, emplacement history and crystallization of a large, open-system layered intrusion. Journal of Petrology **59**(1): 153-190.

Wijbrans, C.,H,, Klemme, S., Berndt, J., and Vollmer, C. 2015. Experimental determination of trace element partition coefficients between spinel and silicate melt: the influence of chemical composition and oxygen fugacity. Contributions to Mineralogy and Petrology **169**(4): 1-33.

Wilson, A.,H. 1982. The geology of the Great 'Dyke', Zimbabwe: the ultramafic rocks. Journal of Petrology **23**(2): 240-292.

Wilson, A.,H., and Prendergast, M.D. 1987. The Great Dyke of Zimbabwe--an overview. Guidebook for the 5th Magmatic Sulphides Field Conference (Harare: Geological Society of Zimbabwe), 94p.

Wilson, A.H., and Prendergast, M.D. 1989. The Great Dyke of Zimbabwe: I-tectonic setting, stratigraphy, petrology, structure, emplacement and crystallization. *Editor* M. Jones *In* Magmatic sulphides; the Zimbabwe volume. pp. 1-20

Wilson, A.H. 2012. A Chill Sequence to the Bushveld Complex: Insight into the First Stage of Emplacement and Implications for the Parental Magmas. Journal of Petrology **53**(6): 1123-1168. doi: 10.1093/petrology/egs011.

Wooden, J.L., Czamanske, G.K., and Zientek, M.L. 1991. A lead isotopic study of the Stillwater Complex, Montana: constraints on crustal contamination and source regions. Contributions to Mineralogy and Petrology **107**(1): 80-93. doi: 10.1007/BF00311186.

Worst, B.G. 1960. The Great Dyke of Southern Rhodesia. Government printer.

Xu, Y., Chung, S.-L., Jahn, B.-m., and Wu, G. 2001. Petrologic and geochemical constraints on the petrogenesis of Permian–Triassic Emeishan flood basalts in southwestern China. Lithos **58**(3-4): 145-168.

Zhou, M.-F., Robinson, P.T., Su, B.-X., Gao, J.-F., Li, J.-W., Yang, J.-S., and Malpas, J. 2014. Compositions of chromite, associated minerals, and parental magmas of podiform chromite deposits: The role of slab contamination of asthenospheric melts in suprasubduction zone environments. Gondwana Research **26**(1): 262-283.

Zientek, M.L., Cooper, R.W., Corson, S.R., and Geraghty, E.P. 2002. Platinum-group element mineralization in the Stillwater Complex, Montana. *In* Geology, Geochemistry, Mineralogy and Mineral Benefication of Platinum Group Element. *Editor* L.J. Cabri. Canadian Institute of Mining, Metallurgy and Petroleum, Special Publication vol **54**. pp. 459-481.

Zientek, M.L. 2012. Magmatic ore deposits in layered intrusions - Descriptive model for reef-type PGE and contact-type Cu-Ni-PGE deposits. Open File Report 2012-10 U.S. Geological Survey 48p.

Figure Captions

Fig. 1 Chrome resources and production 2021 data from U.S. Geological Survey, 2021, Mineral commodity summaries 2021.

Fig. 2 a) Map of the Stillwater Complex showing the principal units and the location of the traverses sampled. Modified after Todd et al. (1982) and Zientek et al. (2002). Dashed line J-M reef. b) Stratigraphic section through the Stillwater Complex, S = two minor sulfide occurrences

Fig 3 Stillwater chromites: a) E zone with chromite doublet showing narrow layers, host rock type pyroxenite; b) G chromite showing thick bottom layer overlain by a number of thin layers, host rock type peridotite; c) Reflected light photomicrograph of chromites showing large chromite grains with triple junctions and smaller euhedral chromite grains; d) Transmitted light photomicrograph of a chromite-rich peridotite (B layer) showing chromite and olivine inclusions in orthopyroxene oikocrysts e) Transmitted light photomicrograph of E chromite layers in pyroxenite. Note the slumping of the bottom layer.

Fig. 4 a) Map of the Bushveld Complex and b) Stratigraphic section through the Bushveld Complex modified after Prevec (2019).

Fig. 5 a) Transmitted light photomicrograph of the UG2 chromite (Bushveld) showing chromite grains with interstitial plagioclase. b) Transmitted light photomicrograph of UG2 chromite in orthopyroxene oikocrysts. c) UG1 chromite layer at Dwars River showing anorthosites base with sharp contact with a thick chromite layer containing anorthosites fragments overlain by alternating anorthosites and chromite layers, which are in turn overlain by a pyroxenite of the next unit. d) Example of the disrupted layering below the UG1.

Fig. 6 a) Map of the Great Dyke after Oberthür, (2011) b) Stratigraphic cross section of Great Dyke modified after Wilson and Prendergast (1989).

Fig 7 Plots of Cr_2O_3; versus a) MgO, b) FeOT and c) Al_2O_3 concentrations in chromite.

Fig 8 Plots of Cr_2O_3 versus; a) TiO_2, b) V, c) Mn, d) Zn, e) Co and f) Ni concentrations in chromite. Legend as on Fig. 7

Fig. 9 Plots of Cr_2O_3 versus; a) Ga, b) Sc, c) Hf, d) Sn, e) Ta and f) Nb concentrations in chromite. Legend as on Fig. 7.

Fig 10 Oxide and element distributions in a UG2-W chromite grain (sample BC16). Note most elements do not show zonation. Manganese and Zn are enriched along cracks in the chromite. Ti-rich laths reflect the presence of small ilmenite exsolutions in the chromite. Scale bar 0.5 mm.

Fig. 11 Plots of weight % chromite in whole rock vs a) Mn, b) Co, c) Zn, d) Ni and e) Mg# in chromite from Stillwater. Note that for rocks containing <40 weight% chromite Mn, Co and Zn higher than for the massive chromite.

Fig. 12 Plots of weight % chromite in whole rock versus; a)V, b) Sc, c) Sn, d) TiO_2, e) Ga, and f) Cr# for chromites from Stillwater. Note that for most chromites the concentrations are similar, exceptions to this are TiO_2 and Ga concentrations, which are higher the C chromite.

Fig. 13 Plots of Mg# chromite versus a) Mn, b) Co, c) Zn and d) Ni concentrations in chromites from the Bushveld Complex. Note that chromites with Mg# <0.4 are enriched in Mn, Co and Zn relative to chromites with Mg#>0.4 from the same chromite layer.

Fig. 14 Plots of Mg# in chromite versus a) TiO_2, b) V, c) Sc and d) Ga concentrations in chromites from the Bushveld Complex.

Fig. 15 Plots of Mg# in chromite versus a) Cr#, b) TiO_2 and c) Ni for chromites from the Great Dyke.

Fig. 16 Variations in; a) TiO_2, b) V, c) Ga, d) Sc and e) Cr# of chromites in the chromites layers of the Stillwater Complex. Note TiO_2, V and Ga show the same variations with height and Sc and Cr# show the opposite trends. The chromites are spaced out evenly across the 2.5 km section and not at their true stratigraphic height.

Fig. 17 Variations in TiO_2 and Cr# of chromites in the chromites layers of the Great Dyke. The chromites are spaced out evenly across the 2 km section and not at their true stratigraphic height.

Fig. 18 Variations in a) TiO_2, b) V, and c) Cr# of chromites in the chromites layers of the Bushveld Complex. The chromites are spaced out evenly across the 2.5 km section and not at their true stratigraphic height.

Fig. 19 Variations in; a) V, b) Ga, c) Mn, d) Co e) Ni and f) Zn across the UG2 at Waterval Mine and Impala and the UG1 at Impala. Note the elements do not decrease as they would if chromite only crystallized.

Fig. 20 Plots of TiO_2 versus, a) Ga, b) V and Ga vs c) Sc and d) Ga to illustrate the effects of olivine, orthopyroxene, clinopyroxene and chromite crystallization. Legend as on Fig. 7.

Fig 21 Chromite compositions normalized to komatiite chromite; a) Alexo chromites, b) Emeishan chromites from Lo-Ti picrites, c) Emeishan chromites from Hi-Ti picrites.

Fig 22 Chromite compositions normalized to komatiite chromite; a) Great Dyke chromites, b) Stillwater chromites

Fig 23 Chromite compositions normalized to komatiite chromite; a) Bushveld Complex sills and Lower Critical Zone chromites, b) MG3, MG4 and UG1 chromites c) UG2-W and UG2-N chromites.

Fig. 24 Plot of MgO versus Sc for whole rock compositions of the ultramafic series of the Stillwater Complex. Illustrating that most of the chromite-rich rocks contain olivine and orthopyroxene in the ratio of approximately 1:1.

Table 1. Representative analyses of chromites

Locality		Alexo		Emeishan			Bushveld				Great Dyke		Stillwater	
Rock type		cpx spin	B-zone	Lo-Ti	Hi-Ti	sill	LG6	MG3	UG1	UG2	C8	C1d	A	G1
Sample		AX 43	AX 37	BC 06	JC 03	DI 326	BC 13	27B	1184.4	1154.8	GD 3	GD 5	ST 7A	ST 11G1
							Microprobe Analyses							
MgO	wt %	13.27	13.74	14.34	10.62	7.50	9.12	8.01	8.95	9.11	13.66	9.17	9.70	10.78
Al2O3	wt %	15.62	13.48	16.55	14.77	11.20	13.94	16.78	17.41	17.14	12.31	14.66	18.74	15.42
SiO2	wt %	0.09	0.12	0.23	0.08	0.22	0.08	0.02	0.01	0.02	0.23	0.16	0.02	0.02
FeOT	wt %	19.14	16.48	20.82	28.21	27.18	26.90	29.02	27.42	27.76	14.69	25.32	28.74	26.04
Cr2O3	wt %	51.32	54.08	47.56	44.75	53.25	47.90	43.25	44.42	43.82	58.96	50.05	40.18	46.01
FeO	wt %	14.45	12.72	13.18	19.29	22.17	20.42	22.30	21.51	21.16	13.26	20.62	20.24	18.16
Fe2O3	wt %	5.22	4.18	8.49	9.91	5.57	7.20	7.47	6.57	7.33	1.59	5.22	9.45	8.76
Mg#		0.62	0.66	0.66	0.50	0.38	0.44	0.39	0.43	0.43	0.65	0.44	0.46	0.51
Cr#		0.69	0.73	0.66	0.67	0.76	0.70	0.63	0.63	0.63	0.76	0.70	0.59	0.67
Fe3+/(FeT)		0.25	0.23	0.37	0.32	0.18	0.24	0.23	0.22	0.24	0.10	0.19	0.30	0.30
							LA-ICP-MS Analyses							
Sc	ppm	7.97	7.00	7.18	10.20	1.83	4.98	6.43	7.89	8.26	4.70	5.64	4.63	5.00
Ti	ppm	2176	1501	3227	8255	970	4252	3996	4974	5103	1638	3090	4356	3410 ,
V	ppm	1145	790	583	1175	922	2240	2413	2956	2904	766	1731	2066	1273
Mn	ppm	1318	1395	1516	2099	2512	2358	1871	1872	1769	1133	2256	1761	1550
Co	ppm	221	240	233	251	395	397	289	329	330	230	478	287	281
Ni	ppm	1029	1176	1675	1312	600	1125	1000	1182	1262	1239	751	1188	1158
Cu	ppm	4.22	6.60	33.40	70.34	27.93	1.18	3.96	1.83	1.16	2.50	1.26	1.46	2.33
Zn	ppm	771	608	403	630	952	802	753	717	708	322	869	731	556
Ga	ppm	33.6	28.0	36.0	43.0	20.7	54.2	57.8	65.3	55.5	35.6	50.7	50.3	46.1
Nb	ppm	nd	0.170	0.039	0.084	0.028	0.055	0.016	0.108	0.138	0.056	0.102	0.027	0.020
Sn	ppm	0.275	0.100	0.108	0.298	0.238	0.158	0.247	0.097	0.117	0.909	0.241	0.229	0.221
Hf	ppm	0.016	0.020	0.028	0.071	0.024	0.125	0.046	0.060	0.086	0.087	0.113	0.068	0.021
Ta	ppm	0.002	0.003	0.019	0.008	0.003	0.065	0.006	0.001	0.006	0.024	0.031	0.006	0.006

cpx spin = clinopyroxene spinifex layer, Lo-Ti=Low-Ti picrite, Hi-Ti=high-Ti picrite, FeOT=Total Fe expressed as FeO

FeO, Fe2O3, Mg#, Cr#, Fe3+/FeT calculated using Barnes and Roedder (2001) , nd=not determined.

Table 2. Estimation of partition coefficients between calculated liquids and chromite

	High-Ti Picrite		Low Ti-picrites		ol spin flow		Literature Values		
	ave	σ	ave	σ	ave	σ			
n	20		16		6		Min	Max	Ref
Al	1.09	0.17	1.24	0.18	1.56	0.07	0.94	2.70	1,2,3,4
Cd	<0.5		<0.5		nd				
Co	2.71	0.44	2.63	0.21	2.32	0.31	3.30	5.10	2,4,5
Cr	388	124	325	132	107	9	128	270	1,2,3,4
Cu	0.74	0.86	0.66	0.55	0.17	0.02	0.17	0.25	2
Fe	2.69	0.38	2.31	0.40	1.66	0.31	1.25	4.75	1,2,3,4
Ga	3.21	0.74	2.54	0.70	3.20	0.43	2.40	3.80	2,5,6
Hf	0.024	0.013	0.016	0.004	0.022	0.009	0.004	0.008	2
In	0.49	0.14	0.36	0.09	0.62	0.27			
Mg	0.80	0.13	0.84	0.26	0.53	0.10	1.00	2.09	1,2,3,4
Mn	1.45	0.32	1.50	0.39	0.71	0.12	0.70	1.53	1,2,3,4,5
Nb	0.010	0.015	0.005	0.002	nd	nd	0.001	0.002	2
Ni	4.96	2.18	2.77	1.21	1.36	0.27	5.00	18.60	1,2,5
Sc	0.24	0.08	0.16	0.08	0.18	0.04	0.13	0.30	2,4,5
Sn	0.20	0.15	0.13	0.04	0.63	0.08			
Ta	0.009	0.011	0.005	0.004	0.083	0.069	0.001	0.002	2
Ti	0.83	0.17	0.54	0.09	0.60	0.05	0.14	0.78	1,2,3,4,5
V	4.35	0.65	2.92	0.87	4.39	0.60	1.00	10.00	2,4,5,6
Y	0.001	0.000	0.001	0.001	0.003	0.005			
Zn	5.71	1.72	6.47	2.23	8.85	2.36	6.90	10.10	5

n=number of samples, nd = not determined

1 Righer et al. (2004), 2 Wijbrans et al. (2015), 3 Brenan et al. (2012)

4 Horn and Jenner (1994), 5 Page et al. (2009), 6 Brenan et al. (2021)

Table 3. Calculation of bulk partition coefficients

	Partition coefficent used					Bulk D assuming				
	Chr	Ol	Opx	Cpx	Plag	Chr	Ol+chr	Opx+chr	Cpx+chr	Plag+chr
Ref		1,5	2	3	4	100%	98+2%	98+2%	98+2%	98+2%
Ni	5.00	3.3	0.69	2	0.08	5.000	3.334	0.776	2.060	0.178
Co	3.00	1.6	1	1.2	0.09	3.000	1.628	1.040	1.236	0.148
Mn	1.42	1	1.5	1		1.416	1.008	1.498	1.008	0.028
Zn	6.00	0.70	0.60	0.79		6.000	0.806	0.708	0.894	0.120
V	4.30	0.02	0.15	3.1	0.02	4.300	0.106	0.233	3.124	0.106
Sc	0.20	0.12	0.44	3.9	0.02	0.200	0.122	0.435	3.826	0.024
Ga	3.00	0.04	0.17	0.35	1	3.000	0.099	0.227	0.403	1.040
Ti	0.65	0.01	0.11	0.34	0.07	0.650	0.023	0.121	0.346	0.082
Ta	0.01	0.01	0.004	0.01	0.07	0.007	0.010	0.004	0.010	0.069
Hf	0.02	0.005	0.037	0.33	0.01	0.021	0.005	0.037	0.324	0.010
Cu	0.20					0.200	0.004	0.004	0.004	0.004
Sn	0.18					0.176	0.004	0.004	0.004	0.004
Nb	0.01		0.03	0.008	0.03	0.006	0.000	0.030	0.008	0.030

1 Bédard (2005), 2 Bédard (2007) 3 Bédard (2014) 4 Bédard (2006) 5 Brenan et al. (2021)

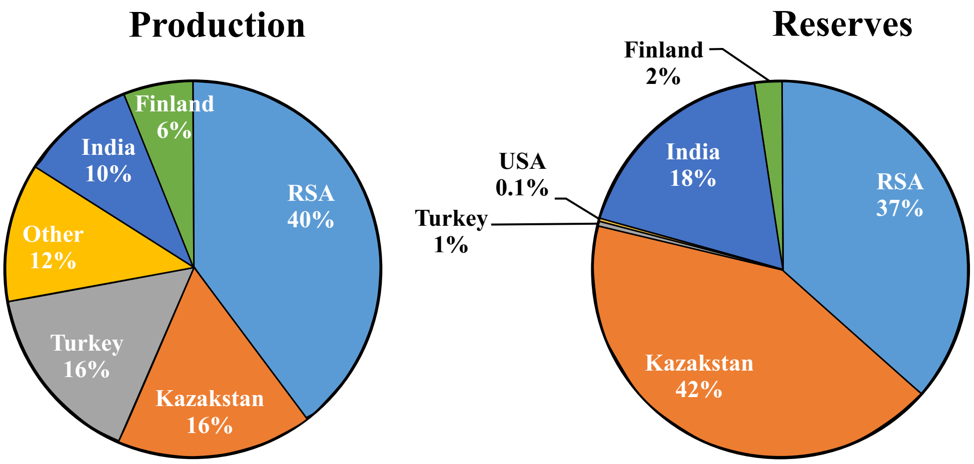
Production
RSA
40%
Kazakstan
16%
Turkey
16%
Other
12%
India
10%
Finland
6%
Reserves
Finland
2%
USA
0.1%
Turkey
1%
India
18%
RSA
37%
Kazakstan
42%

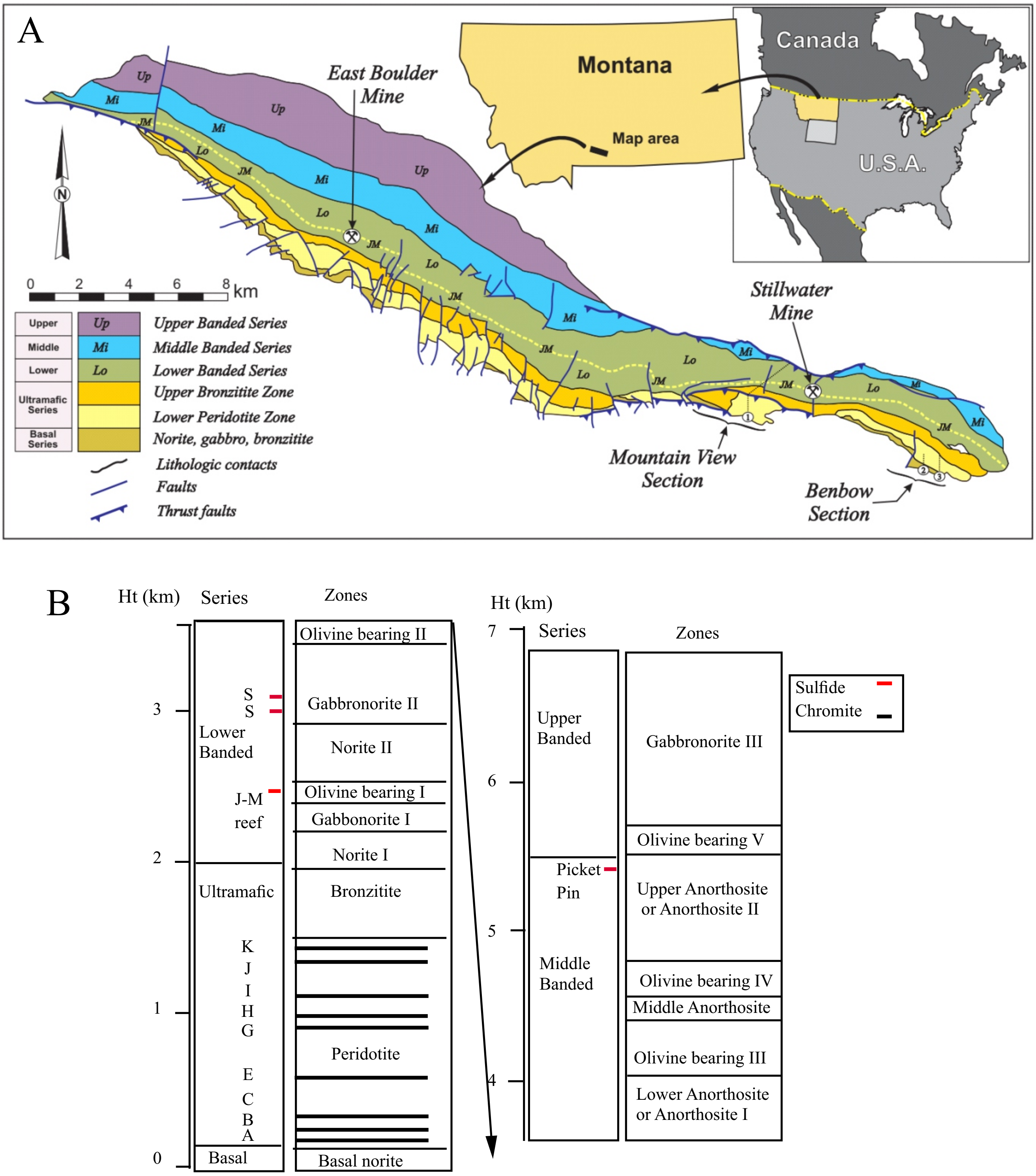
A
East Boulder Mine
Montana
Map area
Canada
U.S.A.
N
0 2 4 6 8 km
Up
Mi
JM
Lo
Upper | Up | Upper Banded Series
Middle | Mi | Middle Banded Series
Lower | Lo | Lower Banded Series
Ultramafic Series | Upper Bronzitite Zone
Lower Peridotite Zone
Basal Series | Norite, gabbro, bronzitite
Lithologic contacts
Faults
Thrust faults
Stillwater Mine
Mountain View Section
Benbow Section
①
②
③
B
Ht (km)
Series
Zones
0
1
2
3
Basal
Ultramafic
Lower Banded
S
S
J-M reef
K
J
I
H
G
E
C
B
A
Olivine bearing II
Gabbronorite II
Norite II
Olivine bearing I
Gabbonorite I
Norite I
Bronzitite
Peridotite
Basal norite
Ht (km)
4
5
6
7
Series
Zones
Upper Banded
Picket Pin
Middle Banded
Gabbronorite III
Olivine bearing V
Upper Anorthosite or Anorthosite II
Olivine bearing IV
Middle Anorthosite
Olivine bearing III
Lower Anorthosite or Anorthosite I
Sulfide
Chromite

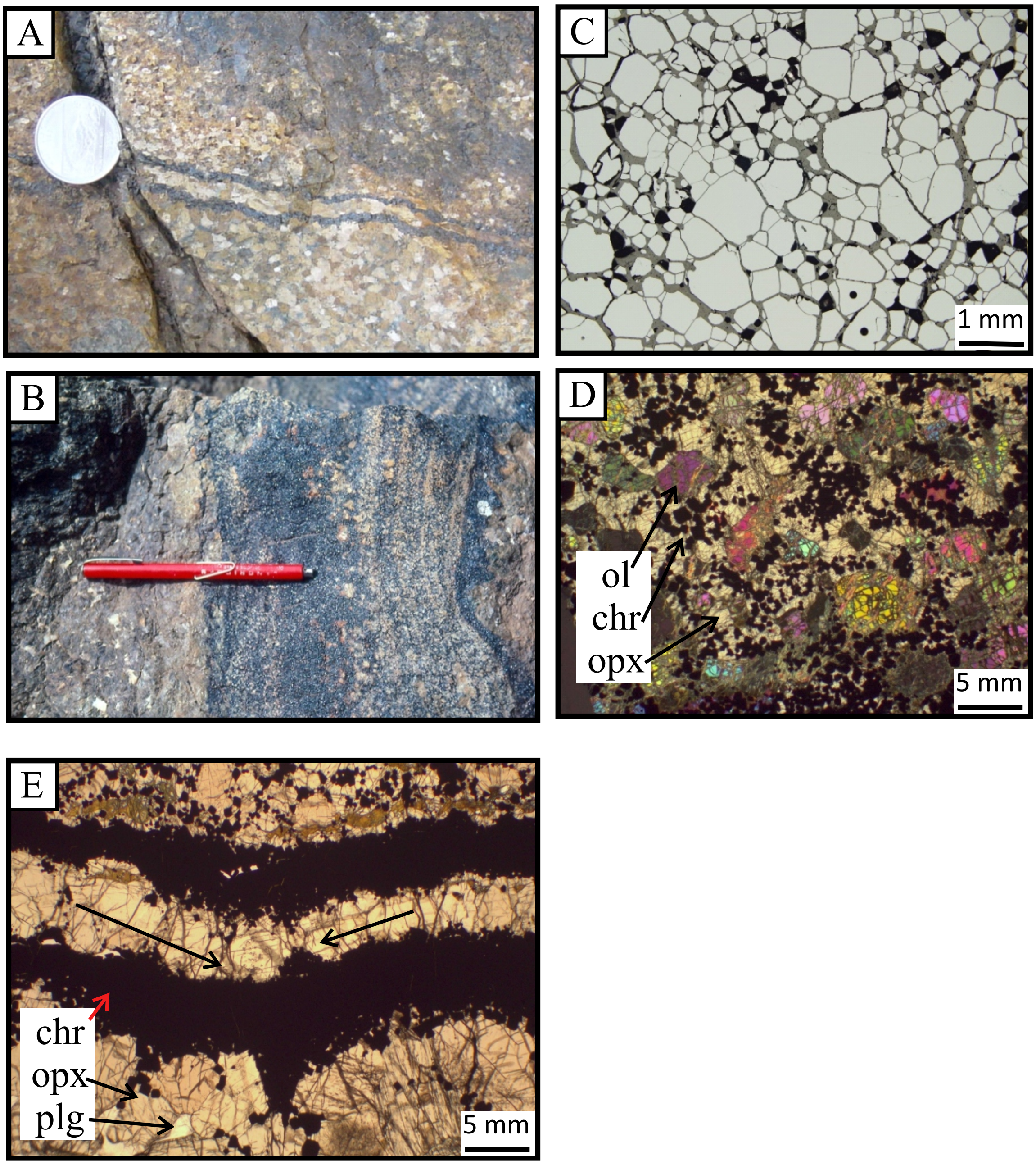
A
C
1 mm
B
D
ol
chr
opx
5 mm
E
chr
opx
plg
5 mm

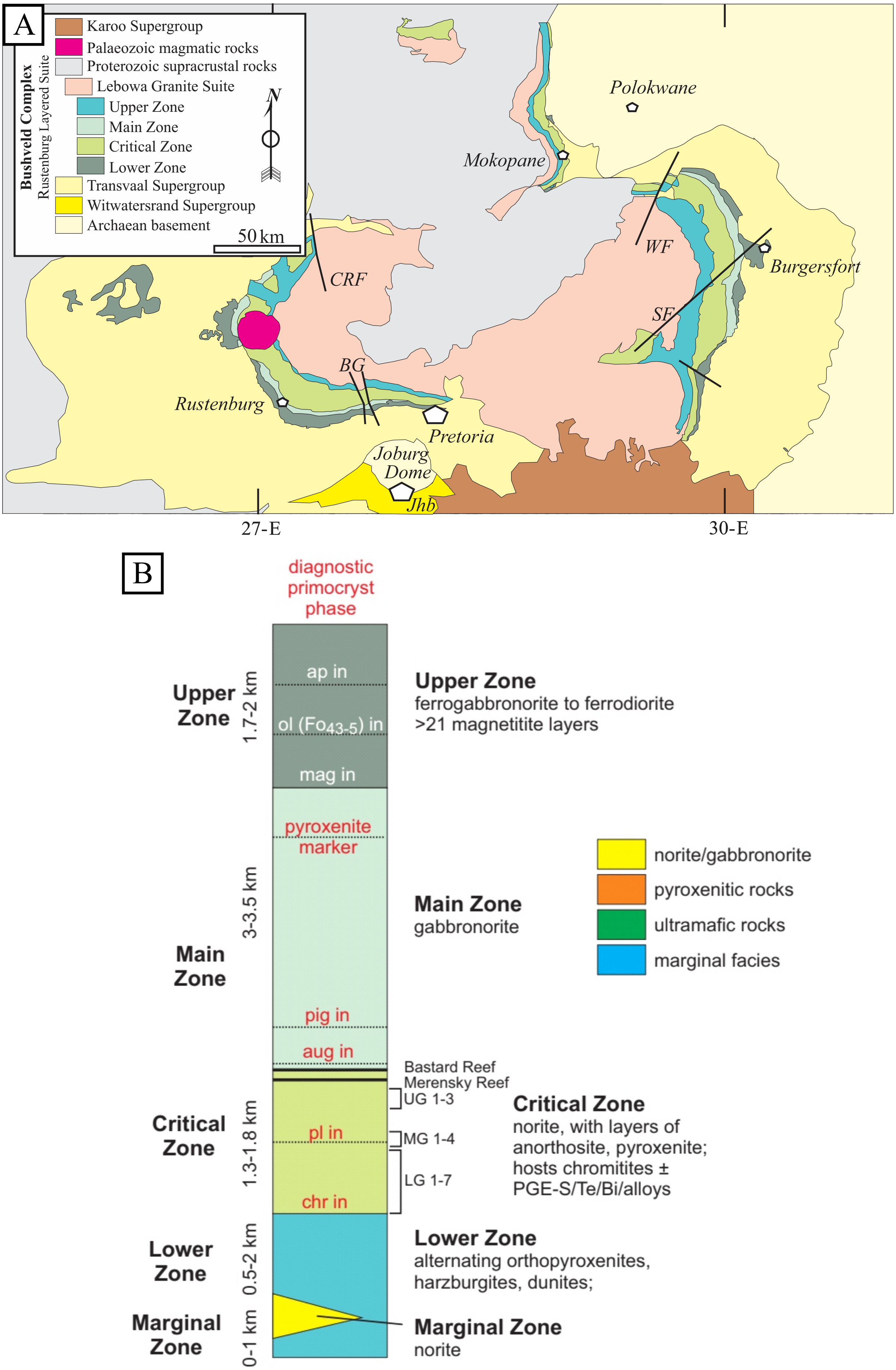
A
Bushveld Complex
Rustenburg Layered Suite
Karoo Supergroup
Palaeozoic magmatic rocks
Proterozoic supracrustal rocks
Lebowa Granite Suite
Upper Zone
Main Zone
Critical Zone
Lower Zone
Transvaal Supergroup
Witwatersrand Supergroup
Archaean basement
N
50 km
Polokwane
Mokopane
WF
Burgersfort
CRF
SF
BG
Rustenburg
Pretoria
Joburg Dome
Jhb
27-E
30-E
B
diagnostic primocryst phase
Upper Zone
1.7-2 km
ap in
ol (Fo43-5) in
mag in
Upper Zone
ferrogabbronorite to ferrodiorite
>21 magnetitite layers
pyroxenite marker
Main Zone
3-3.5 km
Main Zone
gabbronorite
pig in
aug in
norite/gabbronorite
pyroxenitic rocks
ultramafic rocks
marginal facies
Bastard Reef
Merensky Reef
UG 1-3
MG 1-4
LG 1-7
Critical Zone
1.3-1.8 km
pl in
chr in
Critical Zone
norite, with layers of anorthosite, pyroxenite; hosts chromitites ± PGE-S/Te/Bi/alloys
Lower Zone
0.5-2 km
Lower Zone
alternating orthopyroxenites, harzburgites, dunites;
Marginal Zone
0-1 km
Marginal Zone
norite

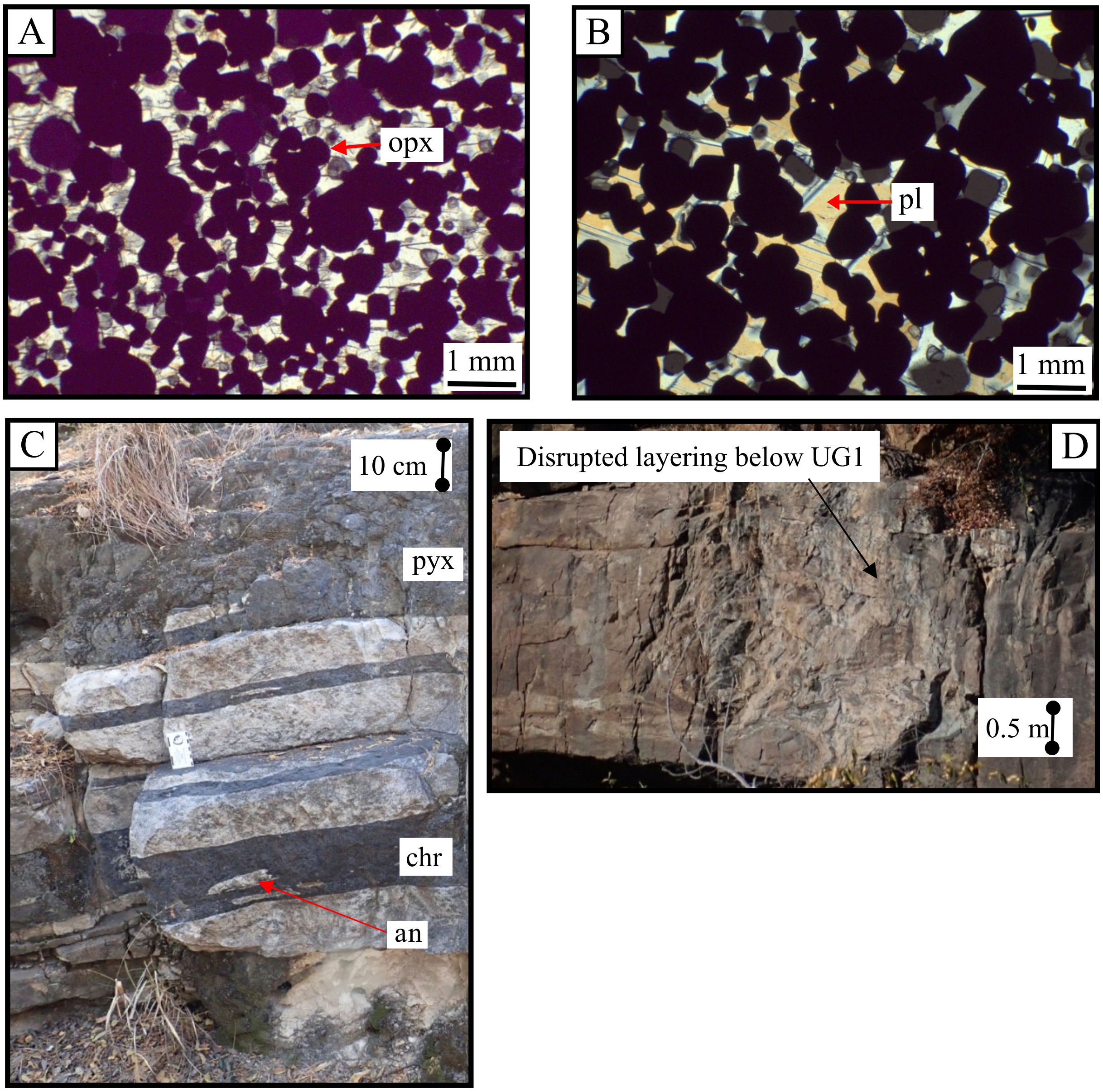
A
opx
1 mm
B
pl
1 mm
C
10 cm
pyx
chr
an
D
Disrupted layering below UG1
0.5 m

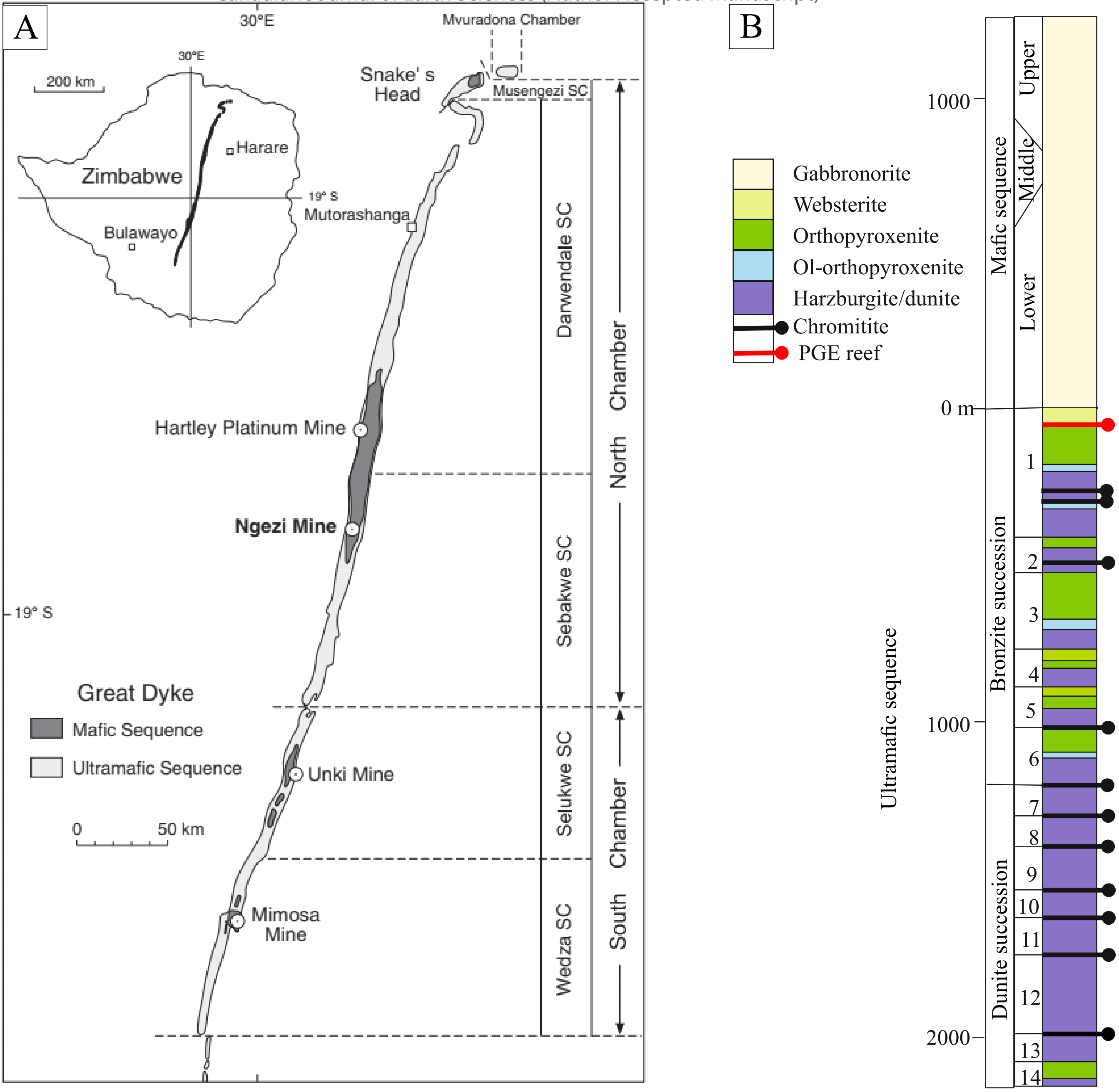
A
30°E
Mvuradona Chamber
30°E
200 km
Snake' s Head
Musengezi SC
Harare
Zimbabwe
19° S
Mutorashanga
Bulawayo
Darwendale SC
North Chamber
Hartley Platinum Mine
Ngezi Mine
Sebakwe SC
19° S
Great Dyke
Mafic Sequence
Ultramafic Sequence
Unki Mine
Selukwe SC
South Chamber
0
50 km
Mimosa Mine
Wedza SC
B
Gabbronorite
Websterite
Orthopyroxenite
Ol-orthopyroxenite
Harzburgite/dunite
Chromitite
PGE reef
1000
0 m
1000
2000
Ultramafic sequence
Mafic sequence
Bronzite succession
Dunite succession
Upper
Middle
Lower
1
2
3
4
5
6
7
8
9
10
11
12
13
14

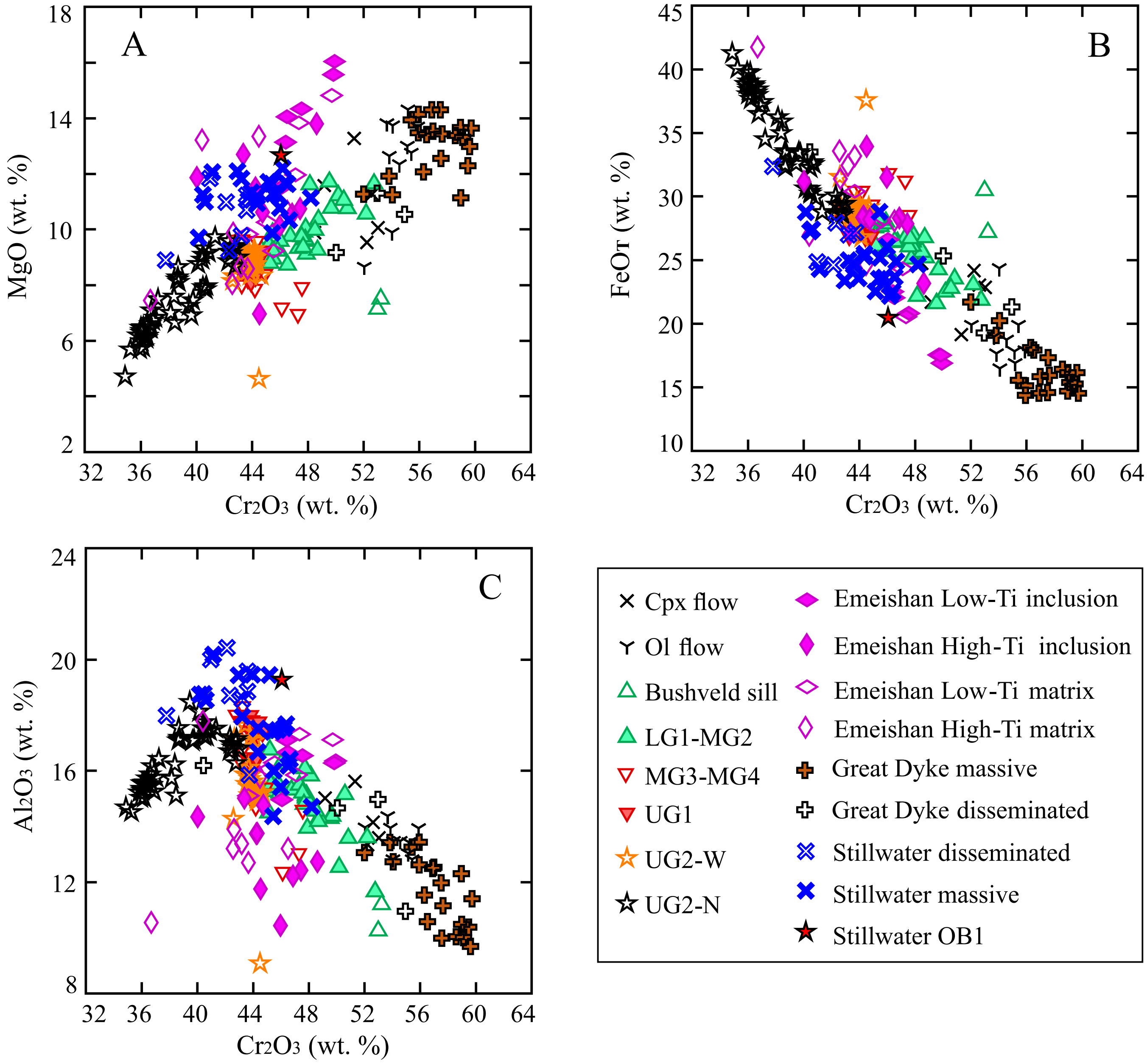
A
MgO (wt. %)
18
14
10
6
2
32
36
40
44
48
52
56
60
64
Cr2O3 (wt. %)
B
FeOT (wt. %)
45
40
35
30
25
20
15
10
32
36
40
44
48
52
56
60
64
Cr2O3 (wt. %)
C
Al2O3 (wt. %)
24
20
16
12
8
32
36
40
44
48
52
56
60
64
Cr2O3 (wt. %)
Cpx flow
Ol flow
Bushveld sill
LG1-MG2
MG3-MG4
UG1
UG2-W
UG2-N
Emeishan Low-Ti inclusion
Emeishan High-Ti inclusion
Emeishan Low-Ti matrix
Emeishan High-Ti matrix
Great Dyke massive
Great Dyke disseminated
Stillwater disseminated
Stillwater massive
Stillwater OB1

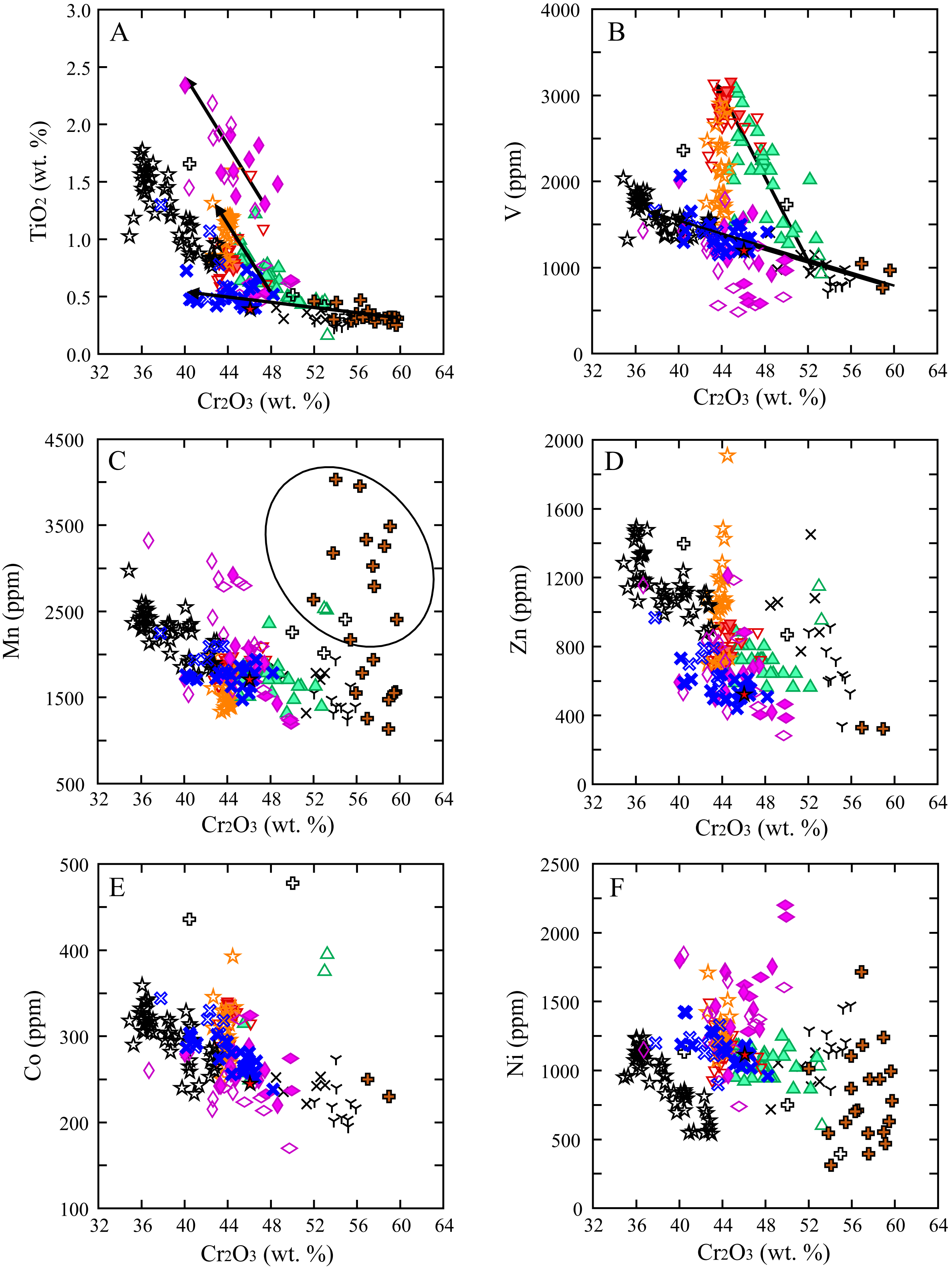
A
TiO2 (wt. %)
3.0
2.5
2.0
1.5
1.0
0.5
0.0
32
36
40
44
48
52
56
60
64
Cr2O3 (wt. %)
B
V (ppm)
4000
3000
2000
1000
0
Cr2O3 (wt. %)
C
Mn (ppm)
4500
3500
2500
1500
500
Cr2O3 (wt. %)
D
Zn (ppm)
2000
1600
1200
800
400
0
Cr2O3 (wt. %)
E
Co (ppm)
500
400
300
200
100
Cr2O3 (wt. %)
F
Ni (ppm)
2500
2000
1500
1000
500
0
Cr2O3 (wt. %)

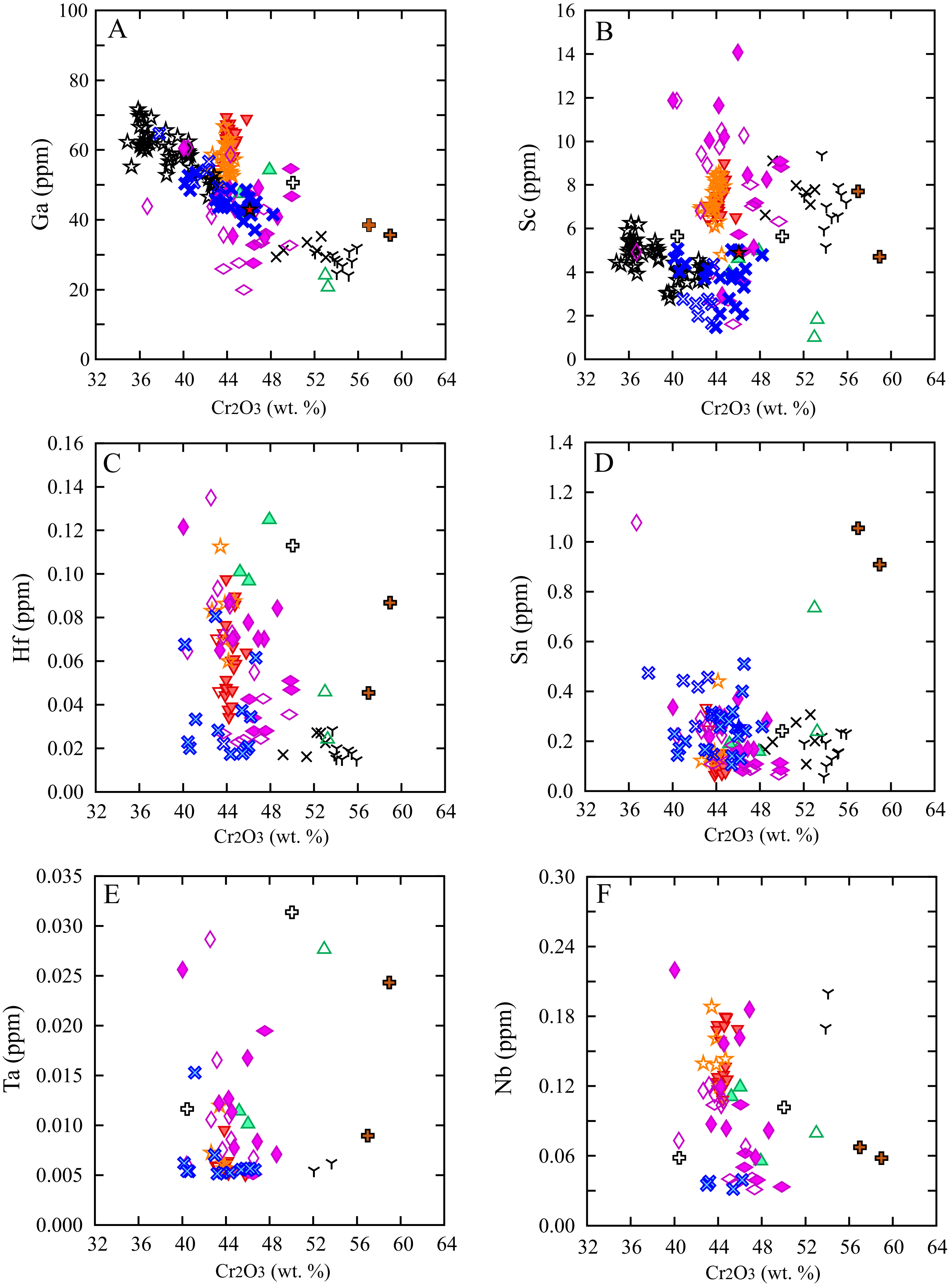
A
Ga (ppm)
0
20
40
60
80
100
B
Sc (ppm)
0
2
4
6
8
10
12
14
16
C
Hf (ppm)
0.00
0.02
0.04
0.06
0.08
0.10
0.12
0.14
0.16
D
Sn (ppm)
0.0
0.2
0.4
0.6
0.8
1.0
1.2
1.4
E
Ta (ppm)
0.000
0.005
0.010
0.015
0.020
0.025
0.030
0.035
F
Nb (ppm)
0.00
0.06
0.12
0.18
0.24
0.30
32
36
40
44
48
52
56
60
64
Cr2O3 (wt. %)

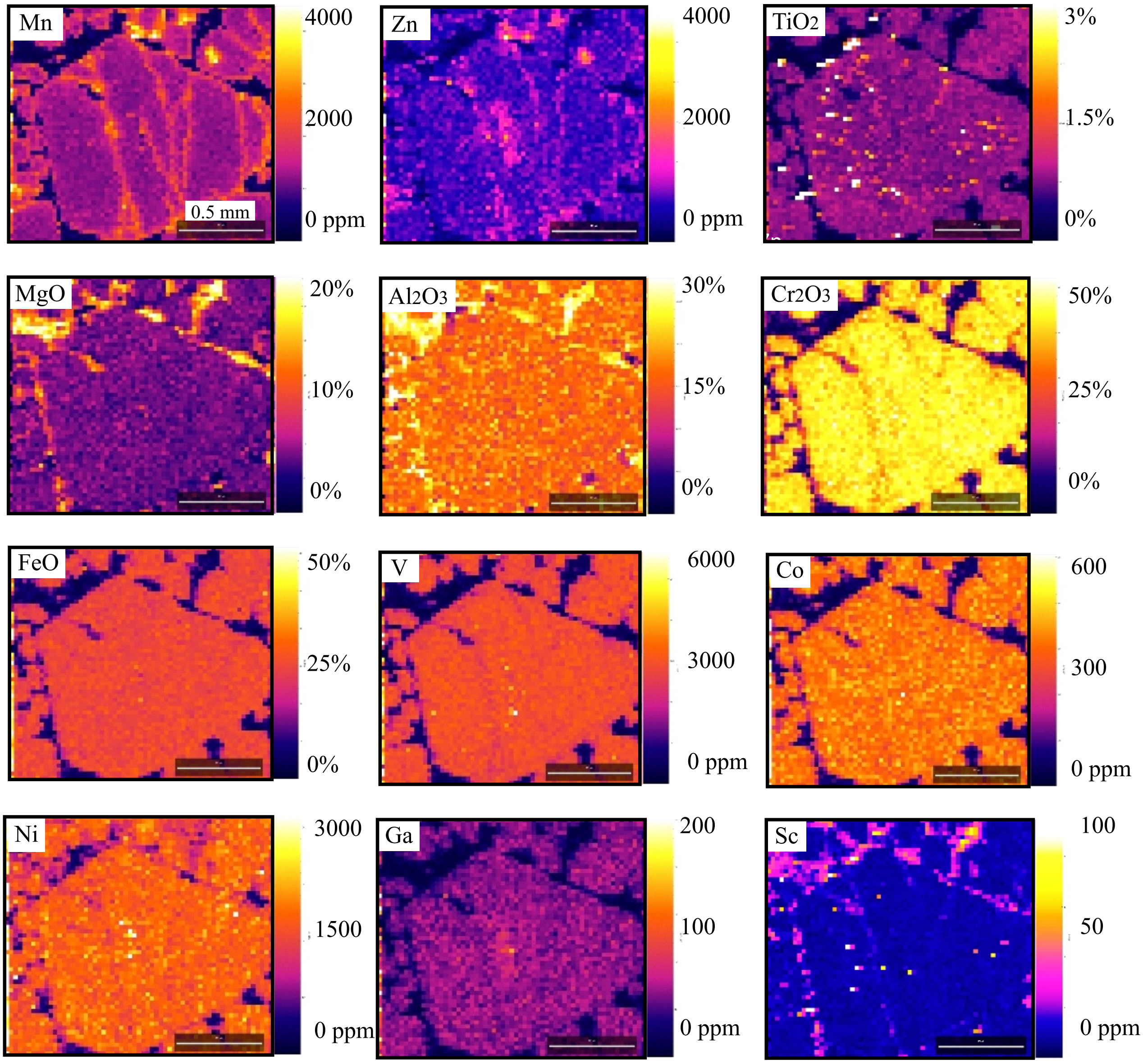
Mn
0.5 mm
4000
2000
0 ppm
Zn
4000
2000
0 ppm
TiO2
3%
1.5%
0%
MgO
20%
10%
0%
Al2O3
30%
15%
0%
Cr2O3
50%
25%
0%
FeO
50%
25%
0%
V
6000
3000
0 ppm
Co
600
300
0 ppm
Ni
3000
1500
0 ppm
Ga
200
100
0 ppm
Sc
100
50
0 ppm

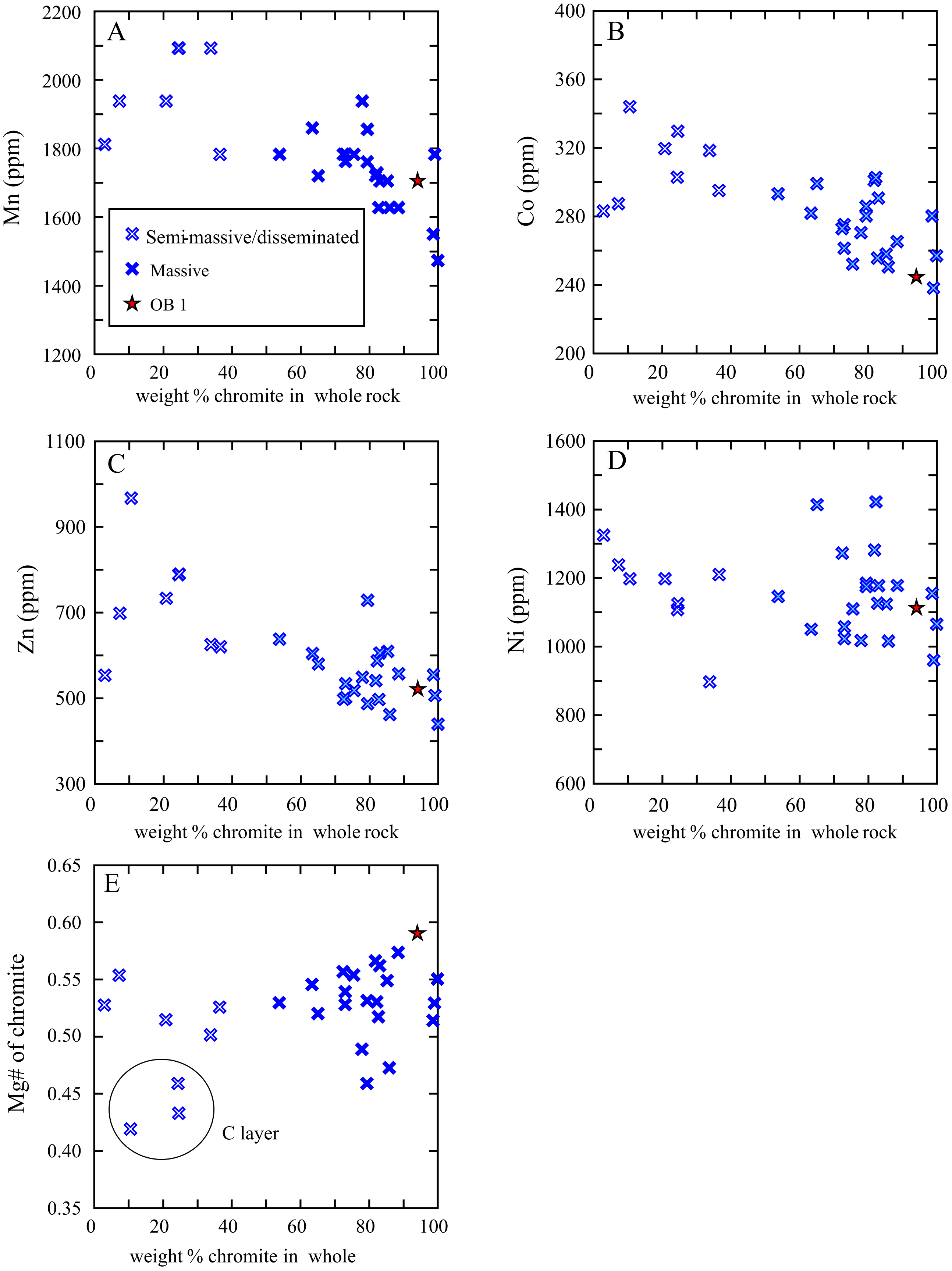
A
Mn (ppm)
2200
2000
1800
1600
1400
1200
0
20
40
60
80
100
weight % chromite in whole rock
Semi-massive/disseminated
Massive
OB 1
B
Co (ppm)
400
360
320
280
240
200
0
20
40
60
80
100
weight % chromite in whole rock
C
Zn (ppm)
1100
900
700
500
300
0
20
40
60
80
100
weight % chromite in whole rock
D
Ni (ppm)
1600
1400
1200
1000
800
600
0
20
40
60
80
100
weight % chromite in whole rock
E
Mg# of chromite
0.65
0.60
0.55
0.50
0.45
0.40
0.35
C layer
0
20
40
60
80
100
weight % chromite in whole

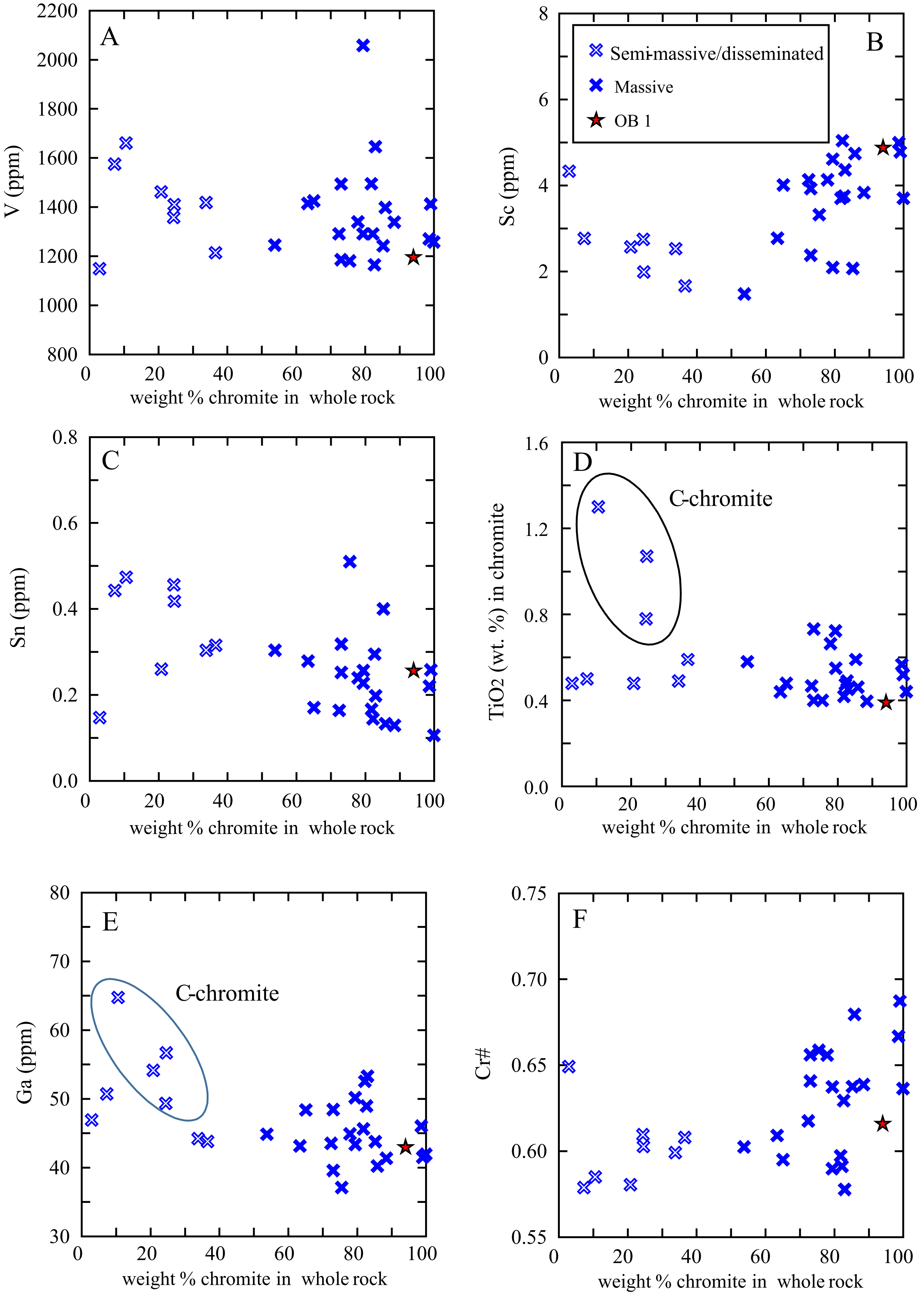
A
V (ppm)
2200
2000
1800
1600
1400
1200
1000
800
0
20
40
60
80
100
weight % chromite in whole rock
B
Semi-massive/disseminated
Massive
OB 1
Sc (ppm)
8
6
4
2
0
weight % chromite in whole rock
C
Sn (ppm)
0.8
0.6
0.4
0.2
0.0
weight % chromite in whole rock
D
C-chromite
TiO2 (wt. %) in chromite
1.6
1.2
0.8
0.4
0.0
weight % chromite in whole rock
E
C-chromite
Ga (ppm)
80
70
60
50
40
30
weight % chromite in whole rock
F
Cr#
0.75
0.70
0.65
0.60
0.55
weight % chromite in whole rock

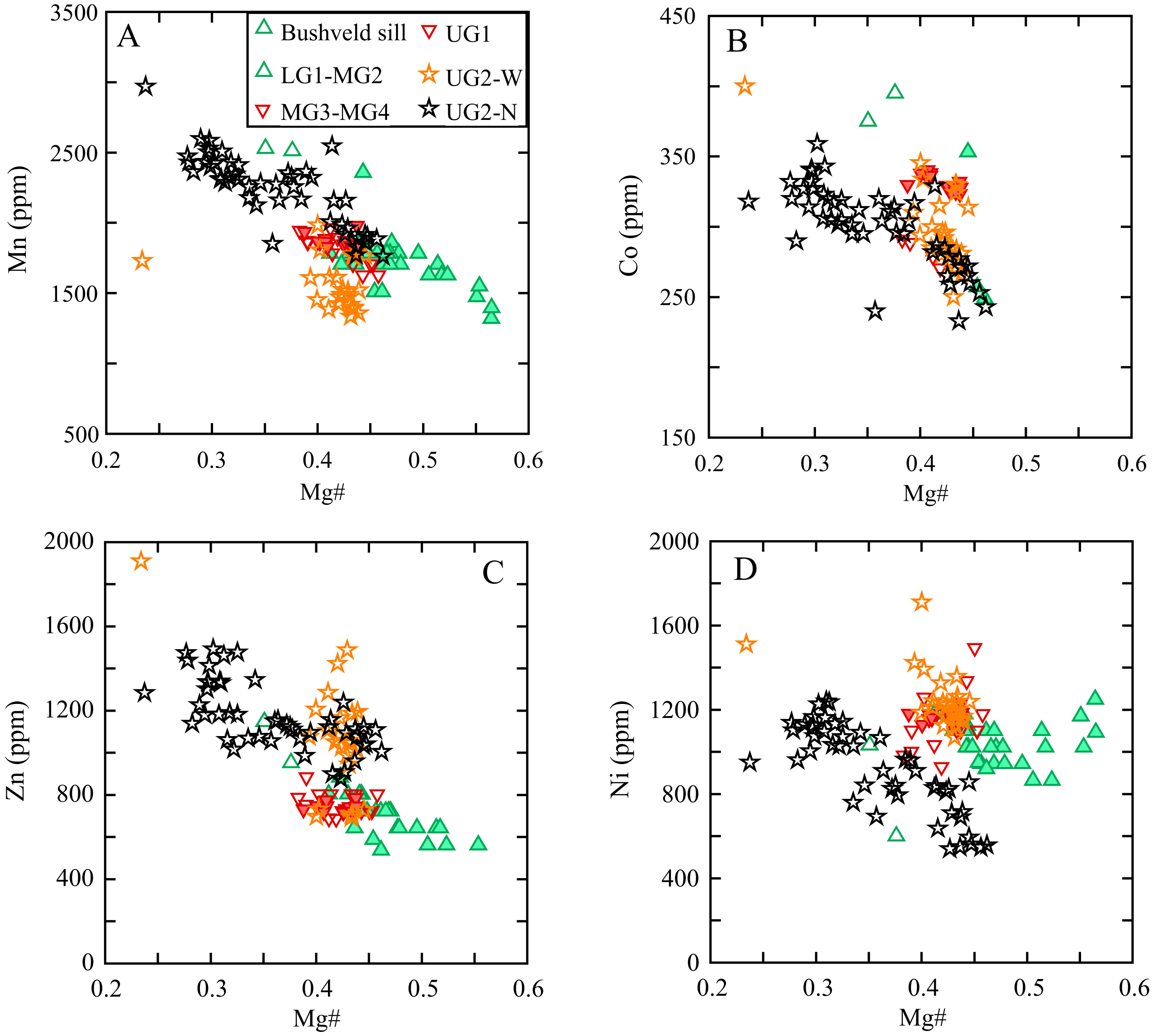
A
Bushveld sill
LG1-MG2
MG3-MG4
UG1
UG2-W
UG2-N
Mn (ppm)
3500
2500
1500
500
0.2
0.3
0.4
0.5
0.6
Mg#
B
Co (ppm)
450
350
250
150
C
Zn (ppm)
2000
1600
1200
800
400
0
D
Ni (ppm)

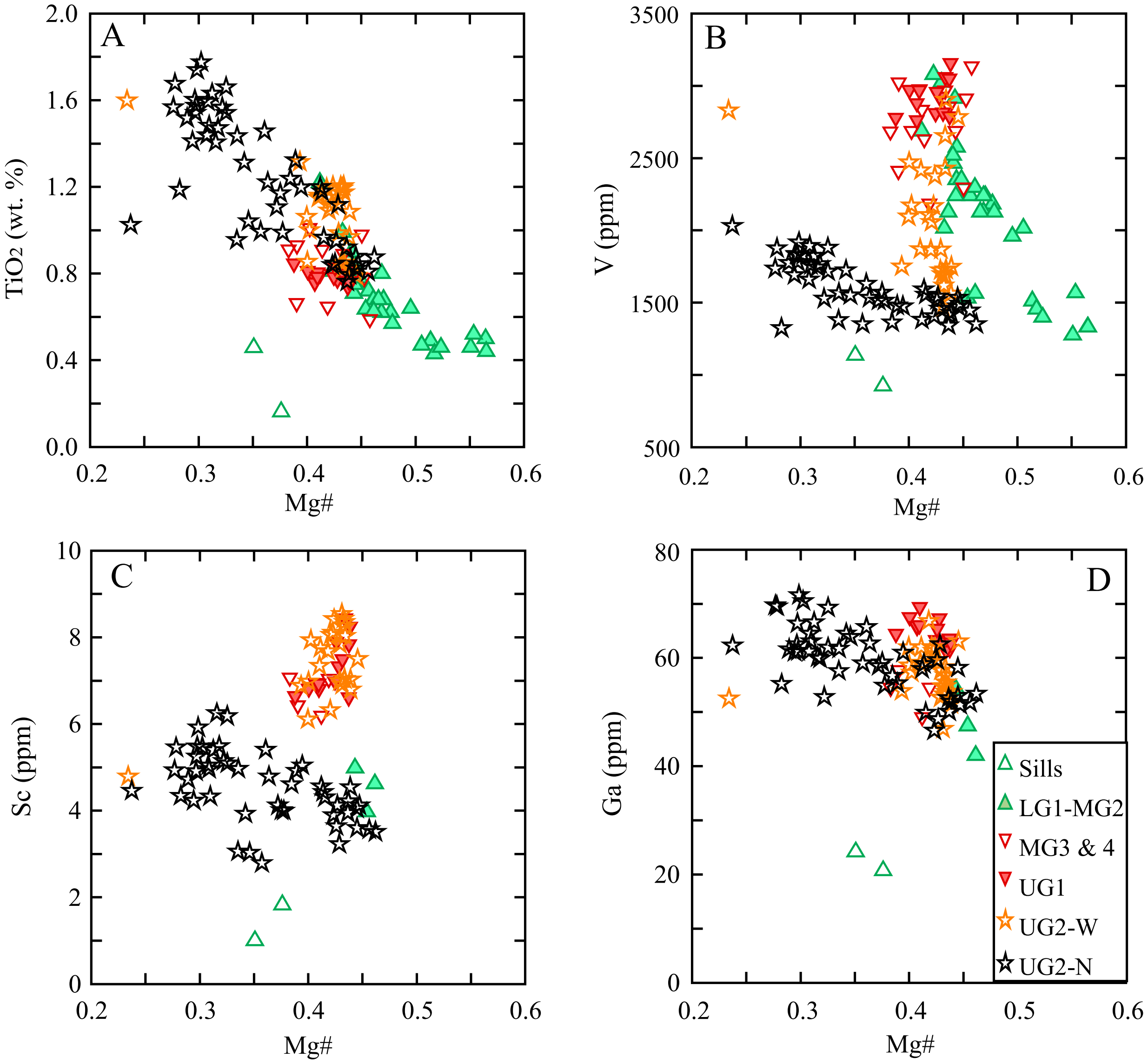
A
TiO2 (wt. %)
2.0
1.6
1.2
0.8
0.4
0.0
0.2
0.3
0.4
0.5
0.6
Mg#
B
V (ppm)
3500
2500
1500
500
0.2
0.3
0.4
0.5
0.6
Mg#
C
Sc (ppm)
10
8
6
4
2
0
0.2
0.3
0.4
0.5
0.6
Mg#
D
Ga (ppm)
80
60
40
20
0
0.2
0.3
0.4
0.5
0.6
Mg#
Sills
LG1-MG2
MG3 & 4
UG1
UG2-W
UG2-N

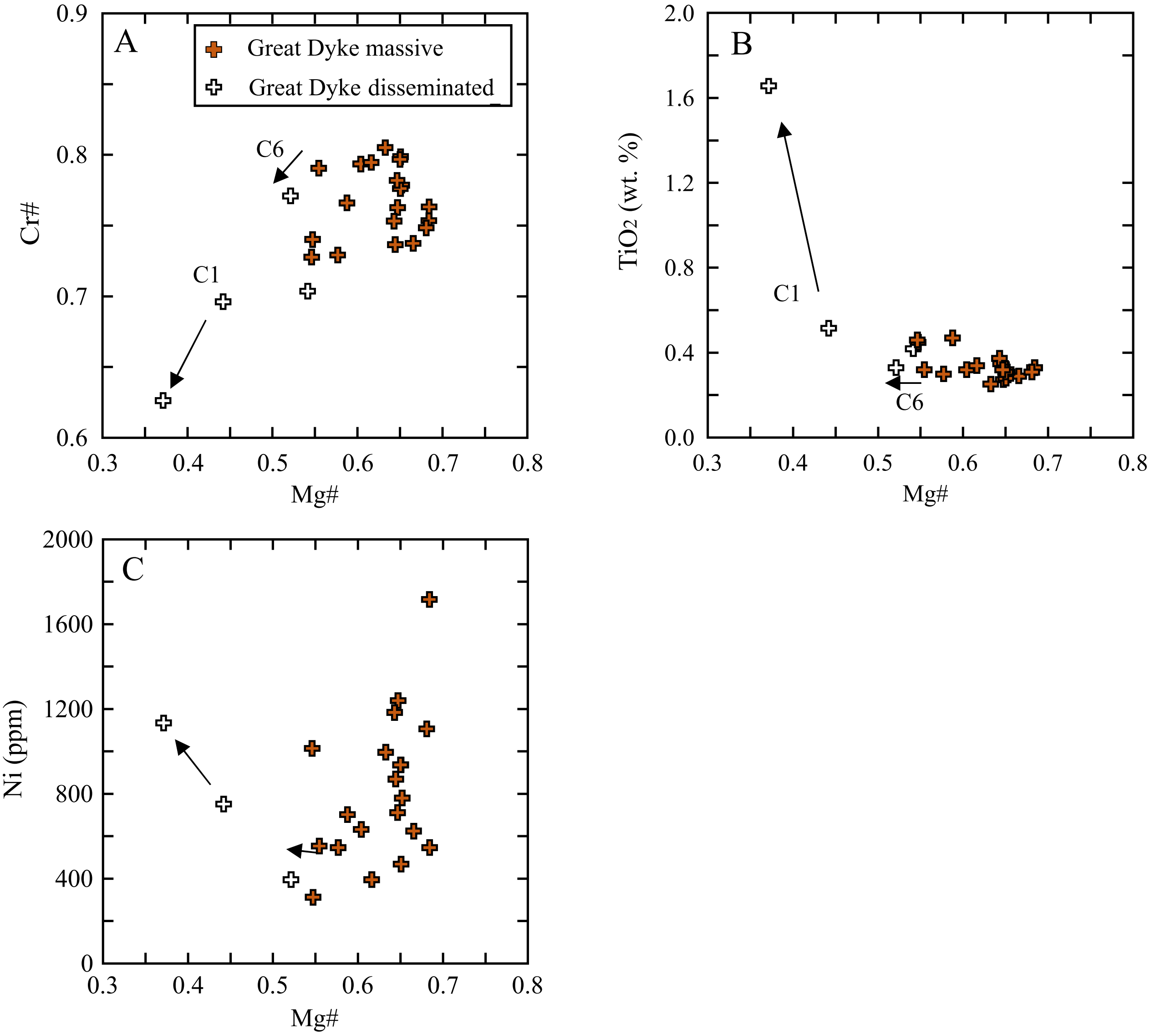
A
Great Dyke massive
Great Dyke disseminated
Cr#
0.6
0.7
0.8
0.9
C6
C1
Mg#
0.3
0.4
0.5
0.6
0.7
0.8
B
TiO2 (wt. %)
0.0
0.4
0.8
1.2
1.6
2.0
C1
C6
Mg#
0.3
0.4
0.5
0.6
0.7
0.8
C
Ni (ppm)
0
400
800
1200
1600
2000
Mg#
0.3
0.4
0.5
0.6
0.7
0.8

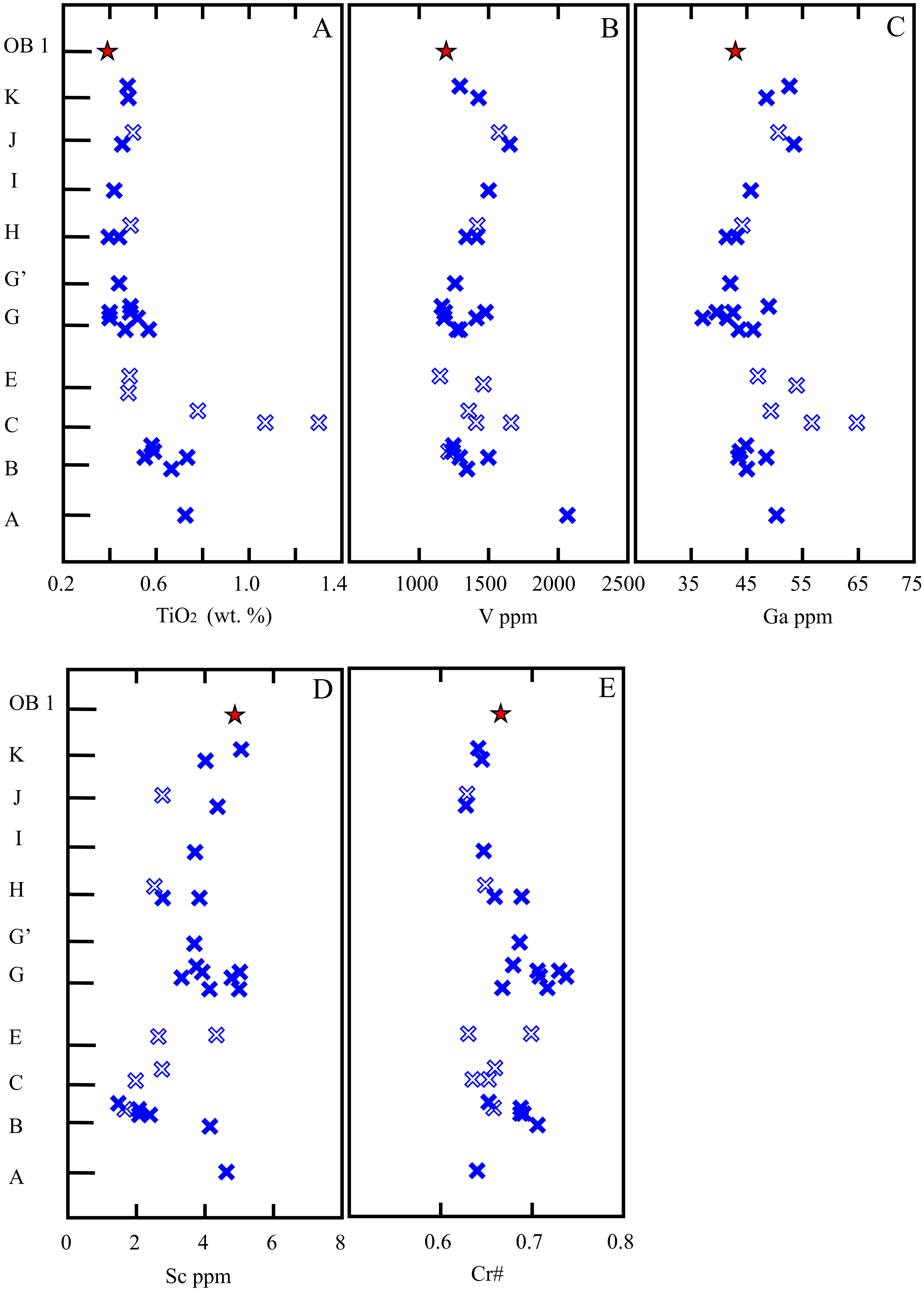
A
B
C
D
E
OB 1
K
J
I
H
G’
G
E
C
B
A
0.2
0.6
1.0
1.4
TiO2 (wt. %)
1000
1500
2000
2500
V ppm
35
45
55
65
75
Ga ppm
0
2
4
6
8
Sc ppm
0.6
0.7
0.8
Cr#

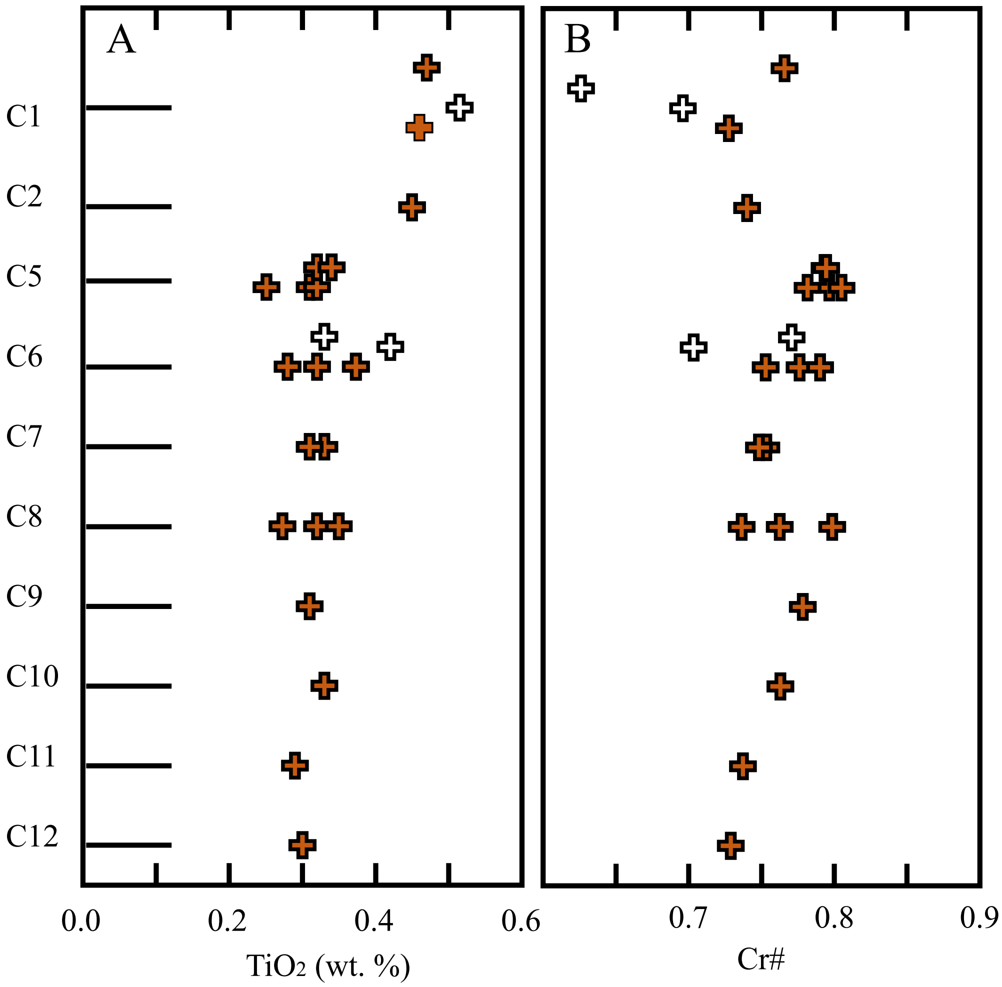
A
B
C1
C2
C5
C6
C7
C8
C9
C10
C11
C12
0.0
0.2
0.4
0.6
TiO2 (wt. %)
0.7
0.8
0.9
Cr#

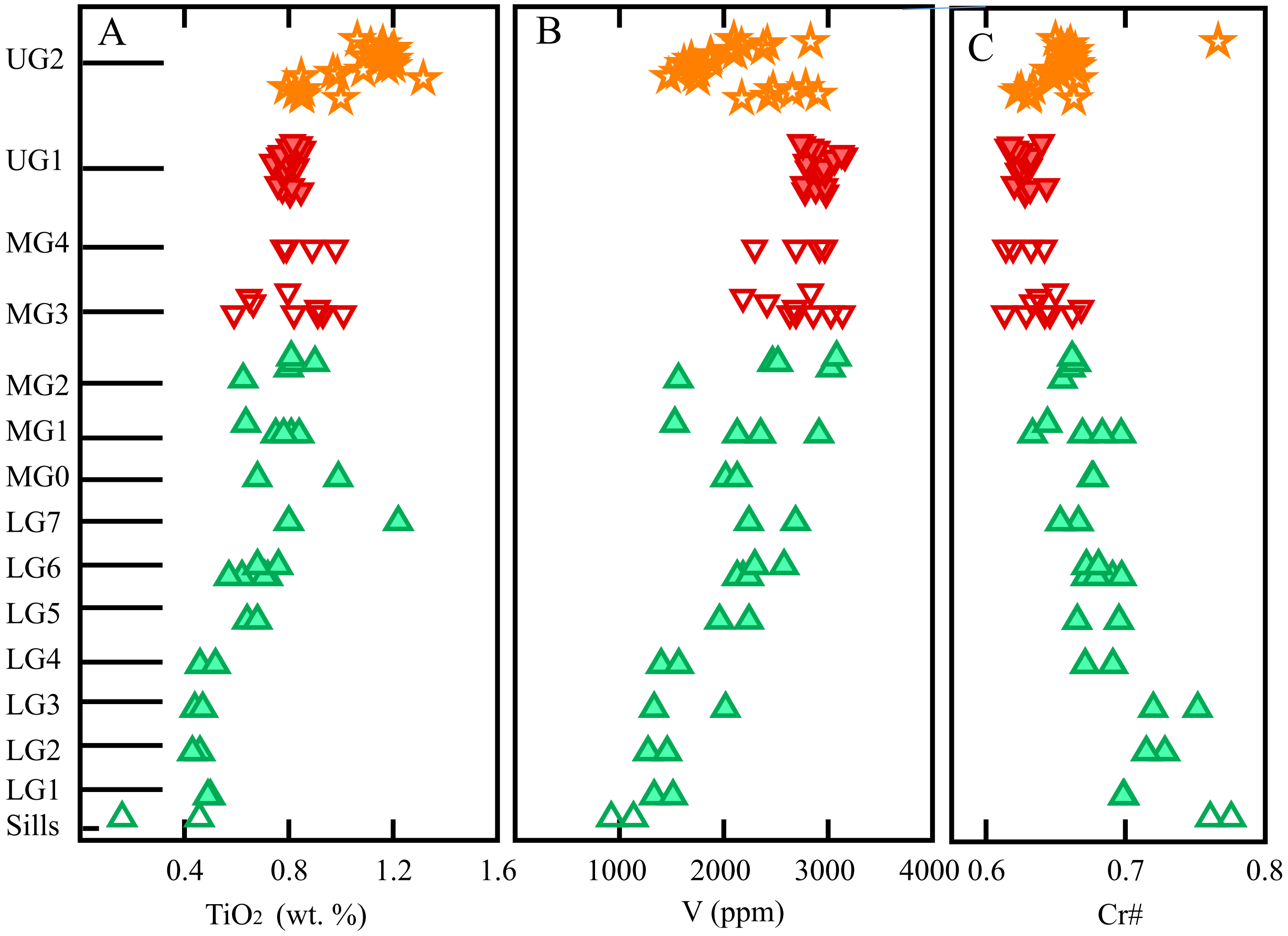
A
B
C
UG2
UG1
MG4
MG3
MG2
MG1
MG0
LG7
LG6
LG5
LG4
LG3
LG2
LG1
Sills
0.4
0.8
1.2
1.6
TiO2 (wt. %)
1000
2000
3000
4000
V (ppm)
0.6
0.7
0.8
Cr#

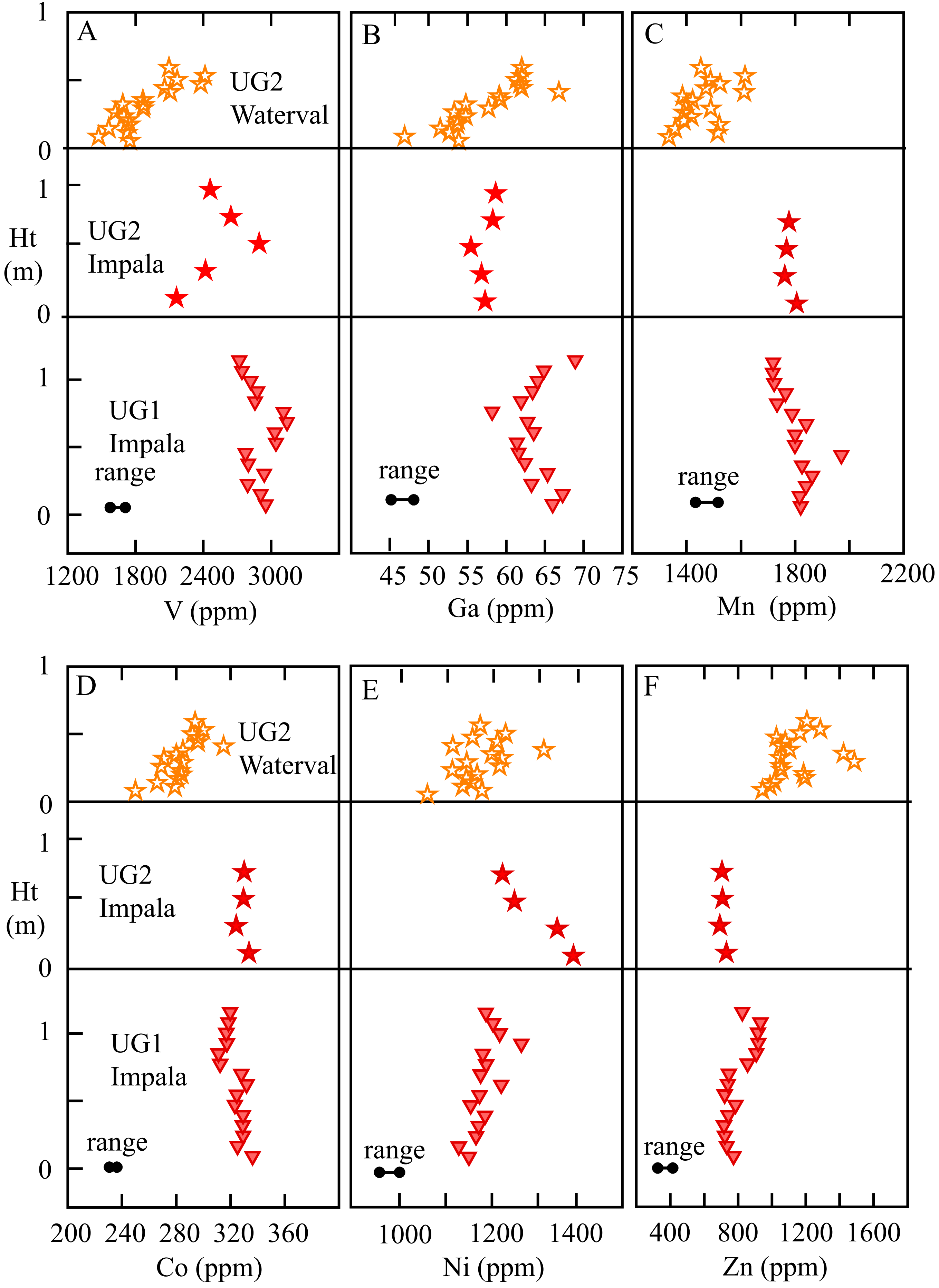
A
B
C
UG2
Waterval
UG2
Impala
UG1
Impala
range
Ht
(m)
1
0
1
0
1
0
1200 1800 2400 3000
V (ppm)
45 50 55 60 65 70 75
Ga (ppm)
1400 1800 2200
Mn (ppm)
D
E
F
Co (ppm)
200 240 280 320 360
Ni (ppm)
1000 1200 1400
Zn (ppm)
400 800 1200 1600

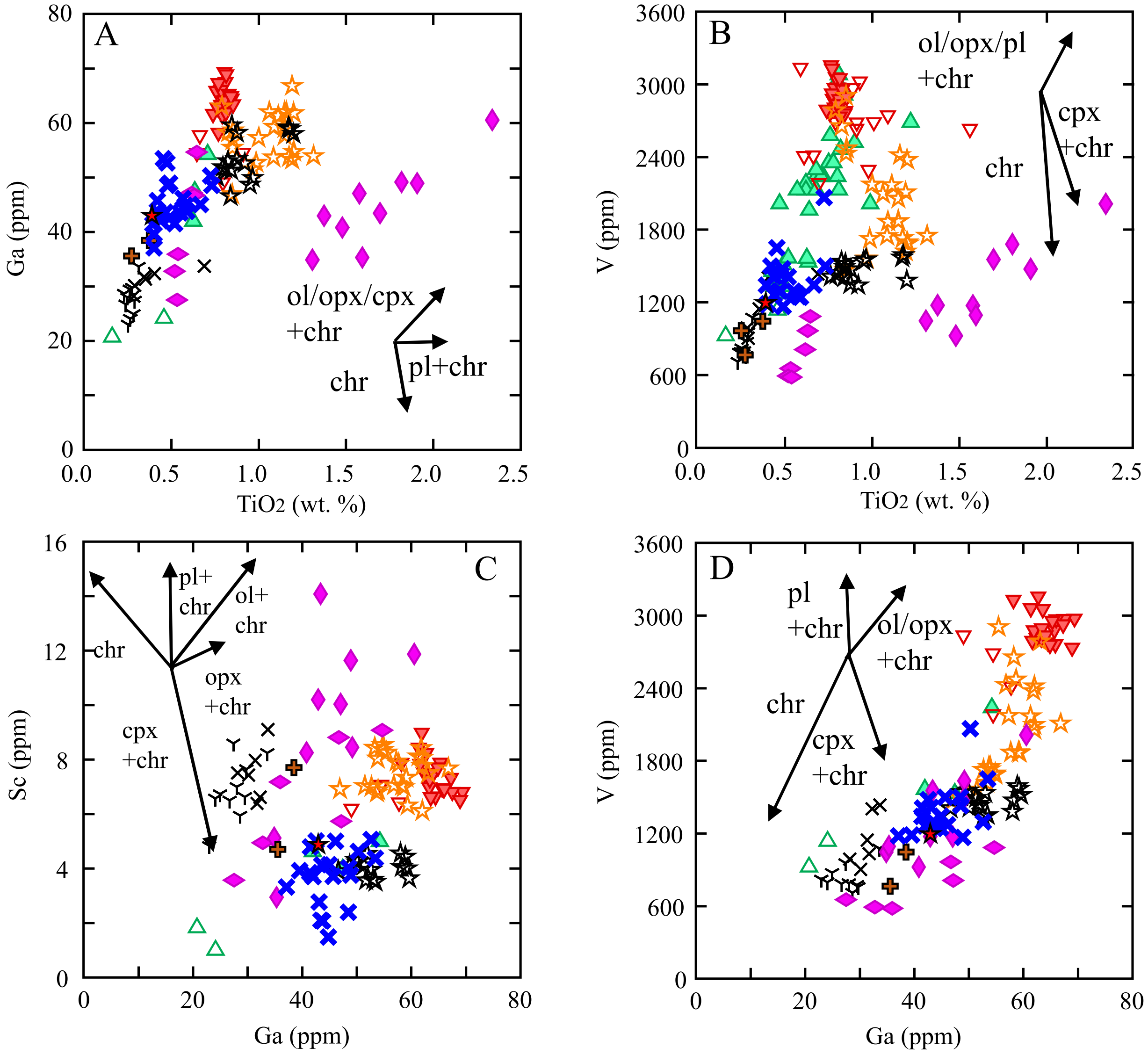
A
Ga (ppm)
TiO2 (wt. %)
ol/opx/cpx
+chr
pl+chr
chr
B
V (ppm)
TiO2 (wt. %)
ol/opx/pl
+chr
cpx
+chr
chr
C
Sc (ppm)
Ga (ppm)
pl+
chr
ol+
chr
chr
opx
+chr
cpx
+chr
D
V (ppm)
Ga (ppm)
pl
+chr
ol/opx
+chr
chr
cpx
+chr

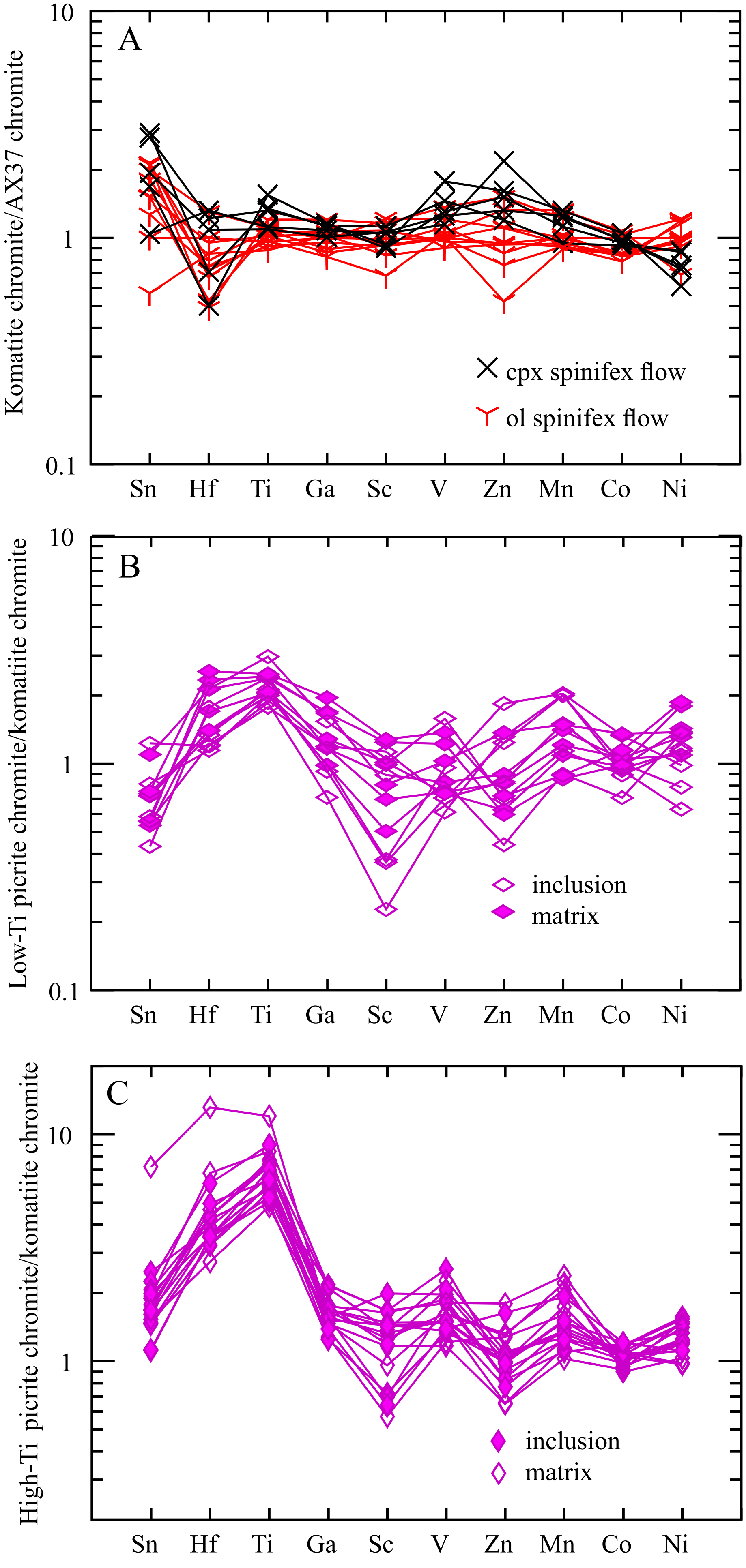
A
Komatite chromite/AX37 chromite
10
1
0.1
✕ cpx spinifex flow
Y ol spinifex flow
Sn
Hf
Ti
Ga
Sc
V
Zn
Mn
Co
Ni
B
Low-Ti picrite chromite/komatiite chromite
10
1
0.1
◇ inclusion
◆ matrix
Sn
Hf
Ti
Ga
Sc
V
Zn
Mn
Co
Ni
C
High-Ti picrite chromite/komatiite chromite
10
1
◆ inclusion
◇ matrix
Sn
Hf
Ti
Ga
Sc
V
Zn
Mn
Co
Ni

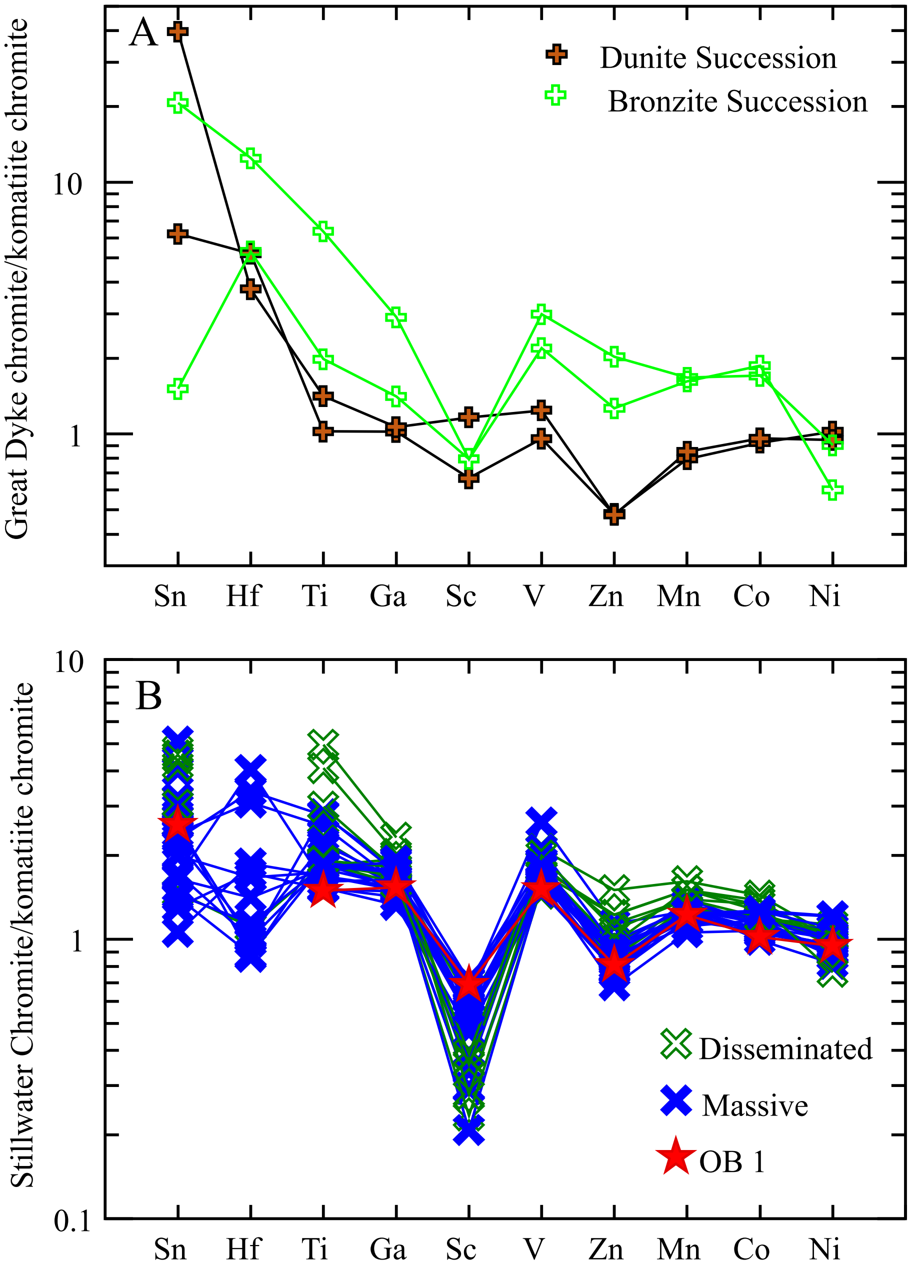
A
Dunite Succession
Bronzite Succession
Great Dyke chromite/komatiite chromite
10
1
Sn
Hf
Ti
Ga
Sc
V
Zn
Mn
Co
Ni
B
Stillwater Chromite/komatiite chromite
10
1
0.1
Disseminated
Massive
OB 1
Sn
Hf
Ti
Ga
Sc
V
Zn
Mn
Co
Ni

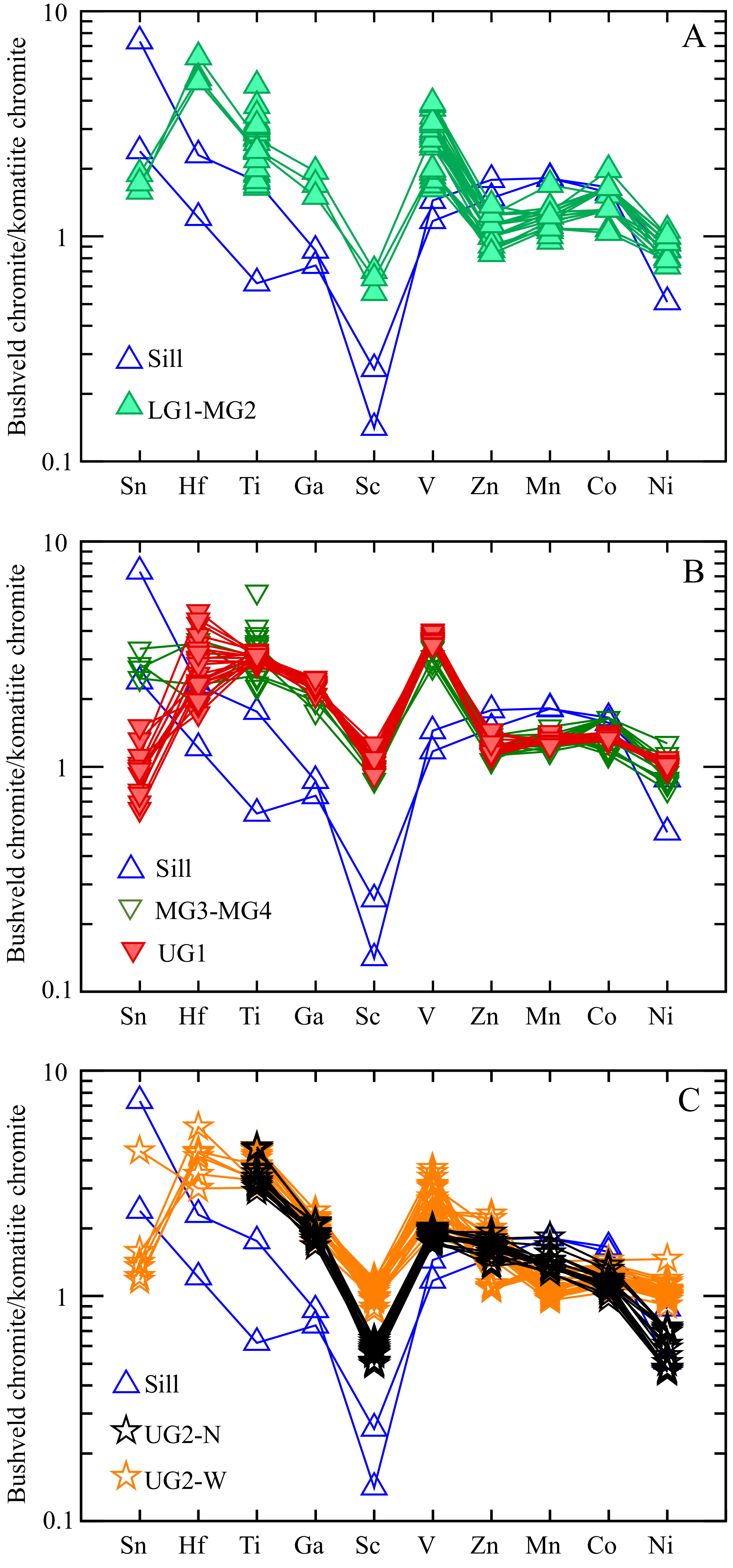
A
Bushveld chromite/komatiite chromite
10
1
0.1
Sn
Hf
Ti
Ga
Sc
V
Zn
Mn
Co
Ni
△ Sill
▲ LG1-MG2
B
Bushveld chromite/komatiite chromite
10
1
0.1
Sn
Hf
Ti
Ga
Sc
V
Zn
Mn
Co
Ni
△ Sill
▽ MG3-MG4
▼ UG1
C
Bushveld chromite/komatiite chromite
10
1
0.1
Sn
Hf
Ti
Ga
Sc
V
Zn
Mn
Co
Ni
△ Sill
☆ UG2-N
☆ UG2-W

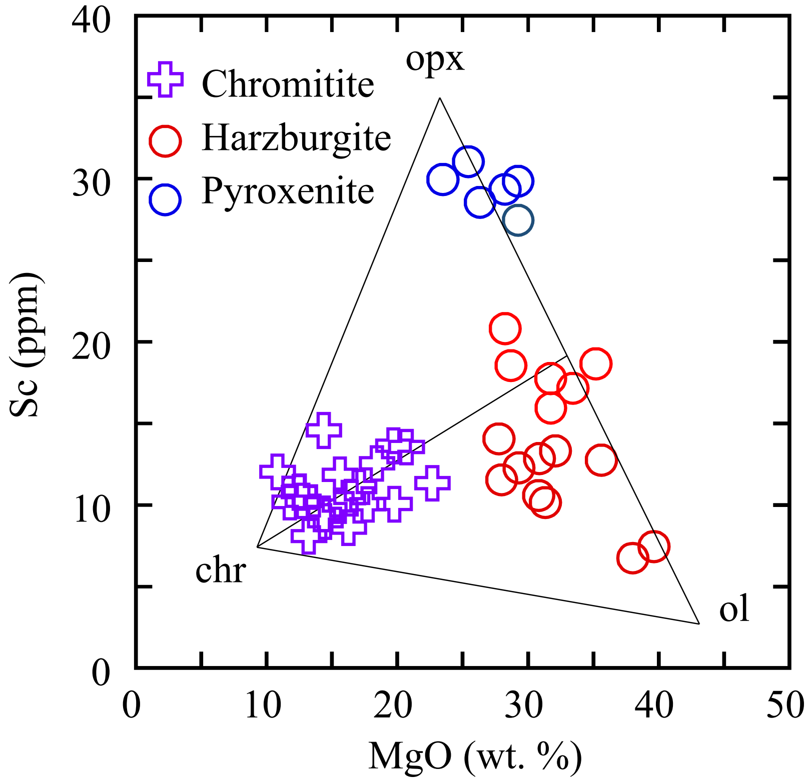
Chromitite
Harzburgite
Pyroxenite
opx
chr
ol
Sc (ppm)
MgO (wt. %)
0
10
20
30
40
50